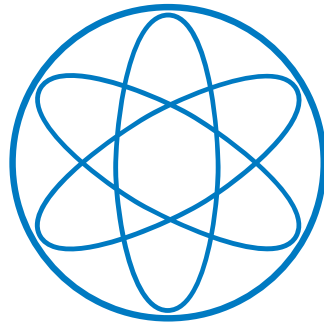


Denis Bytschkow

Investigation of MHD mode rotation in the tokamak ASDEX Upgrade

IPP 1/341
September, 2010

PHYSIK-DEPARTMENT
TECHNISCHE UNIVERSITÄT MÜNCHEN



Investigation of MHD mode
rotation in the tokamak
ASDEX Upgrade

Master Thesis
by
Denis Bytschkow

September 2010



Max Planck Institut für Plasmaphysik
Projekt ASDEX Upgrade
Boltzmannstr. 2, 85748 Garching
Prof. Dr. S. Günter



Abstract

The rotation of MHD modes in a fast rotating tokamak plasma is mainly determined by the plasma rotation frequency. Additionally, magnetic islands are expected to have an offset velocity, due to the electron diamagnetic drift. This follows from the condition, that the magnetic field structure is *frozen* in the plasma electrons. The electron diamagnetic drift velocity acts as an offset in the counter current direction. Hence, in ASDEX Upgrade magnetic islands should rotate slower than the ambient plasma. However, several MHD modes show the opposite effect and rotate even faster. This observation was confirmed in investigations for ASDEX Upgrade [35] and DIII-D [16].

A possible explanation for this behavior is the neoclassical toroidal viscosity theory (NTV). NTV adds a neoclassical toroidal offset velocity, which can increase the MHD mode rotation with respect to the plasma rotation. Additionally, MHD modes generate an NTV torque, which connects them with the ambient plasma flow.

In this thesis the influence of various effects on MHD mode rotation are investigated. Several models are compared with the observed mode rotation. It will be shown that the rotation of magnetic islands cannot be described alone with the plasma rotation together with the electron diamagnetic drift and that the neoclassical toroidal offset has to be taken into account. It will be shown, that this can improve the description of MHD mode rotation.

However, in some cases with strong mode coupling of 2 MHD modes with the same toroidal but different poloidal mode numbers this is not sufficient. In order to consider mode coupling, an MHD mode rotation model is used, which describes the MHD mode rotation with the NTV torque resulting from both coupled modes. Since the plasma rotation and the MHD mode rotation do not change in a stationary case, we assume that the mode rotation frequency adjust such that the total NTV torque vanishes. This approach is used to determine the expected MHD mode rotation and compared with the measured mode frequency.

Contents

| | |
|--|-----------|
| 1. Introduction | 1 |
| 1.1. Thermonuclear Fusion | 2 |
| 1.2. Magnetic Confinement and Tokamak | 4 |
| 1.3. Importance of Plasma and MHD Mode Rotation | 5 |
| 1.4. Motivation and Outline | 6 |
| 2. Theoretical Principles | 9 |
| 2.1. Introduction | 9 |
| 2.2. Tokamak Equilibrium | 11 |
| 2.3. Neoclassical Theory and Trapped Particles | 13 |
| 2.4. Magnetohydrodynamic Stability and MHD Modes | 14 |
| 2.5. Plasma Rotation | 17 |
| 2.6. MHD Mode Rotation | 19 |
| 2.7. Neoclassical Toroidal Viscosity | 21 |
| 2.8. Summary | 22 |
| 3. ASDEX Upgrade and Diagnostics | 23 |
| 3.1. ASDEX Upgrade | 23 |
| 3.2. Charge Exchange Recombination Spectroscopy | 25 |
| 3.3. Electron Cyclotron Emission | 27 |
| 3.4. Magnetic Measurements | 28 |
| 3.5. Soft X-Ray Diagnostic | 29 |
| 3.6. Integrated Data Analysis | 31 |
| 4. Methodological Approach | 33 |
| 4.1. MHD Mode Characterisation | 33 |
| 4.1.1. Determination of MHD Mode Frequency | 33 |
| 4.1.2. MHD Mode Numbers | 35 |
| 4.1.3. MHD Mode Localisation | 36 |
| 4.1.4. MHD Mode Coupling | 37 |

| | |
|---|-----------|
| 4.2. Determination of Plasma Rotation Frequency | 38 |
| 4.3. Electron Diamagnetic Drift | 39 |
| 4.3.1. Consideration of Geometrical Properties | 40 |
| 5. MHD Modes and Plasma Rotation | 43 |
| 5.1. The Rotation of (3/2) Modes | 43 |
| 5.2. The Rotation of (2/1) Modes with Flat Temperature Profiles | 51 |
| 6. Neoclassical Influence on MHD Mode Rotation | 57 |
| 6.1. Determination of the NTV Regime | 57 |
| 6.2. (3/2) Mode Rotation with the Neoclassical Offset | 60 |
| 6.3. (2/1) Modes with Flat Temperature Profiles | 64 |
| 6.4. Neoclassical Torque | 67 |
| 6.5. Determination of the Frequency with Vanishing Torque | 70 |
| 7. Summary, Conclusions and Outlook | 75 |
| A. Determination of $b_{m,n}$ | 77 |
| B. Determination of $W_{m,n}$ | 79 |
| Bibliography | 81 |
| Acknowledgment | 87 |

Chapter 1.

Introduction

Historical development demonstrates the significance of energy and the importance of new energy sources in our life. Currently, our energy supply is mainly based on limited natural resources, which can deplete in the next decades. In search for new technologies controlled fusion has a tremendous potential to become a long-term option as an environmentally friendly and almost unlimited energy source.

The possibility of fusion reactions is shown by the sun, which provided us with energy for the last billion years. The most promising candidate for the commercial production of energy is the fusion of deuterium (D) and tritium (T). The reasons are explained in the next section. The fusion reaction produces helium, neutrons and kinetic energy, which is distributed according to the reversed mass ratio of the reaction products, 20% for He and 80% for the neutron:



The energy of 17.6 MeV per reaction corresponds to 94 GWh thermal energy for 1 kg of D - T fuel, which is equivalent to 11.5 Mio kg coal or 10.6 Mio m³ natural gas. Since deuterium is a stable isotope it occurs in natural hydrogen compounds to the extent of 0.015%. It can be extracted from the water in the oceans in practically unlimited quantities. One m³ water contains 33 g deuterium and the extraction is already done routinely for scientific and industrial applications.

On the other hand, tritium is not stable and has a half-life of about 12.3 years. Therefore it does not occur naturally. It is possible to breed tritium from lithium using neutron induced fission reactions directly in the reactor wall. Hence, no transportation would be required, which is beneficial for the operational safety. Furthermore, lithium occurs more homogeneously in the crust of the Earth in comparison with fossil fuels, so no political

concerns regarding lithium supply should appear. The currently known reserves allow electricity generation for several thousand years with present world's energy consumption [33].

Further advantages of fusion technology in comparison with fission are the safety aspects and waste handling. In a future fusion reactor only a small quantity of fuel is present at a time. Additionally, the fusion reaction requires precise conditions in order to proceed. Therefore, in case of a failure, the fusion reaction will stop automatically. Radioactive material is present in a fusion device as tritium and as induced radioactivity in structural materials, by the absorption of neutrons. However, in contrast to fission waste products the half-life of fusion waste is short and after about 100 years [25] most of these materials can be recycled for use in future fusion plants.

1.1. Thermonuclear Fusion

Fusion is the process, when multiple nuclei are joined together and form a heavier nucleus. The mass of the fusion product is not exactly the sum of the mass of the initial nuclei, since it depends on the nuclear binding energy. As can be seen in Figure 1.1a the average binding energy per nucleon increases up to iron. Thus, the mass of the fusion product of two light nuclei will be less than the total mass before the reaction. According to Einstein, this mass deficit is released as energy. Especially light nuclei have the best ratio of gained energy per fuel mass, which is several times better than for fission.

In order to perform fusion it is necessary to overcome the repulsive Coulomb potential between the particles. Therefore, the nuclei need enough kinetic energy, which can be provided by heating the particles to very high temperatures. This is called thermonuclear fusion. At these temperatures the kinetic energy of the particles becomes much larger than the atomic binding energy and electrons will be separated from the nuclei. The fuelling gas becomes a plasma, which consists of positive charged ions and negative electrons. The electrostatic charge of the ions is neutralized by the presence of an equal number of electrons, resulting in a quasi neutrality of the plasma.

The fusion reaction rate can be determined by the cross section, which strongly depends on the energy. The cross section of a proton-proton reaction appears to be very small, since it involves weak interaction. So this reaction cannot be used for energy production on Earth. Larger cross sections are available for the hydrogen isotopes deuterium and tritium.

Furthermore the temperature distribution of the heated particles has to be considered, for the calculation of reaction rate $\langle\sigma v\rangle$ (where v represent the relative velocity), since essential reactions occur in the high energy tail of the Maxwellian distribution [47]. The reaction rate is shown in Figure 1.1b.

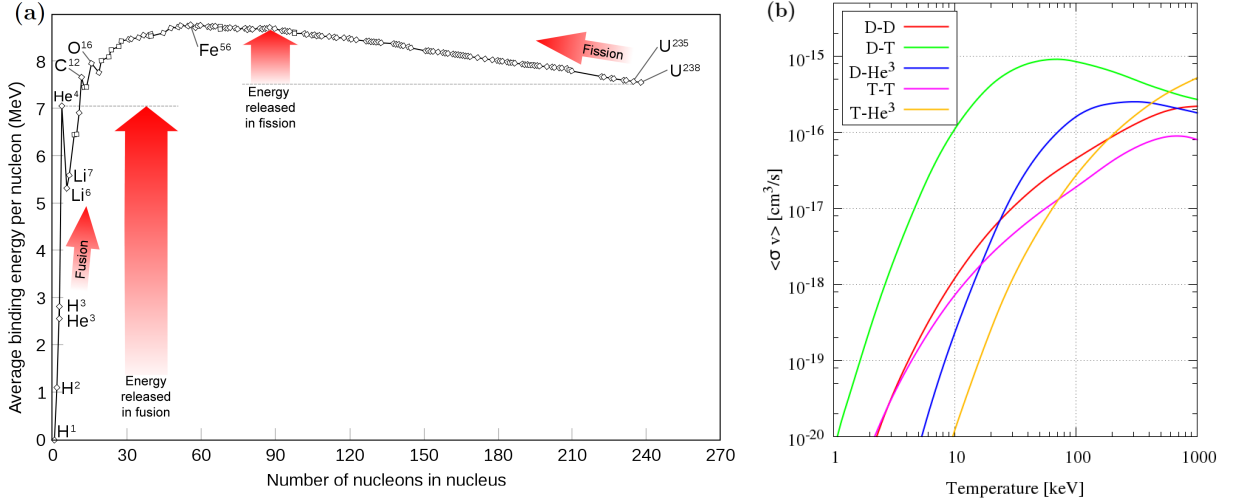


Figure 1.1: (a) The average binding energy per nucleon. (b) Reaction rate parameter for possible fusion reactions. [19]

It is easy to see that $D-T$ has the largest reaction rate of all fusion processes at the *lowest* temperatures, with a maximum at 64keV ($1eV \approx 11700 K$). This makes it the ideal candidate for energy production.

If the energy gain from the fusion reactions cannot compensate the energy loss of the fusion plasma, the temperature will decrease and the fusion process will stop without external heating. Therefore fusion can only be sustained if the energy confinement time is sufficiently long. One desirable goal of fusion research is achieving conditions under which the plasma is self-sustained, without the need for external heating. This is called ignition. Lawson derived a criterion, which describes the minimum conditions for ignition [26]. In the case of the $D-T$ reaction the ignition conditions are¹:

$$n \cdot \tau_E \cdot T > 5 \cdot 10^{21} \frac{keV \cdot s}{m^3} \quad (1.2)$$

with the particle density n , temperature T and the energy confinement time τ_E . Due to the temperature dependence of both, the energy loss of the plasma and the reaction rate,

¹For the central value of parabolic density and temperature profiles[47]

it can be shown that the optimum temperature for controlled fusion is about $10 - 20$ keV, which is between $100 - 250$ Mio. K [47].

1.2. Magnetic Confinement and Tokamak

There are no materials available, which can be used for the plasma confinement at such high temperatures. So one has to find an approach to confine the plasma for fusion without wall contact. The electrostatic charge of plasma particles allows to create a magnetic trap due to the Lorentz force:

$$\mathbf{F}_{Lorentz} = q \cdot (\mathbf{v} \times \mathbf{B}) \quad (1.3)$$

Without a magnetic field plasma particles move arbitrarily in all directions. If a magnetic field \mathbf{B} is applied, a charged particle will feel a force, which is perpendicular to \mathbf{B} and the particle velocity \mathbf{v} . Hence, plasma particles will gyrate around the magnetic field lines with the cyclotron frequency $\omega_c = \frac{qB}{m}$.

Closing the field lines circularly to a torus will confine the plasma particles avoid end losses. But this alone is not sufficient to enable a stable operation in a fusion device. Due to the bending of the torus the magnetic field is inhomogeneous and the gradient of the magnetic field will lead to charge dependent particle drifts. Hence, electrons and ions will be separated, which will lead to an electric field. Together with the magnetic field this will cause an $\mathbf{E} \times \mathbf{B}$ drift of the plasma. The drift is directed radially outwards for all particles in the plasma, preventing a stable operation. This problem can be solved by twisting the magnetic field lines with an additional magnetic field, thereby generating a helical field structure.

Several types of magnetic confinement devices are currently of scientific interest. The most important are the stellarator and the tokamak. The stellarator achieves the helical field structure with a rather complicated design of magnetic field coils, whereas the tokamak design uses an electric current in the plasma. The name tokamak is derived from *Toroidal'naja Kamera s Magnitnymi Katushkami*, which means: toroidal chamber with magnetic coils. The tokamak design was proposed in Russia by Tamm and Sakharov in the early 1950s [4]. A schematic drawing of a tokamak is shown in Figure 1.2. The tokamak has an axially symmetric form, which is shaped like a torus. Several toroidal field coils produce a strong toroidal magnetic field B_t , which avoids end-losses and de-

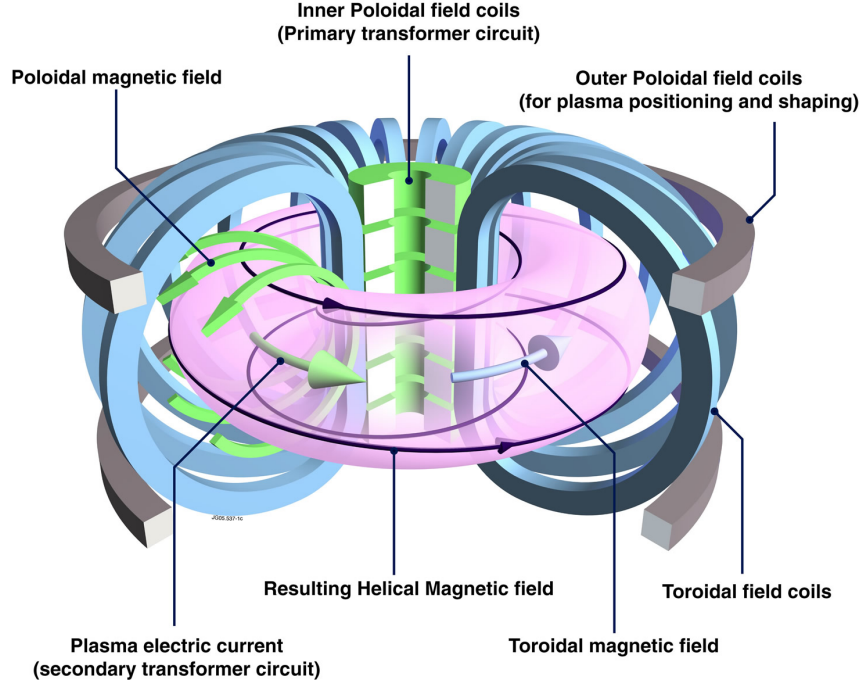


Figure 1.2: Schematic representation of the main components of the tokamak. The toroidal field coils (blue) create the toroidal magnetic field. A primary transformer circuit (green) induces a current in the plasma. The outer poloidal field coils (grey) are used for the shaping and the positioning of the plasma. [JET-EFDA]

defines the basic torus form. A central transformer coil uses the plasma as a secondary winding and induces a loop voltage around the torus and with this an electric current in the plasma. Consequently, the tokamak is a pulsed device. The electric current serves to create a poloidal magnetic field B_p , which results, together with the toroidal magnetic field, in a helical magnetic structure. Additionally the electric current is used for ohmic plasma heating. Due to the decreasing plasma resistivity for increasing temperature, ohmic heating cannot be used to reach the temperatures required for fusion. Other methods for heating are the injection of fast neutral particles (NBI) or the injection of electromagnetic waves, which are resonant to the cyclotron frequency of the ions (ICRH) or electrons (ECRH).

1.3. Importance of Plasma and MHD Mode Rotation

In order to achieve ignition, the plasma must fulfil certain criteria. One is the high confinement time of energy. This is achieved if the energy, which is put into the plasma, stays sufficiently long inside the plasma. The confinement in a tokamak depends on the

radial transport of energy. Empirically it is observed, that the energy transport increases with increasing power input. It is widely accepted that turbulence is responsible for the increased energy transport. It has been observed experimentally [8] and in simulations [40] that plasma rotation can influence the confinement, because turbulence can be suppressed with increased rotational shear. Furthermore, rotational shear does not only improve the confinement, it improves also the stability regarding the excitation of magnetohydrodynamic instabilities [9], which are called MHD modes. Therefore, a good understanding of plasma rotation and a high rotational shear could be important for the improvement of the plasma confinement and stability.

In specific cases large MHD modes can occur, leading to a strong degradation of the confinement. Furthermore, an MHD mode can lock to a static magnetic perturbation, come to standstill, grow and cause a disruption, which is a fast, total loss of confinement [5]. The confinement loss results in a high heat load on the walls. Furthermore, the termination causes a fast current decrease, which induces large structural forces. This can strongly damage the tokamak. Therefore, it is crucial to have a good knowledge about MHD modes, especially about their appearance and their motion in a tokamak.

1.4. Motivation and Outline

The rotation of MHD modes in a fast rotating plasma is assumed to be dominated by the plasma rotation. It is expected that in case of resistive MHD modes (magnetic islands) an additional offset velocity should be added, due to the electron diamagnetic drift. The reason will be explained in the next chapter. However, earlier studies at ASDEX Upgrade² and other tokamak experiments have shown that further contributions have to be considered as well [35], [16]. Currently, it is not exactly understood, which physical mechanisms influence the MHD mode rotation in the plasma. A closer investigation of island rotation in the tokamak ASDEX Upgrade is the goal of this thesis.

The thesis is structured as follows. The second chapter describes the basic theoretical framework, which is necessary for the understanding of the work. The equipment used for this thesis is introduced in the third chapter. It will describe ASDEX Upgrade, where the work was carried out and explain the diagnostic tools, which are used for the measurements of the plasma rotation and the determination of required plasma properties. Now that the theory and the diagnostics are introduced, chapter four will continue with

²ASDEX stands for *Axially Symmetric Divertor EXperiment*

the methodological approach in order to specify the characteristics of MHD modes. Additionally, the plasma rotation and the determination of the electron diamagnetic frequency are described. Chapter five presents the first results of the comparison of MHD mode and plasma rotation. It will show the deviation of MHD mode rotation to the plasma rotation and present possible interpretations. Furthermore, it is assumed that the neoclassical toroidal viscosity (NTV) must be considered, in order to explain MHD mode rotation in a tokamak. This will be investigated in the chapter six. Finally, a summary, a conclusion and an outlook will be given in the last chapter.

Chapter 2.

Theoretical Principles

This chapter will give an overview over the essential physics, which are helpful for the investigation of MHD mode rotation. It will start with the basic principles of plasma physics and give a short introduction to this topic. Afterwards, the tokamak equilibrium and important plasma parameters will be explained, followed by the magnetohydrodynamic stability, plasma rotation, MHD mode rotation and the neoclassical toroidal viscosity. A summary is given at the end of this chapter. More detailed introductions can be found in the literature [15], [47], [23], [14].

2.1. Introduction

The motions of a many particle system, like a plasma, can be described by kinetic theory. Because of the large number of particles involved, the description has to be statistical. This is carried out using a distribution function $f_\alpha(\mathbf{x}, \mathbf{v}, t)$, which represents the population density of the particles of type α , where \mathbf{x} describes the position and \mathbf{v} the velocity. The distribution function can change as a result of forces and collisions. The proper kinetic equation for a plasma is [47]:

$$\frac{\partial f_\alpha}{\partial t} + \mathbf{v} \cdot \nabla f_\alpha + \frac{q_\alpha}{m_\alpha} \cdot (\mathbf{E} + \mathbf{v} \times \mathbf{B}) \cdot \nabla_{\mathbf{v}} f_\alpha = \left(\frac{\partial f_\alpha}{\partial t} \right)_c \quad (2.1)$$

where \mathbf{E} and \mathbf{B} represent the macroscopic electric and the magnetic field in the plasma and $\left(\frac{\partial f_\alpha}{\partial t} \right)_c$ considers the collisions. This is also known as the *Fokker-Planck equation* (or *Vlasov equation* in the case of an ideal plasma, where there are no collisions $\left(\frac{\partial f_\alpha}{\partial t} \right)_c = 0$). For a full description of the plasma this equation has to be solved together with the Maxwell equations. In most cases we are interested in macroscopic physical properties of

the plasma and not in the particle distribution. This can be described by the moments of the distribution function leading to simplified equations¹. A physical property $\langle A \rangle$ corresponds to a moment of the function:

$$\langle A \rangle = \frac{1}{n_\alpha} \int A f_\alpha d\mathbf{v} \quad (2.2)$$

where $n_\alpha(\mathbf{x}, t) = \int f_\alpha(\mathbf{x}, \mathbf{v}, t) d\mathbf{v}$ is the local density of particle α . By the calculation of the moments of equation 2.1 we obtain:

$$\frac{\partial n_\alpha}{\partial t} + \nabla \cdot (n_\alpha \mathbf{v}_\alpha) = 0 \quad (2.3)$$

$$m_\alpha n_\alpha \left(\frac{\partial \mathbf{v}_\alpha}{\partial t} + \mathbf{v}_\alpha \cdot \nabla \mathbf{v}_\alpha \right) = -\nabla p_\alpha + n_\alpha q_\alpha (\mathbf{E} + \mathbf{v}_\alpha \times \mathbf{B}) + R_{\alpha\beta} \quad (2.4)$$

where \mathbf{v}_α is the center of mass velocity, $R_{\alpha\beta}$ represents the collision operator with other particles and p_α the pressure tensor, which becomes a scalar quantity if isotropic pressure is assumed². Equation 2.3 is the continuity equation and equation 2.4 the force equation of particle α .

In magnetohydrodynamics (MHD) the equations for ions and electrons can be combined into a one fluid model in order to describe the plasma. The mass density is given as $\rho = n_i m_i + n_e m_e$ and the center of mass velocity as $\mathbf{v} = \frac{n_i m_i \mathbf{v}_i + n_e m_e \mathbf{v}_e}{n_i m_i + n_e m_e}$. It is clear that $m_e \ll m_i$ and we know for a $D-T$ plasma $n = n_i = n_e$ due to quasi neutrality. From this, it follows that $m \approx m_i$, $\rho \approx nm$ and $\mathbf{v} \approx \mathbf{v}_i$. By analysing the momentum equations one can see, that each equation includes the next higher momentum. To reach a closed set of equations, the plasma behavior is assumed to be adiabatic and reversible:

$$\frac{d}{dt} \left(\frac{p}{\rho^\gamma} \right) = 0 \quad (2.5)$$

Here, γ is the adiabatic coefficient³. With this, the MHD equations can be derived [15]:

$$\frac{\partial \rho}{\partial t} + \nabla \cdot (\rho \mathbf{v}) = 0 \quad (\text{mass conservation}) \quad (2.6)$$

$$\rho \cdot \left(\frac{\partial \mathbf{v}}{\partial t} + (\mathbf{v} \cdot \nabla) \mathbf{v} \right) = \mathbf{j} \times \mathbf{B} - \nabla p \quad (\text{momentum conservation}) \quad (2.7)$$

¹This simplification neglects the kinetic effects of the particle distribution, since particles with different velocities react differently to external fields (e.g. Landau damping).

²The scalar pressure in plasma physics is defined via the density n and the temperature T as $p = n \cdot T$.

³For an ideal gas with $n = 3$ degrees of freedom $\gamma = \frac{n+2}{n} = \frac{5}{3}$

$$\mathbf{E} + \mathbf{v} \times \mathbf{B} = \eta \mathbf{j} + \frac{1}{en_e} (\mathbf{j} \times \mathbf{B} - \nabla p) \quad (\text{generalized Ohm's law}) \quad (2.8)$$

where \mathbf{j} is the electric current, p the total plasma pressure and η the plasma resistivity. Gravity is neglected in these equations. Together with the four Maxwell equations

$$\nabla \cdot \mathbf{E} = \frac{\rho}{\varepsilon_0} \quad (\text{Gauss's law}) \quad (2.9)$$

$$\nabla \cdot \mathbf{B} = 0 \quad (\text{Gauss's law for magnetism}) \quad (2.10)$$

$$\nabla \times \mathbf{E} = -\frac{\partial \mathbf{B}}{\partial t} \quad (\text{Faraday's law}) \quad (2.11)$$

$$\nabla \times \mathbf{B} = \mu_0 \mathbf{j} + \mu_0 \varepsilon_0 \frac{\partial \mathbf{E}}{\partial t} \quad (\text{Ampère's law}) \quad (2.12)$$

and the adiabatic constraint this forms a complete set of MHD equations, which have to be solved simultaneously in order to describe the plasma correctly. Here, ε_0 and μ_0 is the electric and the magnetic constant, respectively.

There are some consequences of the MHD equations if the plasma is assumed to be ideal. This is the case if the resistivity is negligible $\eta \approx 0$. Using equation 2.8 with $\eta \rightarrow 0$ and neglecting the time dependence it can be derived that the magnetic flux is *frozen* in the plasma fluid [15]. Using a two fluid model it can be shown, that the magnetic flux is *frozen* in the electrons [50].

2.2. Tokamak Equilibrium

One application of the MHD equations is the description of a magnetic equilibrium. For an equilibrium we can demand for the time derivatives to be negligible, thus $\frac{\partial}{\partial t} \approx 0$. Additionally, in ideal MHD equations the resistivity and viscosity are negligible. In this case equation 2.7 together with 2.6 becomes:

$$\mathbf{j} \times \mathbf{B} = \nabla p \quad (2.13)$$

This equation is the ideal force balance equation. It shows that a pressure gradient in a plasma can be sustained by an electric current. It can be easily seen from equation 2.13 that the pressure gradient is perpendicular to the magnetic field and the electric current, thus $\mathbf{j} \cdot \nabla p = 0$ and $\mathbf{B} \cdot \nabla p = 0$. In an axisymmetric case, this forms a set of radially nested surfaces with constant pressure. Also the electric current lines lie on these surfaces. A schematic representation of such magnetic surfaces is illustrated in Figure 2.1.

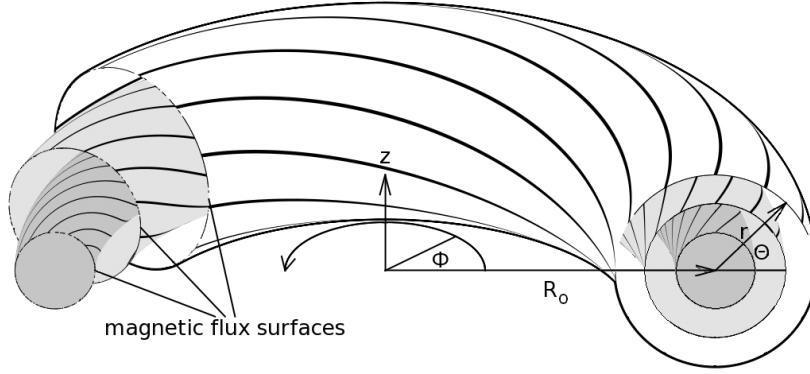


Figure 2.1: Magnetic flux surfaces in a tokamak. The toroidal geometry can be described with the major radius R_0 of the magnetic axis, the minor radius r , the toroidal angle Φ and the poloidal angle Θ .

For a profound description of the tokamak equilibrium it is useful to introduce the poloidal magnetic flux function Ψ . This function is determined by the poloidal magnetic flux within the magnetic surface. Thus, the poloidal magnetic flux is also constant on that surface and Ψ can be written as [47]:

$$\mathbf{B} \cdot \nabla \Psi = 0 \quad (2.14)$$

The helical winding of a magnetic field line on a magnetic flux surface is described by the so called *safety factor* q , which specifies the number of toroidal windings needed, to perform one poloidal rotation. If the q -factor is 1, a magnetic field line needs one rotation around the torus to return to its poloidal starting position. The exact definition of q is [47]:

$$q = \frac{\Delta \Phi}{2\pi} \quad (2.15)$$

where $\Delta \Phi$ is the toroidal angle needed for a poloidal circulation. For a large-aspect ratio⁴ tokamak with a circular cross-section the cylindrical approximation can be made, resulting in:

$$q \simeq \frac{r B_\Phi}{R_0 B_\Theta} \quad (2.16)$$

where r is the minor radius of the magnetic surface, B_Φ the toroidal magnetic field⁵, R_0 the major radius of the magnetic axis and B_Θ the poloidal magnetic field.

⁴The aspect ratio is given by the ratio between the major radius R_0 and the minor radius at the plasma boundary a of a tokamak.

⁵ B_Φ is constant in the cylindrical approximation.

Another important parameter in the tokamak is β . It describes the plasma pressure, which can be confined by the magnetic field as:

$$\beta = \frac{\langle p \rangle}{B^2 / 2\mu_0} \quad (2.17)$$

where $\langle p \rangle$ is the averaged kinetic pressure. This factor is a quantity for the efficiency of a magnetic confinement, since plasma pressure essentially influences the fusion performance, while the square of the magnetic field determines mainly the cost of the fusion reactor.

2.3. Neoclassical Theory and Trapped Particles

In a tokamak the toroidal coils on the inner side are closer together. Hence, the toroidal magnetic field is higher on this side and decreases with increasing radius R as: $B_\phi \propto \frac{1}{R}$. Therefore, the inner side in a tokamak is called *high field side* (HFS) and the outer *low field side* (LFS). As it was already mentioned, the particles gyrate along the field lines. The particle velocity can be split in a parallel part v_\parallel and a perpendicular part v_\perp to the magnetic field line. Due to their perpendicular motion, charged particles have a magnetic moment in a magnetic field:

$$\mu = \frac{mv_\perp^2}{2B} \quad (2.18)$$

It can be shown, that the magnetic moment is constant for a particle. Because of this reason, v_\perp will increase if a particle moves into a higher magnetic field. At the same time, v_\parallel will decrease due to energy conservation. If v_\parallel reaches 0, the particle will be reflected. This is known as a magnetic mirror. The condition for reflection is:

$$\frac{v_\parallel^2(R_0 + r)}{v_\perp^2(R_0 + r)} < \frac{B_{max}}{B_{min}} - 1 \quad (2.19)$$

Particles with an adequate ratio of v_\perp^2/v_\parallel^2 will be reflected, while moving from the LFS to the HFS instead of circulating around the torus. These particles are called *trapped particles*. The effects which act on the trapped particles are described in the so called *neoclassical theory*. The motion of trapped particles will result in a banana like orbit (see Figure 2.2) due to the superposition of the curvature drift⁶ and the ∇B drift⁷.

⁶Curvature drift: $\mathbf{v}_D = -\frac{mv_\parallel^2}{qB^3} \nabla B \times \mathbf{B}$

⁷ ∇B drift: $\mathbf{v}_D = -\frac{mv_\perp^2}{2qB^3} \nabla B \times \mathbf{B}$

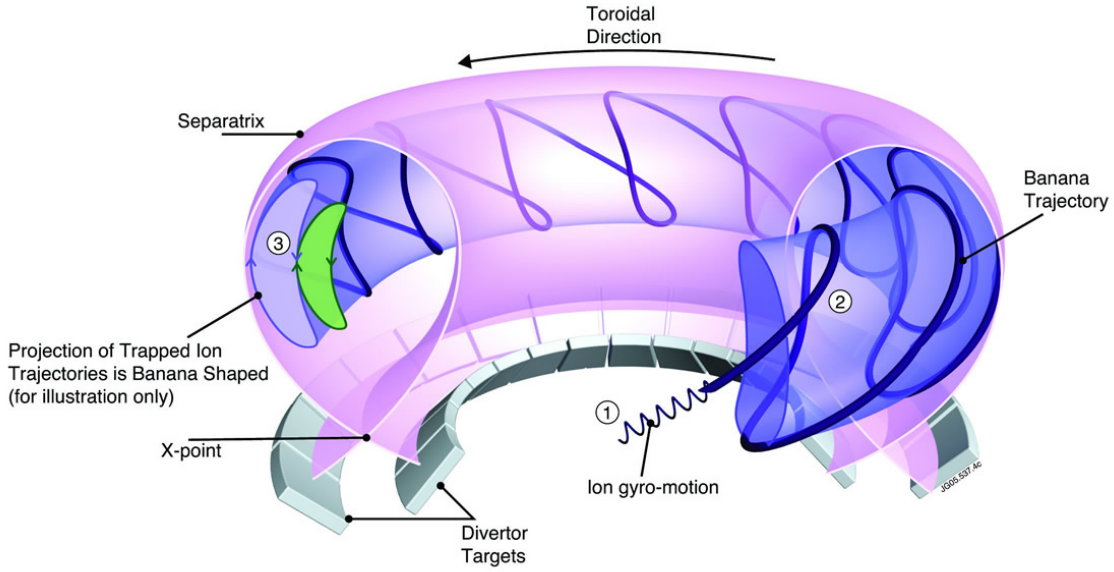


Figure 2.2: Schematic representation of the trajectory of the trapped particle in the tokamak. (1) Gyro-motion of an ion. (2) Banana orbit trajectory. (3) Poloidal cross-section profile of two banana orbits. [JET-EFDA]

There are several important implications from the neoclassical theory. One effect is the *bootstrap current*. This is an electric current, which is produced by trapped particles in the presence of a pressure gradient in the plasma [15]. The origin of the bootstrap current can be explained by comparing the touching point of an inner and an outer banana orbit (see (3) in Figure 2.2). If the inner orbit has a higher density than the outer orbit, more particles move in the direction of the inner orbit at the touching point. If the inner orbit has a higher temperature than the outer orbit, the particles from the inner orbit will move faster. Also in this case, the total particle flow at the touching point will be in the direction of the inner orbit. Both effects will generate an electric current in the toroidal direction. An additional contribution to the bootstrap current stems from the free particles which are accelerated due to collisions with the trapped particles [15].

2.4. Magnetohydrodynamic Stability and MHD Modes

To operate a fusion device, we need not only a good confinement, it should also be stable. The stability analysis can be done in MHD by the calculation of a plasma response to a small perturbation. We can say that if the potential energy decreases due to this perturbation, an instability may grow. Thus, the equilibrium will be unstable. On the

other hand, if the energy increases due to this deviation, the equilibrium will be stable. But this perturbation can still cause an oscillation and stimulate a variety of waves in the plasma.

The destabilising forces in the MHD are driven by the electric current and pressure gradients. Magnetic field compression and line bending act as stabilizing terms. The appearance of an instability is often described either as a small displacement $\boldsymbol{\xi}$ of a fluid element in the plasma or as an initial displacement velocity⁸ $\mathbf{v}_1 = \frac{d\boldsymbol{\xi}}{dt}$. The linearised and integrated perturbation equations are then derived from ideal MHD [50]:

$$\rho_1 = -\nabla \cdot (\rho_0 \boldsymbol{\xi}) \quad (2.20)$$

$$p_1 = -p_0 \gamma \nabla \cdot \boldsymbol{\xi} - \boldsymbol{\xi} \cdot \nabla p_0 \quad (2.21)$$

$$\mathbf{B}_1 = \nabla \times (\boldsymbol{\xi} \times \mathbf{B}_0) \quad (2.22)$$

Equation 2.20 originates from the mass conservation and describes the density perturbation ρ_1 (compression of a volume element). An adiabatic compression or a displacement of the volume element causes a pressure perturbation p_1 , which is described by equation 2.21. The combination of Faraday's law and the ideal Ohmic law gives the magnetic perturbation in equation 2.22. It shows that a volume displacement cause a perturbation of the magnetic \mathbf{B}_1 field [50]. The force equation can be obtained from the displacement vector as:

$$\mathbf{F}(\boldsymbol{\xi}) = \rho_0 \frac{d^2 \boldsymbol{\xi}}{dt^2} = \mathbf{j}_1 \times \mathbf{B}_0 + \mathbf{j}_0 \times \mathbf{B}_1 - \nabla p_1 \quad (2.23)$$

and consequently the energy change is

$$dW = -\frac{1}{2} \int \boldsymbol{\xi} \cdot \mathbf{F} dV \quad (2.24)$$

The sign of dW gives the stability criterion. The plasma will be unstable if dW is negative, and stable if dW is positive. Furthermore, the differential equation 2.23 represents an equation of motion, which can be solved to determine the mode structure. The calculation of the eigenfunction $\boldsymbol{\xi}$ determines the form of the mode and the corresponding eigenvalue the stability [47].

There is a large variety of possible MHD modes in a tokamak. MHD modes are characterised by the poloidal number m and the toroidal number n , which describe the helical

⁸ Index 1 means, that this quantity is a perturbation with respect to the equilibrium.

mode structure. They occur on the rational $q = \frac{m}{n}$ values. At these surfaces a small resonant fluctuation can be amplified. Therefore, magnetic flux surfaces with rational q -values are called *resonant surfaces*. Furthermore, the frequency f describes the rotation of the mode in the laboratory frame and the displacement of a magnetic field due to the mode is described by the radial eigenfunction ξ , which depends on the MHD mode type and varies with the minor plasma radius [21].

One important ideal MHD mode is the (1/1) internal kink, because the topology of the perturbation is similar to the topology of the equilibrium [50]. This enables the formation of such modes without the modification of the plasma topology. An illustration of (1/1) kink modes is shown in 2.3. Such MHD modes occur often if the central q -values are smaller than 1 (e.g. in [21]).

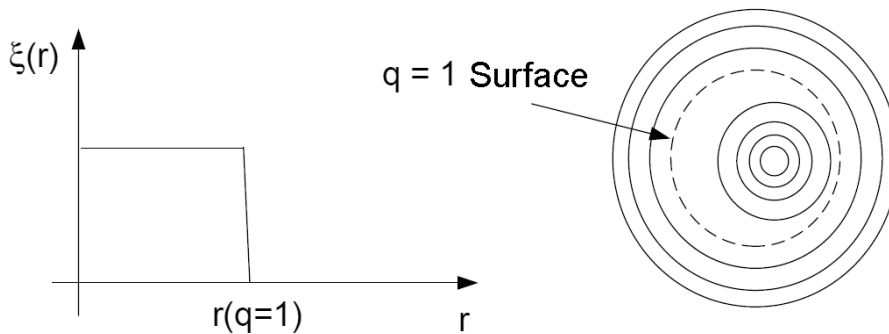


Figure 2.3: The eigenfunction of an internal (1,1) kink mode. The magnetic field lines are shifted inside the $q = 1$ surface.

Another type of instabilities are the resistive MHD modes, which depend on the finite resistivity of the plasma at resonant surfaces. Considering the resistivity ($\eta \neq 0$) in Ohm's law results in the dissipation of magnetic flux, due to an electric current perturbation. This allows the magnetic field lines to tear apart and reconnect, creating a changed topology of the magnetic structure [50].

One of the most common resistive instabilities is the *tearing mode* or *magnetic island*, which occurs on magnetic flux surfaces with rational q -values. The formation of an (m/n) magnetic island can be explained by an electric current perturbation on the $q = \frac{m}{n}$ flux surface, which creates an additional poloidal magnetic field. This perturbation leads to the reconnection of the flux surfaces and forms the typical structure of a magnetic island (see Figure 2.4).

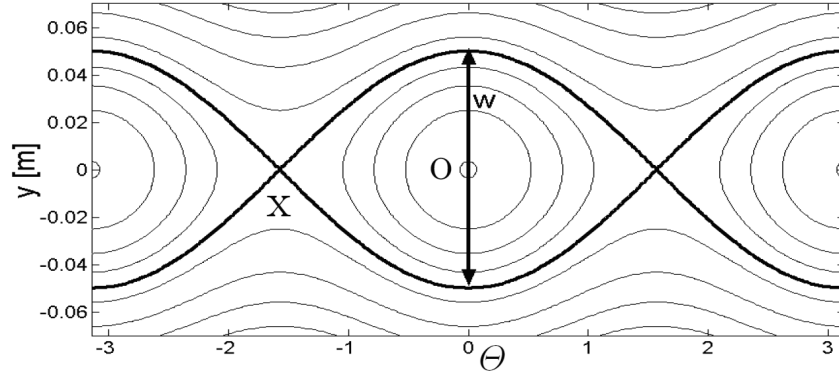


Figure 2.4: The helical flux function for a (2/1) island in a poloidal Θ - radial y plane. Two poloidal O-points with a 10 cm radial width W are formed in the poloidal profile. The island separatrix is indicated as the thick black line. [5]

An island can be seen as a helical flux tube, closing itself after m toroidal and n poloidal rotations. The reconnected flux surfaces are called *separatrix* and embed the island. The reconnection point of the magnetic flux is marked by the X-point and the center by the O-point. The largest extension of the island can be identified as the island width W .

Tearing modes are important for the tokamak, because they connect different radial positions of the plasma due to their spatial structure. Hence, they act as short-circuit regarding radial energy transport. Therefore islands flatten the pressure profile at their location, which decreases the energy confinement and reduces the performance of the tokamak. Another consequence, which can be derived in the neoclassical theory, is a reduction of the bootstrap current. Especially, in high β discharges a small seed island⁹ can cause a loss of bootstrap current, which may lead to further island growth [31]. This mode is called *Neoclassical Tearing Mode* (NTM) and limits the maximum β , which can be achieved in a tokamak.

2.5. Plasma Rotation

The rotation of a plasma is mainly dependent on the flow of the ions in the plasma, due to their higher mass. For the description of the plasma rotation it is useful to begin with the first moment equation 2.4. For a stationary situation, we can assume no time dependence ($\frac{\partial}{\partial t} \approx 0$). Additionally, we can neglect the momentum exchange with other species ($R_{ie} = 0$), since the momentum exchange is much smaller between ions and elec-

⁹Such a seed island can be generated e.g. by a sawtooth crash, which is an other (1/1) resistive instability.

trons than between ions and ions, due to $m_e \ll m_i$ [15]. In this approximation equation 2.4 can be written as:

$$\nabla p_i = en_i \cdot (\mathbf{E} + \mathbf{v}_i \times \mathbf{B}) \quad (2.25)$$

This equation can be solved for \mathbf{v}_i by taking the cross product with the magnetic field together with the *triple product expansion*:

$$\mathbf{v}_i = \frac{\mathbf{E} \times \mathbf{B}}{B^2} - \frac{1}{n_i e} \frac{\nabla p_i \times \mathbf{B}}{B^2} + \mathbf{v}_{i\parallel} \quad (2.26)$$

The first term to the plasma rotation is the $\mathbf{E} \times \mathbf{B}$ drift, which describes the motion of the gyrocentres. The second term on the right hand side is the so called *diamagnetic drift*. The diamagnetic drift is a contribution, which results from the particle gyration in the presence of a temperature or a density gradient. This process is shown in figure 2.5 and can be understood as the following: If there is a decreasing radial density in the plasma, there are more particles on the inner side of a surface. Thus, more particles will gyrate through a surface on the inner side, than on the outer side. The addition of all particle gyrations through a surface will leave a net flow, even if the gyrocentres do not move. There is a similar effect in the presence of a temperature gradient. The difference here is the gyration velocity. *Warmer* particles gyrate faster than *colder* particles, which also results in a net fluid motion.

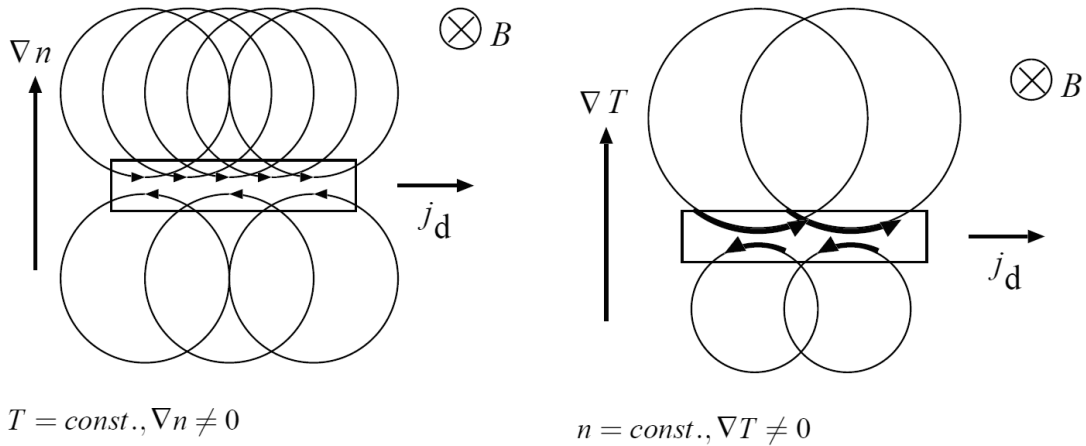


Figure 2.5: Principle of the diamagnetic drift. In the presence of density and temperature gradients there is a net fluid current \mathbf{j}_d [44].

In order to get a profound description of the plasma rotation, it is necessary to consider further effects. In particular neutral particles can lead to an external contribution to the plasma rotation. The injection of neutral particle beams, which have a large toroidal velocity is currently the main source for plasma rotation. After entering the plasma, neutral particles will be ionized and subsequently induce momentum into the plasma via collisions. The total amount of the momentum deposition depends on the angle of incidence of the beam as well as the energy and number of injected neutral particles in the tokamak. Furthermore, *cold* neutral particles from the edge will slow the plasma rotation. These additional forces can be added on the right hand side of equation 2.25 for the plasma rotation determination.

To achieve a more detailed rotation description, also the radial dispersion of the velocity has to be considered, which requires the determination of the momentum transport. This can be done if the non isotropic pressure tensor and the $(nm\mathbf{v} \cdot \nabla\mathbf{v})$ part of equation 2.4 are included. This consideration will lead to an angular momentum balance equation, which can be used to calculate the toroidal rotation profile in a tokamak. Calculations for the momentum transport can be found in literature, e.g. [9],[39].

2.6. MHD Mode Rotation

The rotation of MHD modes in a fast rotating plasma is dominated by the toroidal plasma velocity. Additionally, ideal MHD theory (with the Hall term) predicts that the magnetic flux topology is *frozen* in the electron fluid, as it was introduced in section 2.1. Therefore, the electron diamagnetic drift $\mathbf{v}_{dia,e}$ should contribute to the island rotation.

$$\mathbf{v}_{dia,e} = \frac{1}{en_e} \frac{\nabla p_e \times \mathbf{B}}{B^2} \quad (2.27)$$

Since, the measured mode frequency is a projection of the rotation in toroidal and poloidal directions, it will depend on the magnetic field lines and the rotation direction, whether the electron diamagnetic drift frequency has to be added or subtracted to the plasma rotation frequency. There are four possible combinations, which are sketched in Figure 2.6.

Because of a large B_ϕ component the electron diamagnetic drift is mainly in the poloidal direction. It can be seen in Figure 2.6 together with equation 2.27 that a magnetic field line on the LFS will move upwards for $B_\phi < 0$ and downwards for $B_\phi > 0$. The poloidal

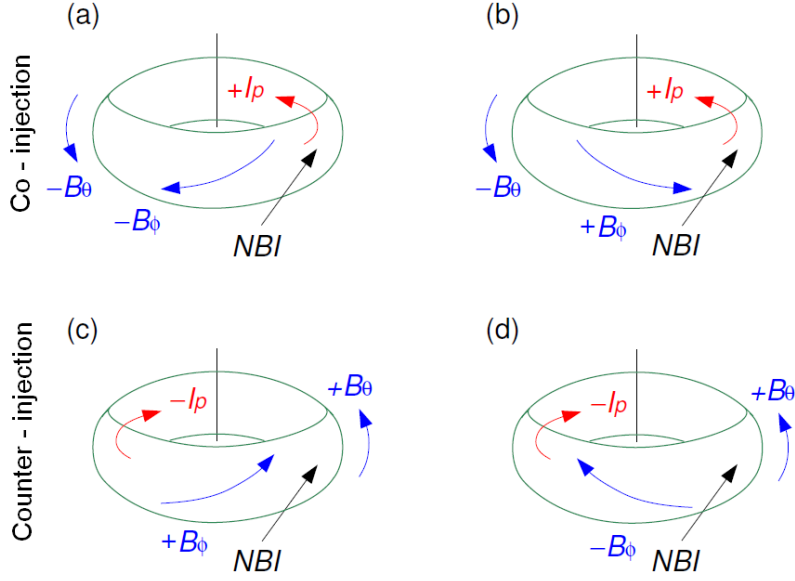


Figure 2.6: The direction of the toroidal magnetic field produce four different combinations with the current and NBI heating. The case when the current has the same direction as the NBI is called Co-Injection and the opposite is called Counter-Injection. [36]

upward rotation of the magnetic field line in Figure 2.6a has the same effect as a toroidal rotation of the magnetic field line, which is directed in the counter-current direction. These two effects cannot be separated in the experiment. Hence, the poloidal rotation of the magnetic field line acts as an additional counter-current rotation. This is also true for Figure 2.6b - Figure 2.6d. Hence, if the plasma rotates in current direction, which is the usual case in ASDEX Upgrade[36], the electron diamagnetic drift has to be subtracted. Hence, the island is expected to rotate slower than the ambient plasma.

Furthermore, the helical island structure implicates, that the detected frequency consists of n times the toroidal rotation frequency and m times the electron diamagnetic rotation frequency. Thus, the expected MHD mode frequency f_{mode} can be calculated as:

$$f_{mode} = n \cdot f_{plasma} - m \cdot f_{dia,e} \quad (2.28)$$

Equation 2.28 is often used in the literature, in order to describe MHD mode rotation [9],[5], [46]. However, earlier investigations of island rotation ([35], [16]) have shown, that magnetic islands can rotate faster than the ambient plasma. This indicates that the physics for MHD mode rotation is not yet completely understood. A possible explanation for this observation is given by the *Neoclassical Toroidal Viscosity* (NTV) theory.

2.7. Neoclassical Toroidal Viscosity

The NTV is caused by the interaction of the plasma with magnetic field components, which break the toroidal symmetry. A possibility to break the symmetry is the occurrence of MHD modes, which generate non axisymmetric magnetic field perturbations. The resonant perturbations produce a localized torque at its respective flux surface, whereas non resonant perturbations produce a global neoclassical torque that damps the toroidal plasma flow [6].

In the fluid model, the NTV drag can be described as a force on the plasma fluid, which occurs as it flows through the non axisymmetric field perturbation. The kinetic model describes the toroidal force by a non ambipolar drift of particles due to the non axisymmetric fields in a collisional plasma. This generates a radial current, which exerts a $\mathbf{j} \times \mathbf{B}$ torque. The torque is dominated by trapped particle drifts [48].

In order to obtain a quantitative expression for the NTV force for the collisionless plasma regime, one can solve the bounce averaged drift kinetic equation and then take the velocity moment to receive the radial flux. This derivation was carried out in [41] and expanded to rotating islands in [42]. One important consequence from the expansion is a toroidal offset velocity of MHD modes, which tries to keep the island rotation at a rate comparable to the ion diamagnetic flow [7]. The first explicit formulation of the toroidal neoclassical offset velocity was introduced by [6]:

$$\omega_{nc} = \frac{k}{Z_i e \bar{R} B_\theta} \cdot \frac{dT_i}{dr} \quad (2.29)$$

Here, Z_i is the charge of the main ion species, \bar{R} the major radius of the flux surface on the midplane at the LFS, B_θ the poloidal magnetic field and $\frac{dT_i}{dr}$ the ion temperature gradient. The factor k depends on the NTV regime of the plasma [7].

Two different regimes with low collisionality are described in [7]. The first is the so called $(1/\nu)$ -regime. The condition for this regime is $q\omega_E < \nu_{ii}/\epsilon < \sqrt{\epsilon}\omega_{ti}$, where ω_E is defined as the $E \times B$ poloidal drift frequency ($\omega_E = \frac{E_r}{rB}$) and $\omega_{ti} = \frac{v_{ti}}{R_0 q}$ the ion transit frequency with $v_{ti} \equiv (T_i/m_i)^{1/2}$. The quantity ν_{ii} describes the ion-ion collision frequency. In this regime the toroidally trapped particles are collisionless and dominate the nonambipolar diffusion process [7]. The factor k is $\simeq 3.5$ in the $(1/\nu)$ -regime.

The second regime is called (ν) -regime. Here, the collisionality decreases even more.

The condition for this regime is $\nu_{ii}/\epsilon < q\omega_E$. Here, the radial drift of ions becomes oscillatory and limited to the toroidal $\mathbf{E} \times \mathbf{B}$ precession drift [7]. [41] predicts that in present-day tokamaks it is unlikely that the ion temperatures are high enough to be deeply in the (ν) -regime. However, it is possible that ions can be slightly in this regime, while electrons are still in the $(1/\nu)$ -regime. In this limit, the ion NTV dominate over the electron NTV. The corresponding factor k is then $\simeq 0.92$ [7].

2.8. Summary

The plasma can be described by the theory of ideal MHD. The resulting equilibrium in a tokamak forms a helical structure of nested magnetic flux surfaces. Due to the toroidal geometry, the magnetic field is not homogeneous and trapped particles can occur if their ratio of perpendicular to parallel velocity is large enough. These particles move on the so called banana orbits. This implicates new effects, like the occurrence of the bootstrap current.

The stability of the equilibrium can be described via the energy principle. The plasma will be stable, if a perturbation increases the total energy, otherwise, the instability will grow. This can deteriorate or even destroy the confinement. Perturbations can be described by the displacement vector $\boldsymbol{\xi}$. The plasma instabilities are mainly driven by electric current and pressure gradients, while magnetic field compression and line bending act as stabilizing terms.

The plasma rotation can be described with the motion of the main plasma ions. In present-day tokamak experiments, the rotation is mainly driven by external forces, like neutral beam heating. The deposition of momentum, due to the neutral beam heating, depends on the beam's angle of incidence as well as the number and energy of injected neutral particles. The description of the exact rotation profile can be quite complex and requires the knowledge of the momentum diffusion coefficients and the influence of the external forces.

The rotation of magnetic islands is expected to be determined by the toroidal plasma rotation subtracted by the electron diamagnetic drift in ASDEX Upgrade. Additionally, the mode numbers have to be taken into account. Another possible contribution is predicted by the NTV theory due to a neoclassical toroidal torque and an offset velocity. The influence of NTV effects is investigated in this thesis.

Chapter 3.

ASDEX Upgrade and Diagnostics

This chapter will give an overview over the experiment ASDEX Upgrade, where this thesis was carried out. It will start with the description of the tokamak ASDEX Upgrade and its parameters. Afterwards, the diagnostics and their physics principals will be described.

3.1. ASDEX Upgrade

ASDEX Upgrade is a medium sized divertor tokamak experiment with a major radius of $R_0 = 1.65$ m and a minor radius of $a = 0.5$ m. The plasmas in ASDEX Upgrade have an elongated cross-section, which can be flexibly shaped. Furthermore, several current drive and heating systems are available. In particular, two different NBI heating systems with four beam lines each and various angles of incidence, which have a strong impact on the plasma rotation.

The goal of ASDEX Upgrade is the investigation of physics, which can improve the design and operation for the experiment ITER¹, which is the next step towards a commercial fusion power plant. The main focus for ASDEX Upgrade is the investigation of transport, exhaust, MHD stability and fast particle physics, but also various start-up and ramp-down scenarios for ITER are of particular interest [51]. Figure 3.1 shows the main components of ASDEX Upgrade.

ASDEX Upgrade can be operated with hydrogen, deuterium and helium as plasma fuel. In addition ASDEX Upgrade is the only tokamak, which has shown the possibility of operation with a full tungsten wall. This allows the investigation of tungsten as a

¹ITER is latin for *Way* or former *International Thermonuclear Experimental Reactor*

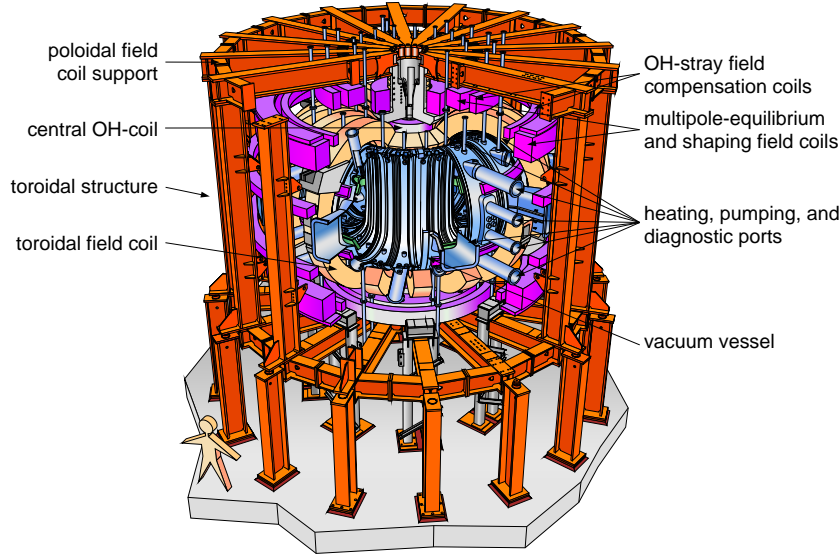


Figure 3.1: Illustration of the tokamak ASDEX Upgrade. [1]

wall material for future fusion devices. The usage of tungsten is beneficial because it can handle high temperatures and has a low retention of tritium. This is important for a commercial fusion power plant.

A typical plasma discharge in ASDEX Upgrade lasts for 7–10 s, has a toroidal magnetic field of 2.5 T on the magnetic axis, 1 MA of plasma current and a central electron density of about $9 \cdot 10^{19} \text{ m}^{-3}$. The parameters of ASDEX Upgrade are summarized in Table 3.1.

| | Identifier | Value |
|--------------------------------|----------------|-----------------------|
| Major plasma radius | R_0 | 1.65 m |
| Minor horizontal plasma radius | a | 0.5 m |
| Minor vertical plasma radius | b | 0.8 m |
| Ellipticity | $\kappa = b/a$ | 1.6 |
| Aspect ratio | R_0/a | 3.3 |
| Plasma volume | | 14 m^3 |
| Plasma current | I_p | $\leq 1.6 \text{ MA}$ |
| Maximum magnetic field | B | $\leq 3.1 \text{ T}$ |
| Pulse duration | | $\leq 10 \text{ s}$ |
| Time between pulses | | 15 – 20 min |
| Plasma heating: | P_{tot} | $\leq 27 \text{ MW}$ |

Table 3.1: Main parameters of ASDEX Upgrade. [1]

3.2. Charge Exchange Recombination Spectroscopy

In order to measure plasma rotation *Charge eXchange R*ecombination *S*pectroscopy (CXRS) is an important tool. CXRS measures the line-emission of excited ions in the plasma and allows the determination of ion temperature from the line broadening and the velocity from the shift of the line-emission due to the Doppler effect.

With the exception of heavy impurities, the ions in the plasma core are fully stripped of electrons due to the high temperature. Therefore, line radiation can only occur if a plasma ion receives an electron due to a charge exchange reaction with a neutral particle. An exchanged electron can occupy an excited state and release line-emission. For charge exchange recombination spectroscopy carbon ions can be used:



The most common state of C^{5+} for the electron is $n = 4$, but also $n = 7$ and $n = 8$ states have considerable populations [17]. Neutral atoms reach the plasma core only by the means of neutral beam injection. Due to the usage of a beam, CXRS gives local information on the ion temperature and velocity.

The CXRS diagnostic in ASDEX Upgrade detects the transition from $n : 8 \rightarrow 7$ with the natural wave length of $\lambda = 529.0 \text{ nm}$. Alternatively, the diagnostic can use the boron ions B^{5+} with $\lambda = 494.5 \text{ nm}$. These wavelengths are in the optical range of light, which can be measured easily with common optical elements.

The particle velocity in the plasma is Maxwellian distributed, leading to a Gaussian broadening of the spectral emission, due to the Doppler effect. In the case of carbon and an ion temperature of 10 eV the Doppler broadening corresponds to about $5 \cdot 10^{-2} \text{ nm}$, which is well above the natural line width of about $5 \cdot 10^{-5} \text{ nm}$ for this transition [9]. Thus, the measurement of the full width half maximum of the Gaussian shaped spectrum can be used to determine the temperature. Furthermore, the plasma rotation results in a Doppler shift of the peak: $\lambda_{shift} = \lambda(1 + \frac{v_{rot}}{c})$. This enables the determination of the ion velocity.

An illustration of the toroidal CXRS geometry is shown in Figure 3.2. Two sources of the line emission can be identified. The active emission occurs due to charge exchange reactions with the neutral beam. Furthermore, C^{5+} ions also occur *naturally* in the edge of the plasma due the low temperature. This contributes as passive emission.

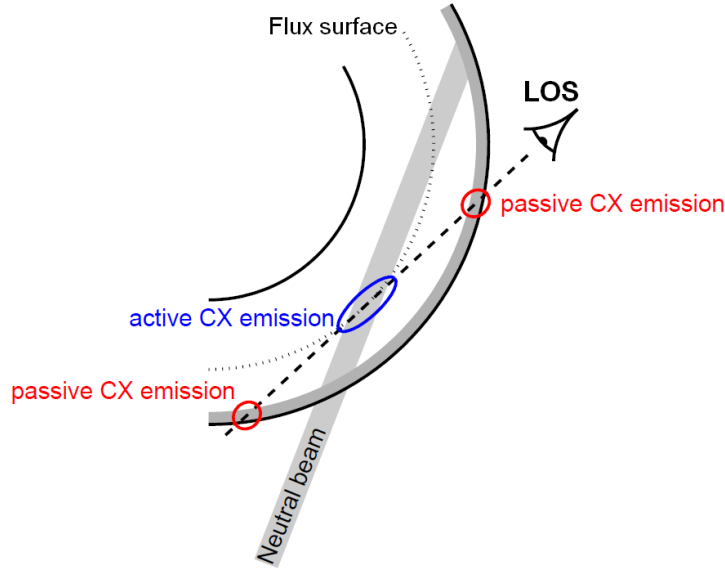


Figure 3.2: Line of sight (LOS) of CXRS in a toroidal cross section of a tokamak. The active signal originates from neutral beam heating, while the passive component occurs *naturally* due to lower temperatures and neutral particles in the edge. [9]

There are two methods to separate the passive and active emission. One method is the usage of a modulated beam. Here, the passive emission is measured when the beam is switched off and can be subtracted from the spectrum when the beam is switched on, leaving only the active emission. However, this can be done only if one assumes, that the neutral beam will not change the C^{5+} population at the edge of the plasma. Additionally, CXRS loses time intervals with this method, because the beam is switched off for a time period.

The second method is fitting Gaussian curves to the passive and the active emission. This allows a continuous measurement, but on the other hand the analysis of the spectrum is more difficult, because an accurate knowledge of the passive and the background emission is required (including possible line emission from impurities). Additionally, the magnetic field will cause a Zeeman splitting of the energy levels. At a magnetic field of 2 T the Zeeman splitting of the carbon $n : 8 \rightarrow 7$ transition causes a broadening of about $7 \cdot 10^{-2}$ nm, which corresponds to a Doppler broadening according to a temperature of 90 eV [9]. Further, contributions for the CXRS signal exist due to the fine structure of the energy levels and the temperature dependence of the recombination cross-section. All these effects result in a complex spectrum of CXRS.

ASDEX Upgrade has two CXRS diagnostics CER and CHR for two different neutral

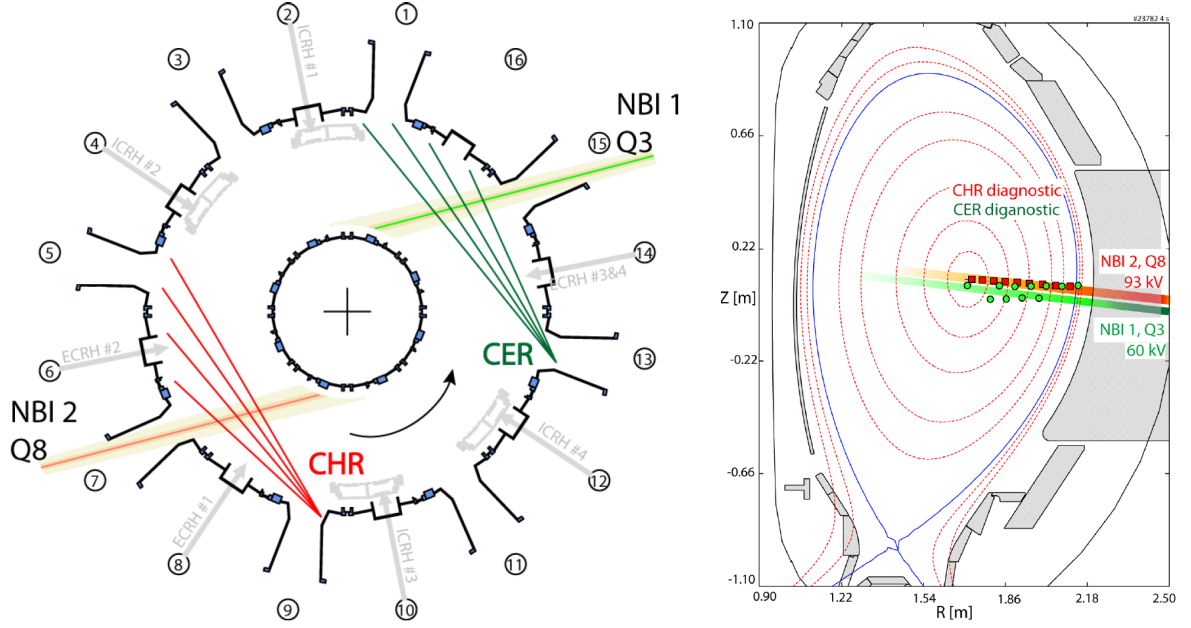


Figure 3.3: The two CXRS diagnostics in ASDEX Upgrade: CHR in red and CER in green. The figure on the left shows the toroidal cross section. The figure on the right shows a poloidal view of the configuration. [13]

beams, which are shown in Figure 3.3. CER is oriented onto the neutral beam Q3. It has a temporal resolution of 25 ms and 30 lines of sight (LOS), where up to 25 different radial positions can be imaged simultaneously. However, currently only about 11 to 15 channels yield reasonable spectra, which can be evaluated in order to get reliable velocity profiles in CER. CHR looks at the neutral beam Q8. CHR has a total of 9 active channels and a time resolution of 50 ms. These two diagnostics can monitor the plasma velocity during the operation time of the corresponding NBI source.

3.3. Electron Cyclotron Emission

Electron cyclotron emission (ECE) is a fast diagnostic for the determination of the local electron temperature in the tokamak. Therefore, it is suited for the investigation of fast plasma activities, like MHD modes.

An electron gyrates around the magnetic field line with the electron cyclotron frequency $\omega_c = \frac{eB}{m_e}$. Due to this accelerated motion the electron emits electromagnetic radiation with the corresponding frequency and its natural harmonics. At the electron cyclotron frequency the plasma is optically thick. Thus, it will absorb and emit radiation as a black

body, which is correlated to the electron temperature. The intensity of the emission can be described with Planck's law. The wavelength of the radiation is within the microwave range, thus: $h\nu < 1 \text{ meV}$. This is small in comparison with the electron temperature of: $T_e \sim 1 \text{ keV}$. In this case, Planck's law can be approximated by the Rayleigh-Jean's law, where the intensity is proportional to the electron temperature:

$$I = \frac{\omega^2}{4\pi^2 c^3} kT_e \quad (3.2)$$

The emission frequency depends on the magnetic field B , which is dominated by the toroidal magnetic field B_ϕ . Due to the tokamak geometry the toroidal magnetic field depends strongly on the major radius as: $B_\phi \propto 1/R$. Thus, measuring an intensity of a certain wavelength, will give the local electron temperature at the corresponding major radius R .

The cyclotron emission occurs with two possible polarisations, the so-called *O-mode* ($\mathbf{E} \parallel \mathbf{B}$) and the *X-mode* ($\mathbf{E} \perp \mathbf{B}$). The X-mode carries the most emission energy [10]. The first harmonic frequency of the X-mode is reflected inside the plasma and cannot leave it. Thus, only the second harmonic of the X-mode or the fundamental frequency of the O-mode can be used for the ECE diagnostic [10]. The usage of microwave detectors with a high time resolution allows the measurement of fast local temperature fluctuations.

ASDEX Upgrade has several ECE measurement systems. In this thesis the ECE diagnostic, which is called CEC, was used for the investigation of MHD mode rotation. CEC is a 60-channel superheterodyne radiometer for the measurement of the second harmonic X-mode along a horizontal (radial) line of sight (LOS) near the tokamak midplane. It has a temporal resolution of 31.25 kHz and a radial spatial resolution of about 1 cm [45].

3.4. Magnetic Measurements

The change of a magnetic field induces a voltage U_{coil} in a magnetic coil, which can be calculated according to Faraday's law as:

$$U_{coil} = -NA \frac{dB}{dt} \quad (3.3)$$

where N is the number of windings of the coil and A is the surface area defined by the coil. If the absolute value of the magnetic fields are of interest the signal has to

be integrated. This can be done directly with an analogue integrating circuit or with a numerical integration of the raw data. In ASDEX Upgrade such magnetic coils are used to determine the vertical and horizontal plasma position, its shape and the stored energy. Additionally, these measurements are used to obtain a plasma equilibrium EQH or FPP².

The investigation of magnetic perturbations due to MHD activities is even simpler, since no integration is necessary. The typical rotation frequency of an MHD mode in the lab frame is in the order of kHz. Because magnetic coils detect the time derivatives, even small perturbations, which are only $10^{-4} - 10^{-3}$ of the total magnetic field, can be seen. The rotation frequency of an MHD mode can be determined by an FFT analysis. Furthermore, different poloidal and toroidal arrangement of coils can be used to study the structure of MHD modes. The phase shift between coils at different locations will give information about the mode numbers.

In this thesis we use the so called Mirnov diagnostic to determine the frequency and structure of the mode. The Mirnov diagnostic in ASDEX Upgrade consist of a poloidal array of 32 coils and two toroidal arrays with 5 coils each, on the HFS and LFS of the tokamak. The Mirnov diagnostic has a sampling rate of 2 MHz. Figure 3.4 illustrates the Mirnov diagnostic in ASDEX Upgrade.

It should be mentioned, that Mirnov coils can distinguish MHD modes with two different frequencies quite well. However, if coupled MHD modes are present in a plasma, they rotate with the same frequency and the signals of the modes are superimposed. The distinction of the MHD modes has a large uncertainty, since the observed amplitude of each mode decreases with increasing distance and increasing m . Due to this fact usually only the external mode can be identified.

3.5. Soft X-Ray Diagnostic

Another important diagnostic for MHD mode characterisation are the soft X-ray (SXR) cameras. Soft X-ray emission originates from the high temperature regions in the plasma, due to the bremsstrahlung, bound-bound line emissions and free-bound recombination of heavy impurities.

²In order to find the equilibrium in ASDEX Upgrade, EQH uses the numerical equilibrium code CLISTE, which solves the Grad-Shafranov equation for the poloidal flux, for a set of poloidal coil currents and limiting structures. Additional information from other diagnostics, e.g. SXR information, can be included. FPP compares the magnetic signals with an available database for accurately determined equilibria. A detailed description of the equilibria reconstruction can be found in [38] and [27].

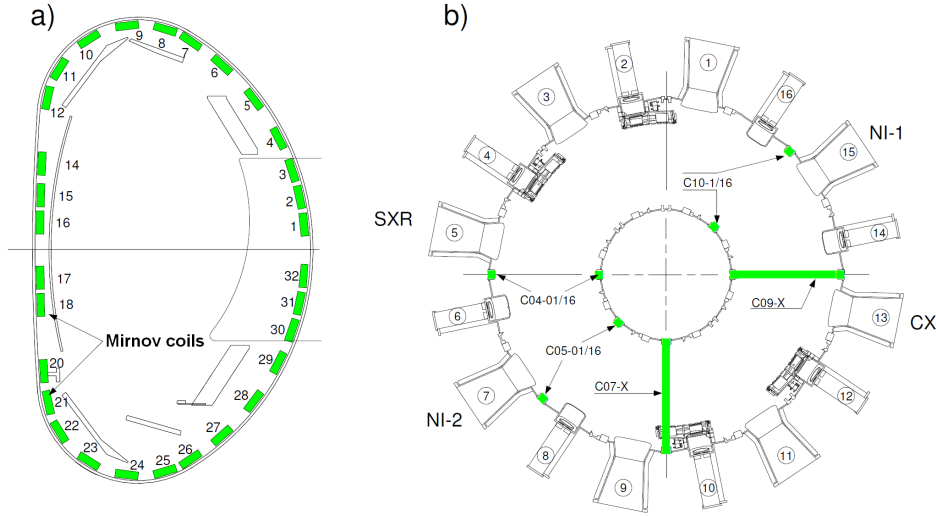


Figure 3.4: Mirnov diagnostic in ASDEX Upgrade. **(a)** Mirnov coils for the determination of the poloidal mode number m . **(b)** Mirnov coils for the determination of the toroidal mode number n .

The intensity of the bremsstrahlung in soft X-ray emission can be estimated for a hydrogen plasma and a Maxwellian velocity distribution. The emission intensity per volume including the camera sensitivity f_{camera} is proportional to [22]:

$$\varepsilon \propto \int n_e^2 Z_{eff} \cdot g_{ff}(T_e, E) \cdot \frac{\exp(-E/T_e)}{\sqrt{T_e}} \cdot f_{camera} \cdot dE \quad (3.4)$$

where n_e is the electron density, T_e the electron temperature, $Z_{eff} = \sum_i n_i Z_i^2 / n_e$ the effective ion charge and g_{ff} the so called Gaunt factor, which is in the order of unity. The observed intensity of SXR is the integral of the intensity per volume along the lines of sight.

SXR is well suited to monitor fast temperature and density fluctuations. This can be used for the investigation of various MHD modes. Unlike the Mirnov diagnostic SXR gives information on localisation and internal structure of MHD modes (e.g. mode coupling).

Furthermore, it has to be considered that heavy impurities can emit line radiation in the corresponding energy region and therefore contribute to the measured intensity. Heavy impurities in ASDEX Upgrade appear in particular in the form of tungsten, which

is not fully ionized even in the plasma core. In addition, the appearance of tungsten can cause a decrease of the electron temperature due to strong line radiation. This interaction of electron temperature and tungsten concentration has to be considered, when SXR data is analysed.

The SXR diagnostic in ASDEX Upgrade consists of 7 cameras at one toroidal position but different poloidal positions and one additional camera in a different toroidal position. They are oriented in such way, that they cover different poloidal angles in one poloidal plane (i.e. the toroidal component can be neglected). In total, these cameras create a dense grid of about 200 lines of sight (Figure 3.5). The sampling frequency of 2 MHz allow the investigation of fast MHD mode activity in ASDEX Upgrade.

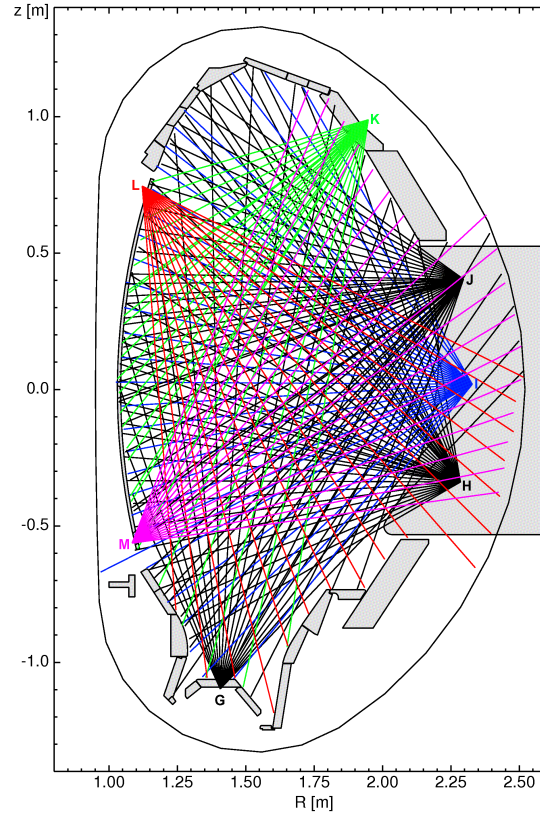


Figure 3.5: Poloidal view of Soft X-Ray lines of sight in ASDEX Upgrade

3.6. Integrated Data Analysis

A major challenge in fusion physics is the coherent combination of measurements from various diagnostics in order to get consistent information about the plasma. The Integrated Data Analysis (IDA) offers a unified and powerful tool for this task. Probabilistic forward modelling methods are used in IDA to merge the raw data of the diagnostics instead of combining results, which might rely on cumbersome iterative procedures [12]. In IDA, all information is formulated as probability density functions, using Bayesian probability theory. This allows the uniform determination of plasma parameters and their uncertainties [11].

The first application of IDA in ASDEX Upgrade was the determination of electron temperature and density profiles. There the information is combined from ECE, Thomson scattering (TS), Lithium Beam (LIB) and DCN-interferometry³. Usual IDA profiles are available with the temporal resolution of the EQH equilibrium, which is 1 ms. These profiles are used in this thesis for the calculation of diamagnetic electron velocity.

³A detailed description of the mentioned diagnostics can be found in [20] and [34]

Chapter 4.

Methodological Approach

In order to investigate MHD mode rotation and the effects of the ambient plasma the knowledge of mode characteristics is required. The first section of this chapter describes the approach for the characterisation of MHD modes. The second section describes shortly the determination of plasma rotation frequency. Finally this chapter continue with the electron diamagnetic drift frequency, which can contribute to the difference between the island and the ambient plasma rotation.

4.1. MHD Mode Characterisation

The appearance of MHD modes in ASDEX Upgrade can be detected in several ways. On the one hand MHD modes lead to a perturbed magnetic field (see equation 2.22), which can be detected with the Mirnov coil diagnostic. On the other hand, the appearance of MHD modes has an impact on the plasma temperature. In particular, magnetic islands act as short-circuit for transport, as it was mentioned in section 2.4. The radial temperature profiles are flattened in the O-point of the island, while the X-point still has a temperature gradient (see Figure 4.1). Therefore, island rotation causes temperature oscillations for a fixed location and enables island characterisation by temperature sensitive diagnostics like ECE or SXR.

4.1.1. Determination of MHD Mode Frequency

The rotation of an MHD mode is seen as a fast signal oscillation, in ECE, SXR or Mirnov coils. The fast Fourier transformation (FFT) analysis is used to determine the MHD mode rotation frequency.

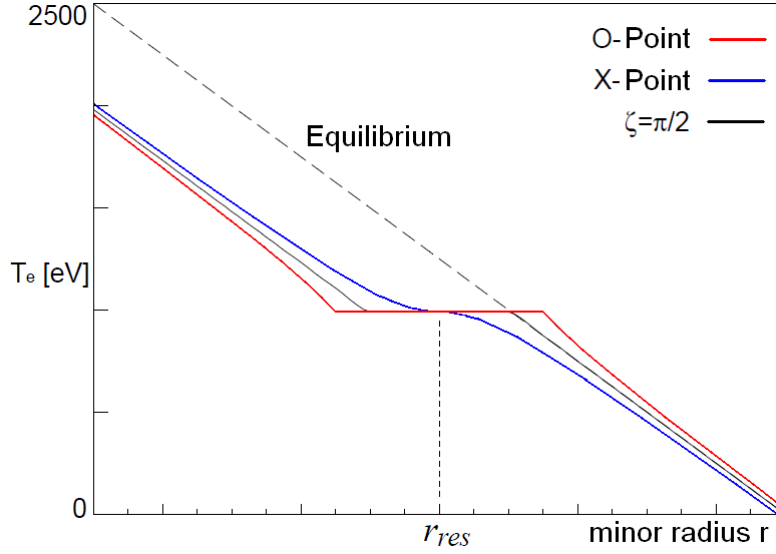


Figure 4.1: A theoretical profile of the electron temperature in the presence of a magnetic island [31].

The application of the FFT for various time steps will generate a spectrogram for the analysis of the mode frequency, which is exemplary shown in Figure 4.2 for discharge #25698. MHD modes are seen as strong FFT amplitudes, which are represented in blue. The tracking of a blue line will give the development of the MHD mode frequency. As can be seen in the spectrogram, a mode appears at 0.85s with 20 kHz and spins up to 24 kHz at 1.0s. At this time, the electron heating (ECRH) is turned on and the MHD mode decelerates to 13 kHz at 1.5s, where it stays almost constant until 2.0s. The following spin up and spin down of the MHD mode is caused by a modulated neutral beam operation of the NBI sources Q6 (more tangential) and Q8 (more radial). At 3.6s the MHD mode disappears. At that time, the ECRH heating is switched off and a rapid increase of tungsten concentration is observed in the core leading to strong line radiation. The increased radiation reduces strongly the electron temperature in the plasma core. Probably due to this dramatic change the island structure is destroyed. Another MHD mode appears at 3.8s for a short moment.

The frequency tracking in the spectrogram is well suited for the determination of MHD mode rotation frequency. However, it must be assured that the Nyquist frequency¹ of the diagnostic is higher than the determined frequency. Otherwise, the MHD mode rotation frequency cannot be reconstructed correctly from the signal.

¹The Nyquist frequency is defined as the half sampling frequency of a discrete signal.

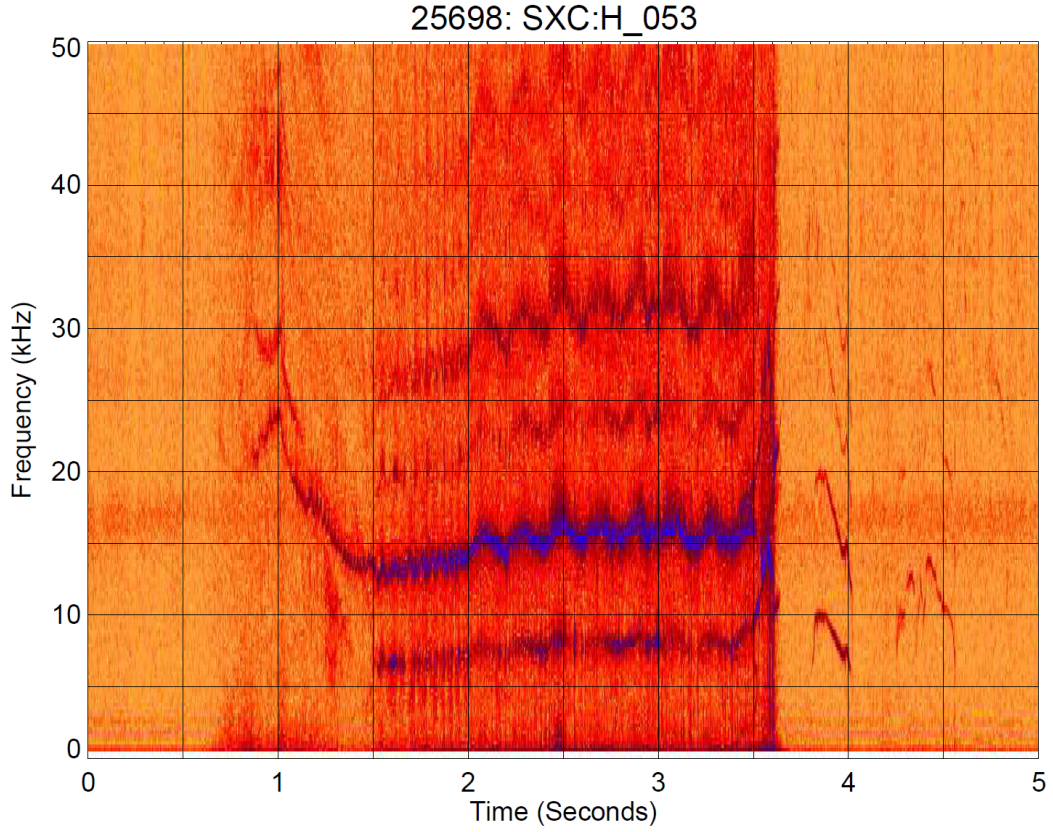


Figure 4.2: The spectrogram of the central SXR channel indicates clear MHD mode activity during the discharge #25698. The strong FFT amplitudes, which are represented in blue, show the presence of a strong MHD mode (and its harmonics).

4.1.2. MHD Mode Numbers

The determination of the MHD mode structure is important in order to interpret the measured signals from the diagnostics. The helical structure of an MHD mode can be described with the toroidal mode number n and the poloidal mode number m . These numbers describe the mode symmetry in the poloidal or the toroidal cross section, i.e. an island with $m = 2$ has two O-points and two X-points in a poloidal cross section.

Mode numbers can be identified in ASDEX Upgrade using an array of Mirnov coils. The raw signal is filtered with an FFT bandpass filter for the corresponding MHD mode frequency. In the next step the phase of the filtered signal is compared for adjacent coils. The calculation of the total phase offset gives the mode number: m for a poloidally and n for a toroidally distributed array (see Figure 4.3).

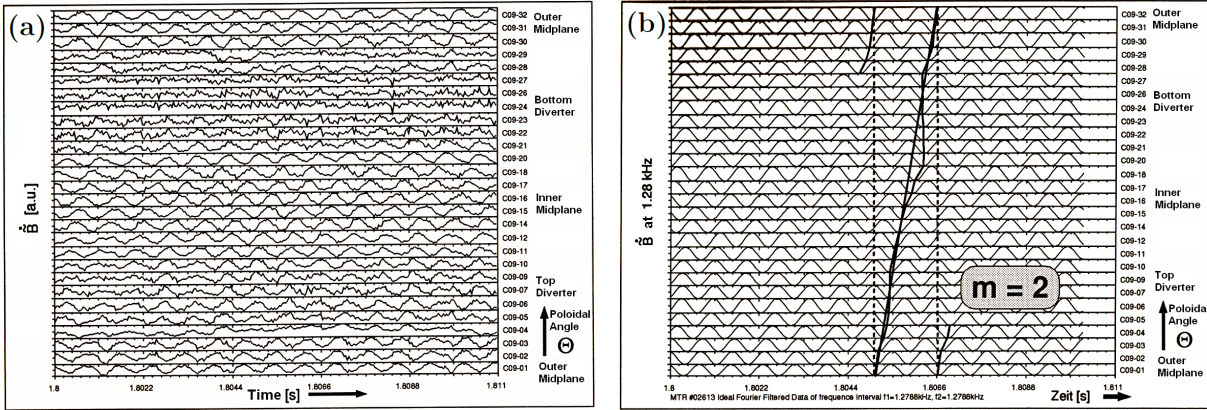


Figure 4.3: (a) Raw signal of poloidal Mirnov coils. (b) The filtered signal of the mode frequency after the band pass filter. The total phase offset determines the poloidal mode number m [37].

4.1.3. MHD Mode Localisation

After the determination of the helical structure also the localisation of the MHD mode is necessary in order to enable the comparison with the ambient plasma rotation. An easy method to obtain the mode position is using the equilibrium reconstruction, since the mode numbers m and n define the resonant flux surface of the MHD mode. However, the uncertainty of the q -profile from the equilibrium reconstruction is rather high in ASDEX Upgrade. Thus, additional methods for the localisation have to be applied.

One possible method for the determination of the position of magnetic islands with ECE. The method can be easily understood, if we look at the temperature profiles of the island. It is useful to start from the temperature profile of the X-point, which is shown in Figure 4.1. If the island rotates, the X-point profile will go over to an O-point profile. Thus, the measured temperature will decrease for the ECE channels on the inner side of the resonant surface and increase outside. The temperature will oscillate antipodal for the channels inside and outside the X-point. This enables the determination of the resonant surface location by comparing the signal of the ECE channels or more easily by the determination of the phase jump of one π in the FFT analysis. However, this method works only if the ECE signal is good (no cut-off) and the region of the phase jump is covered sufficiently by ECE channels. It has to be mentioned, that due to the displacement eigenfunction ECE has no phase jumps for ideal kink modes [21] and for the resistive layer in the $m = 1$ case [3].

Additionally, the SXR diagnostic can be used as a supplementary tool for the mode position, even though the determination of the position with SXR is not as precise as with ECE. SXR has a smaller spatial resolution and uses line integrated signals. But in contrast to ECE, SXR has a higher time resolution and monitors the whole plasma. In particular, SXR is well suited to detect the $q = 1$ surface in the presence of sawtooth crashes. These crashes cause a rapid temperature decrease inside the $q = 1$ surface and increases the temperature outside. The $q = 1$ surface can then be identified as the position between the last decreasing and first increasing line of sight in SXR.

The location of MHD modes in ASDEX Upgrade is described either by the minor radius or more conveniently by the normalised poloidal flux coordinate ρ_{pol} , which can be used to compare different plasma sizes and shapes. ρ_{pol} is defined using the poloidal flux, which was introduced in equation 2.14:

$$\rho_{pol} = \sqrt{\frac{\Psi - \Psi_{core}}{\Psi_{separatrix} - \Psi_{core}}} \quad (4.1)$$

The conversion between ρ_{pol} , minor radius or a certain space coordinate in ASDEX Upgrade is carried out with the help of the equilibrium diagnostic *EQH* or *FPP*.

4.1.4. MHD Mode Coupling

It is possible that several modes exist simultaneously in the plasma. In some cases MHD modes can couple and rotate with the same frequency. If individual MHD modes generate perturbed electric currents, an interaction force will occur amongst them. The analogue picture is the attraction force of two conducting wires with the same current direction. The linear theory provides that MHD mode coupling on different flux surfaces takes place, if the modes have an toroidal mode number n . It is assumed that the coupling occurs in phase where the force interaction region has its maximum. This happens where the spatial distance is minimum, which is on the LFS [43].

MHD Mode coupling can be investigated with the SXR diagnostic. The expected signal for the amplitude and phase profiles in the FFT analysis of SXR can be obtained for individual and coupled modes from simulations (see Figure 4.4). It can be recognized that individual MHD modes generate a characteristic signal shape, which can be used to interpret the mode characteristics. For example, if there is only one mode in the plasma, the number of minima in the amplitude is equal to the number of phase jumps and will yield the mode number m . In particular, the amplitude will have a central minimum for

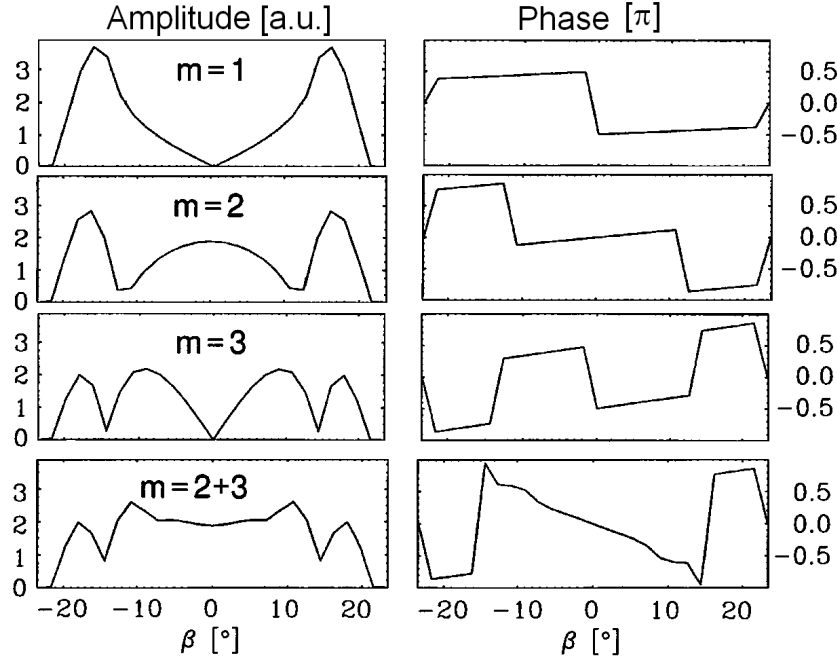


Figure 4.4: Modulated SXR diagnostic for cylindrically shaped plasma and a SXR camera 1 m from the plasma axis. The angle β represents the orientation of the LOS. The individual MHD modes were simulated at the resonant radius of 0.3 m, while the coupled modes were located at the radius of 0.2 m for $m = 2$ and 0.3 m for $m = 3$ [43].

an odd m number. On the other hand, if MHD modes are coupled, the SXR amplitude is shaped rather complex and it is not trivial to characterise the existing modes. However, the SXR signal enables to distinguish rather clear, if there is only a single MHD mode or if there are several MHD modes present in the plasma.

4.2. Determination of Plasma Rotation Frequency

The plasma rotation is measured with the CXRS diagnostic, which was introduced in section 3.2. In order to get a velocity profile, a polynomial function is fitted to the CXRS data over ρ_{pol} as a least square fit, with the singular value decomposition function in IDL. The plasma rotation frequency f_{rot} can then be calculated as:

$$f_{rot} = \frac{v_{rot}}{2\pi R} \quad (4.2)$$

where R is the major radius of the measured position.

It should be considered, that CXRS measures the rotation of impurity ions like carbon or boron, while the plasma rotation is determined by the main ions. The difference of the velocity can be calculated with the neoclassical friction between the main ions and the impurities. The largest contribution for the deviation is given by the ion temperature gradient, but also the ion density is of relevance [24]. In ASDEX Upgrade the velocity of main plasma ions is usually slightly higher (in the order of $10 - 20 \frac{\text{km}}{\text{s}}$ [29]) compared to the impurities.

4.3. Electron Diamagnetic Drift

The electron diamagnetic drift velocity can be calculated with equation 2.27. In a tokamak the largest magnetic field is in the toroidal direction. Due to the cross product of \mathbf{B} with the radial pressure gradient the diamagnetic drift velocity will be mainly in the poloidal direction, which can be approximated calculated as:

$$v_{dia,e} = \frac{1}{en_e B^2} \cdot \left(n_e \frac{\partial T_e}{\partial r} + T_e \frac{\partial n_e}{\partial r} \right) \cdot B_\phi \quad (4.3)$$

where T_e and n_e represent the electron temperature and density profiles. Consistent electron profiles were obtained from IDA. In order to consider the island widths, the gradient was determined averaged over the spatial range of a typical island width in ASDEX Upgrade ($5 - 8 \text{ cm}$ or $\Delta\rho_{pol} \approx 0.1$) as:

$$\frac{\Delta T_e}{\Delta\rho_{pol}} \approx \frac{T_e(\rho_{pol,res} - 0.05) - T_e(\rho_{pol,res} + 0.05)}{\Delta\rho_{pol}} \quad (4.4)$$

and accordingly for the electron density. The required radial gradient is determined afterwards with the corresponding radial positions using the equilibrium reconstruction. The electron diamagnetic drift frequency is determined every 1 ms (standard IDA time resolution) and time-averaged over the time intervals of the CXRS diagnostic, in order to compare equal time steps.

4.3.1. Consideration of Geometrical Properties

The plasma equilibrium in ASDEX Upgrade is usually elongated in the poloidal cross section. As can be recognized from Figure 4.5 the radial gradients vary for different poloidal angles Θ , since the poloidal geometry of the plasma is not exactly circular. In order to consider this in the calculation, the radial gradients for the electron temperature were calculated for different angles as:

$$\frac{\partial T_e}{\partial r} = \frac{\Delta T_e}{\Delta \rho_{pol}} \cdot \frac{\Delta \rho_{pol}}{\Delta r(\Theta)} \cdot \sin(\alpha)$$

Here, $\frac{\Delta \rho_{pol}}{\Delta r(\Theta)}$ considers the elongated equilibrium shape for a given poloidal angle Θ . The parameter $\sin(\alpha)$ considers the fact, that the radial LOS from the magnetic axis is not exactly perpendicular on the equilibrium flux surface for every Θ (α is the angle between the radial LOS and the equilibrium flux surface). The analogue calculation is carried out for the electron density gradient. Afterwards, the local diamagnetic drift velocity $v_{dia,e}$ is calculated with equation 4.3 at the island position $\rho_{pol,res}$ and different angles Θ . This is used to calculate the necessary time for a full rotation $T_{dia,e}$. The reciprocal value of the required time gives the electron diamagnetic drift frequency:

$$\frac{1}{f_{dia,e}} = T_{dia,e} = \int_0^{2\pi} \frac{r(\Theta)}{v_{dia,e}(\Theta)} \cdot d\Theta \quad (4.5)$$

where $r(\Theta)$ is the corresponding minor radius from the magnetic axis.

The resulting geometrical correction is smallest close to the magnetic axis, where the flux surface is most circular. For increasing ρ_{pol} - values the correction increases considerably. The electron diamagnetic drift $v_{dia,e}$ and the minor radius r are shown in Figure 4.6 for the resonant surface at $\rho_{pol} = 0.51$. In this case, the resulting diamagnetic drift frequency from equation 4.5 is 1.27 kHz. The simple calculation of the electron diamag-

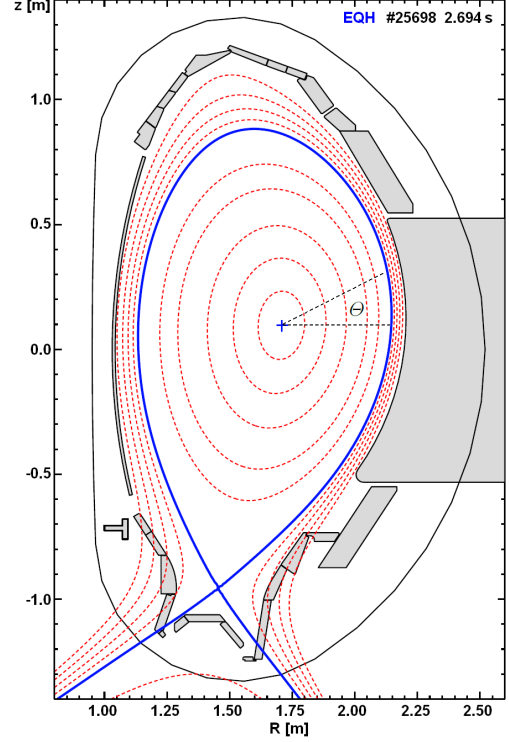


Figure 4.5: Poloidal view of the EQH equilibrium. Red dashed lines show constant ρ_{pol} - values and the blue line illustrates the separatrix.

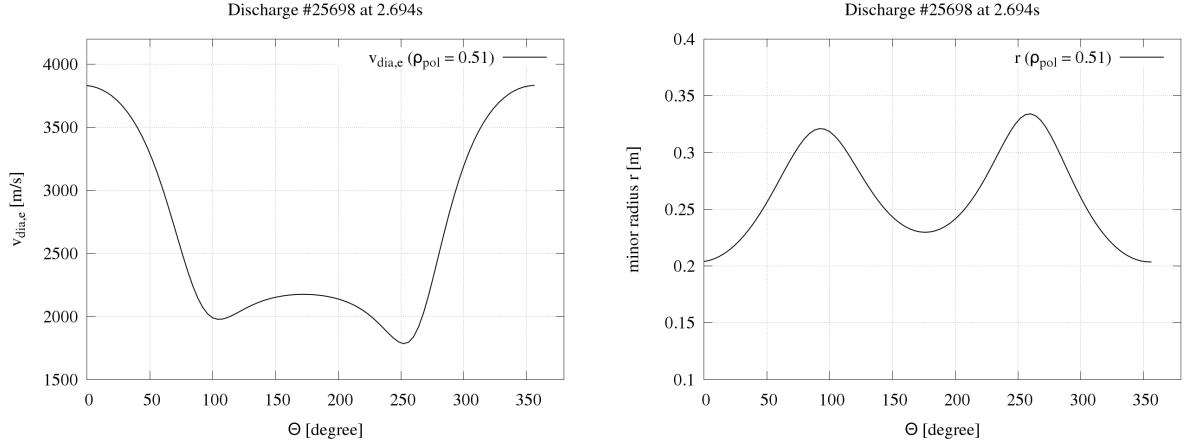


Figure 4.6: Geometrical effects for the calculation of $f_{dia,e}$ for discharge #25698 and 2.694 s at the resonant surface $\rho_{pol} = 0.51$. Due to the large radial gradient the diamagnetic drift velocity is maximum at the LFS. Additionally, the minor radius is minimum for this position.

netic drift frequency $f_{dia,e} = \frac{v_{dia,e}}{2\pi r}$ on the LFS gives 2.98 kHz. This demonstrates the importance of geometrical effects in an elongated plasma cross section.

When the angular velocity $\omega_{dia,e}$ is calculated and transferred to the straight field line angle Θ^* , the resulting rotation velocity will be constant, as it is expected. However, the method of determining the electron diamagnetic drift frequency in straight field line coordinates requires a monotonic q -profile to calculate Θ^* all over the plasma². This is not always the case for the EQH equilibrium. In order to use consistent equilibria with IDA, which is based on EQH, we used the described method to determine the electron diamagnetic drift frequency.

²The calculation of Θ^* can be carried out with the routine by W. Schneider in the kk-package in ASDEX Upgrade.

Chapter 5.

MHD Modes and Plasma Rotation

The introduced theory and tools provide us a basic framework in order to describe the MHD mode rotation. It is expected from the standard theory that the observed island rotation is determined by the ambient plasma rotation and the electron diamagnetic drift frequency at the resonant surfaces, which is described by equation 2.28.

5.1. The Rotation of (3/2) Modes

The MHD mode rotation frequency is determined with SXR as described in section 4.1.1 and the plasma rotation frequency is determined as shown in section 4.2. A comparison of the plasma rotation and an observed MHD mode is shown in Figure 5.1 for discharge #25698 and a selection of discharge parameters is shown in Figure 5.2. The MHD mode occurs at 0.85 s and 20 kHz without any trigger indication. The mode analysis (see section 4.1) characterises this MHD mode with $m = 3$ and $n = 2$. In addition we can observe a phase jump in the FFT analysis of the ECE, which is expected for an island due to its eigenfunction [31]. Hence, the MHD mode is assumed to be a (3/2) magnetic island.

The determination of the island location in the early growth phase is not possible, due to a noisy ECE signal. It can be determined firstly around 0.92 s at rather central ρ_{pol} -values of about 0.34. This corresponds to the plasma rotation at the similar location, without any contribution by the electron diamagnetic drift velocity. Afterwards the island position shifts further outside in ρ_{pol} and for ECE channel numbers. This confirms a real radial shift. The island location levels off at $\rho_{pol} \approx 0.51$ after 1.75 s. The time scale of the shift is several 100 ms, which is in the order of the current diffusion time. This indicates that the current profile and the q -profile can change considerably, when the mode occurs.

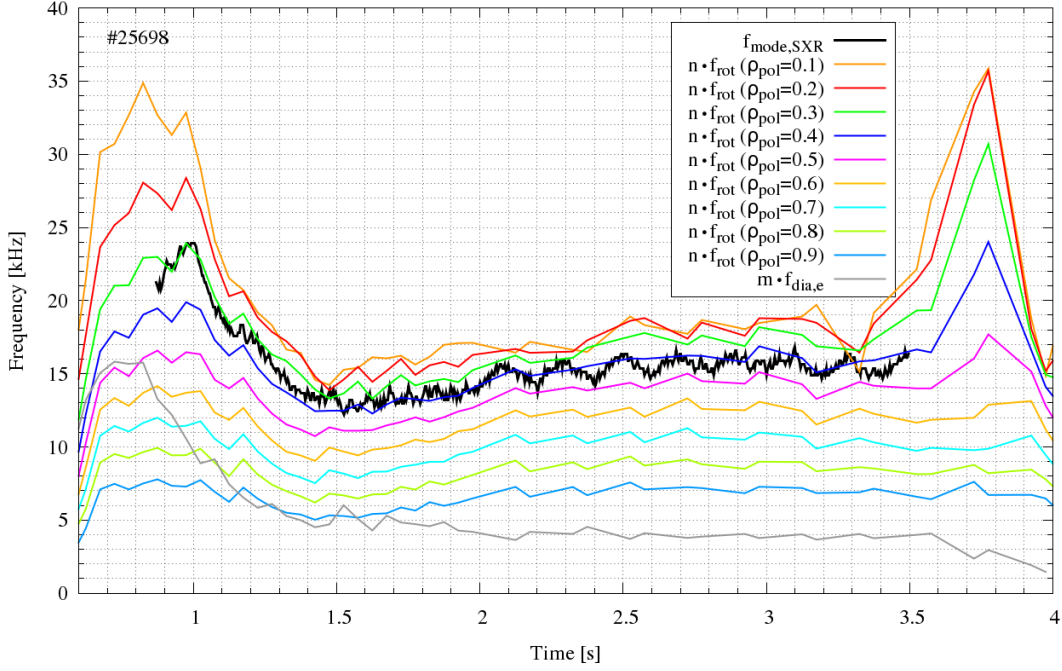


Figure 5.1: The comparison of n times the plasma rotation frequency and the observed (3/2) island during discharge #25698. Additionally, m times the electron diamagnetic drift frequency is shown in gray. Discharge #25698 is an H-mode with 800 MA flat top current, a line averaged central electron density of around $5.2 \cdot 10^{19} \frac{1}{\text{m}^3}$ and a toroidal magnetic field of -2.48 T on axis.

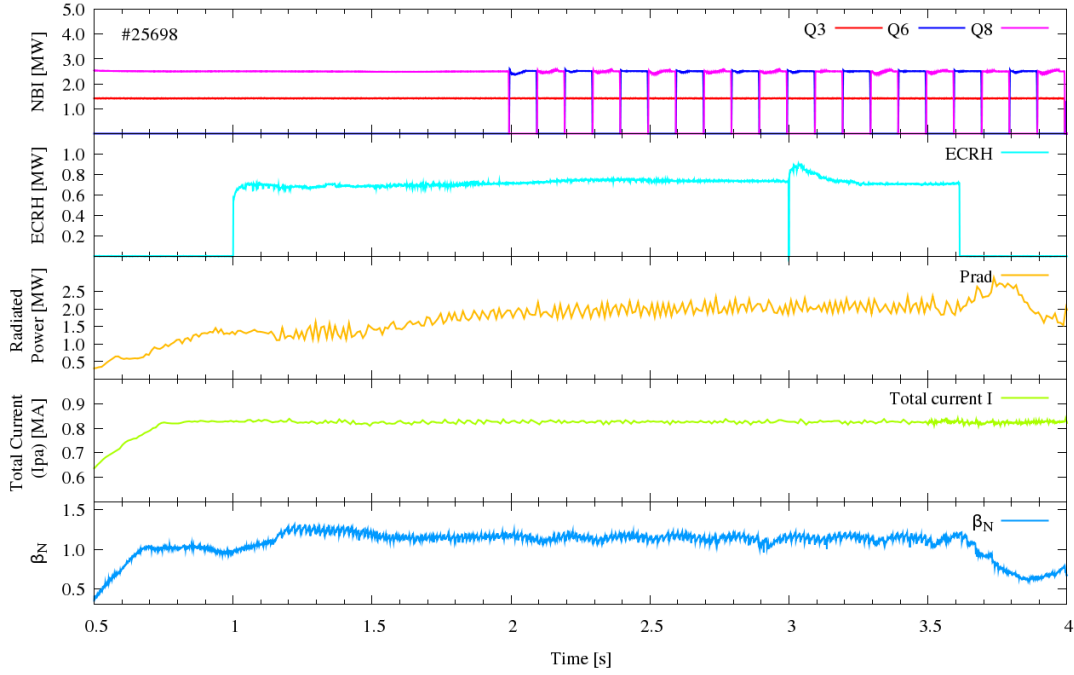


Figure 5.2: Overview of selected discharge parameters for #25698. The NBI sources $Q6$ and $Q8$ are operated alternating in 100 ms intervals from 2.0 s. An ECRH heating of about 0.7 MW starts at 1.0 s. At 3.0 s the ECRH heating is increased to 0.9 MW until 3.6 s. Afterwards, the ECRH is switched off.

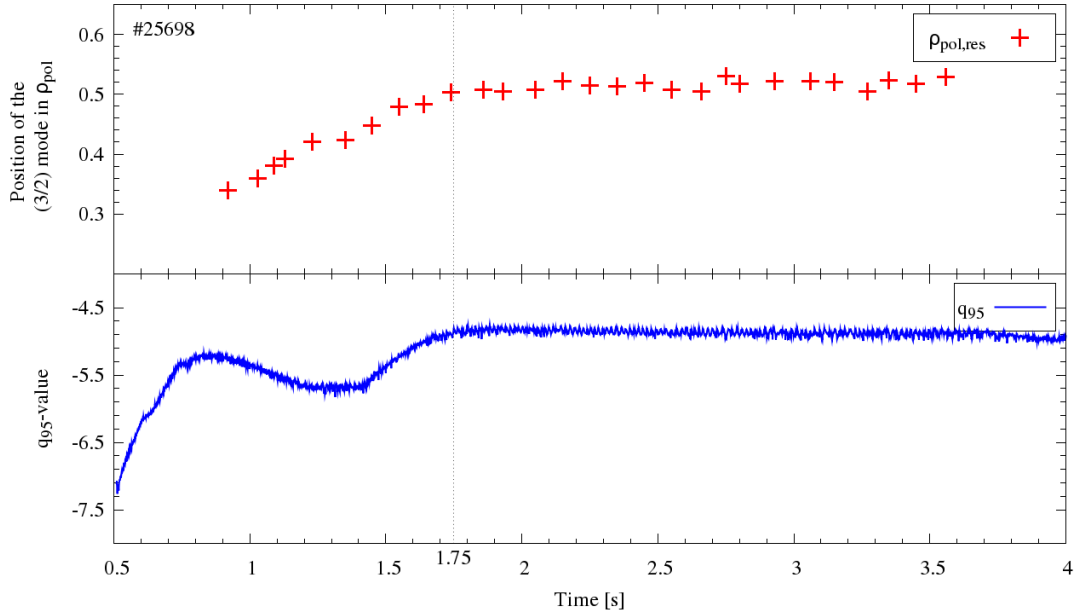


Figure 5.3: The top graph shows the development of the (3/2) island location and the q_{95} factor is shown in the lower graph.

A change can also be observed for the absolute q_{95} -value¹ (see Figure 5.3). It can be argued, that the mode location is fixed on the q -profile and a decrease of q_{95} can decrease the q -profile all over the plasma. Hence, the $q = 1.5$ location can shift further outside. However, this explanation would fit only between 1.4s and 1.75s, but an increasing ρ_{pol} is also observable before 1.4s, where the q_{95} does not decrease. Therefore, q_{95} is probably not the only reason for the shift of the MHD mode and there should be an additional mechanism.

One possible explanation for the shift could be the following: When the island occurs, the temperature and density profiles are flattened. This flattening will cause a reduction of the bootstrap current, reducing the local electric current density. This should slightly reduce the total electric current in the plasma. On the other hand, the control system of ASDEX Upgrade keeps the total electric current at a constant value. Therefore, the central OH-coil (see section 3.1) will induce additional electric current, which will diffuse in the core. Such an ohmic electric current profile could be more peaked. Hence, the central q -value could decrease and lead to a shift of the resonant surface with $q = 1.5$. However, we must be careful with this explanation. The percentage of the bootstrap current is rather small for the investigated ρ_{pol} in ASDEX Upgrade. Therefore, we would expect only a small effect on the q -value. A detailed investigation could provide more understanding of

¹ The q_{95} is defined as a boundary q -value at 95% of the poloidal flux Ψ .

the physical mechanisms for this observation, especially since the understanding for the development of island locations could be helpful for the active control of magnetic islands.

The temporal development of the island location was taken into account for the calculation of the electron diamagnetic drift frequency, which is also shown in Figure 5.1. The diamagnetic drift frequency is large when the mode appears and the island location is further inside. This is due to the high temperature gradient for the ρ_{pol} -values around 0.35. Further outside IDA shows a flattening of the temperature profile between $\rho_{pol} \approx 0.5 - 0.6$, hence diamagnetic contribution decreases when the island shifts into this region.

The comparison of the island rotation with the ambient plasma in Figure 5.1 indicates that the mode rotation corresponds with the plasma rotation at $\rho_{pol} \approx 0.35$ during the formation time. Afterwards, the mode speeds up and reaches the plasma rotation at $\rho_{pol} \approx 0.3$. It follows the rotation for some 100 ms and finally levels off with the plasma rotation frequency of around $\rho_{pol} \approx 0.4$. The mode frequency does not differ a lot from the plasma rotation at the $q = 1.5$ surface and the consideration of the uncertainty, which is described below, could be used in order to explain the mode frequency only with the plasma rotation. However, according to the theory, island rotation should also include the electron diamagnetic drift velocity, which has to be subtracted for the plasma in ASDEX Upgrade (see section 2.6). If this is done, the observed mode rotation will be clearly faster than the expected mode frequency. This will be discussed in the next section in more detail.

Two further (3/2) islands were present in discharges #25776 and #25825. Both islands show similar development of their position as for the mode in #25698 (see Figure 5.4). They begin slightly further inside in the plasma at around $\rho_{pol} \approx 0.42$ and level off after several 100 ms at $\rho_{pol} \approx 0.52$. However, the q_{95} is almost constant for both cases. This strengthens our assumption, that the q_{95} cannot explain the shift of the island location.

The rotation comparison for discharge #25776 is shown in Figure 5.5. The observed frequency of the (3/2) mode is systematically faster than that of the plasma rotation at the rational surface. In contrast to the mode during discharge #25698, the frequency difference of the mode and the plasma is often larger than 2 kHz, which indicates that the mode rotation cannot be described by the plasma rotation within the uncertainty. Furthermore, if the electron diamagnetic drift is considered, the difference for the observed and the expected mode frequency increases. This indicates again, that the (3/2) islands does not move in the electron diamagnetic direction in the plasma rest frame.

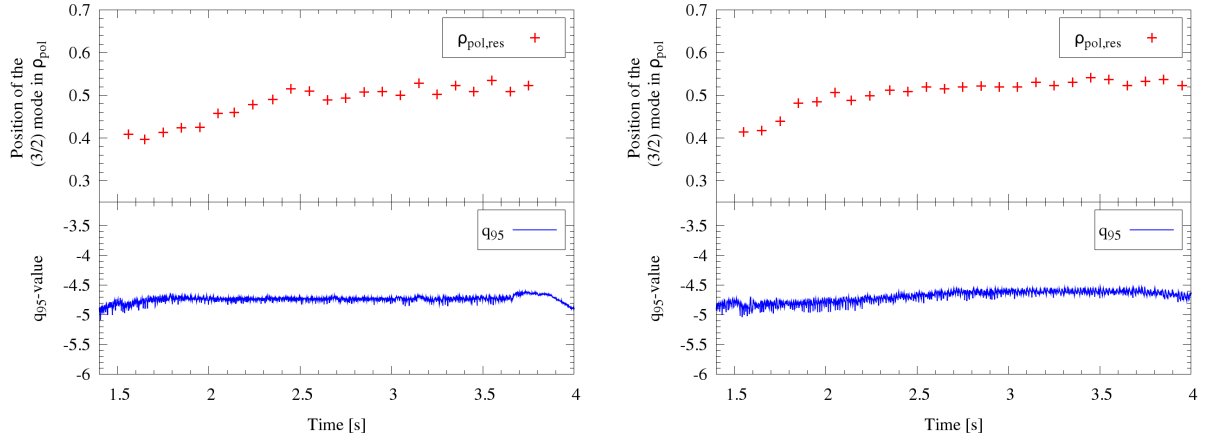


Figure 5.4: The development of the location of the (3/2) islands and the q_{95} value during discharges #25776 and #25825.

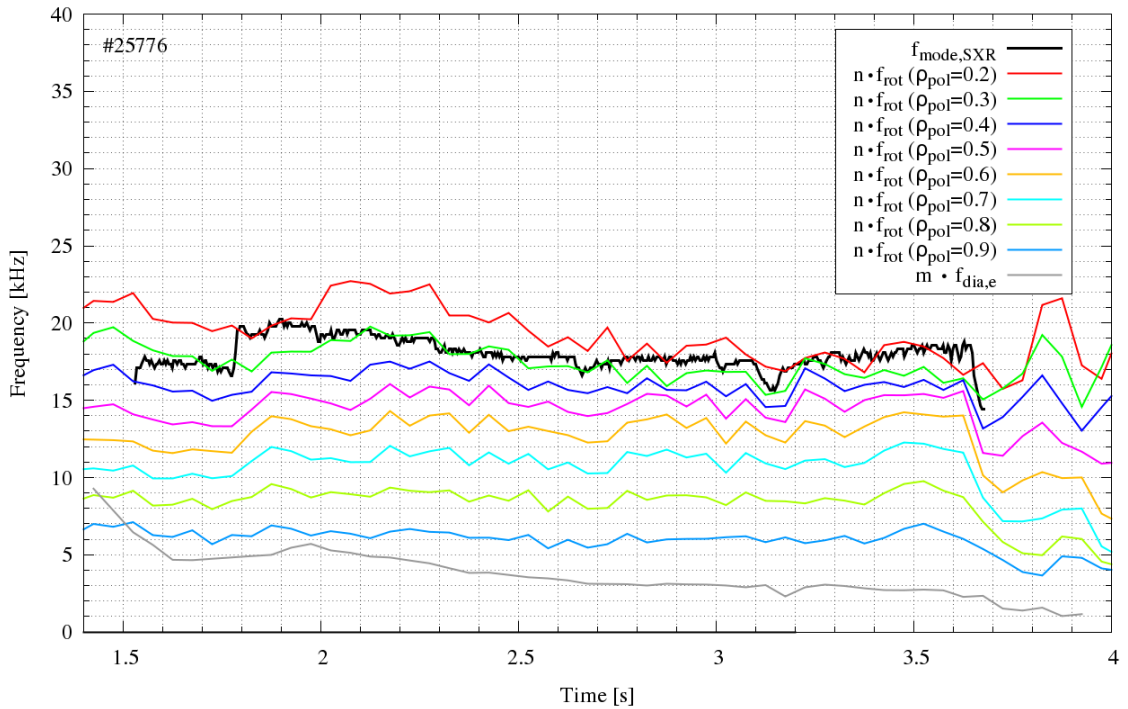


Figure 5.5: The rotation comparison for discharge #25776. This H-mode discharge has a flat top current of 1.0 MA, a central line averaged density of $7.7 \cdot 10^{19} \frac{1}{\text{m}^3}$ and a toroidal magnetic field of -2.52 T on axis. The NBI power input during the mode is constantly 7.7 MW. The ECRH heating works continuously during the mode occurrence but changes between 0.7 MW and 1.7 MW.

The comparison for discharge #25825 in Figure 5.6 demonstrates the same frequency discrepancy as it was observed for previous discharges. All these islands move faster than predicted by the plasma rotation and the electron diamagnetic drift. Actually, the (3/2) islands seems even to prefer the ion diamagnetic rotation direction in the plasma rest frame. Observations for magnetic islands, which are faster in comparison with the plasma rotation were previously found in ASDEX Upgrade [35] and in DIII-D [16].

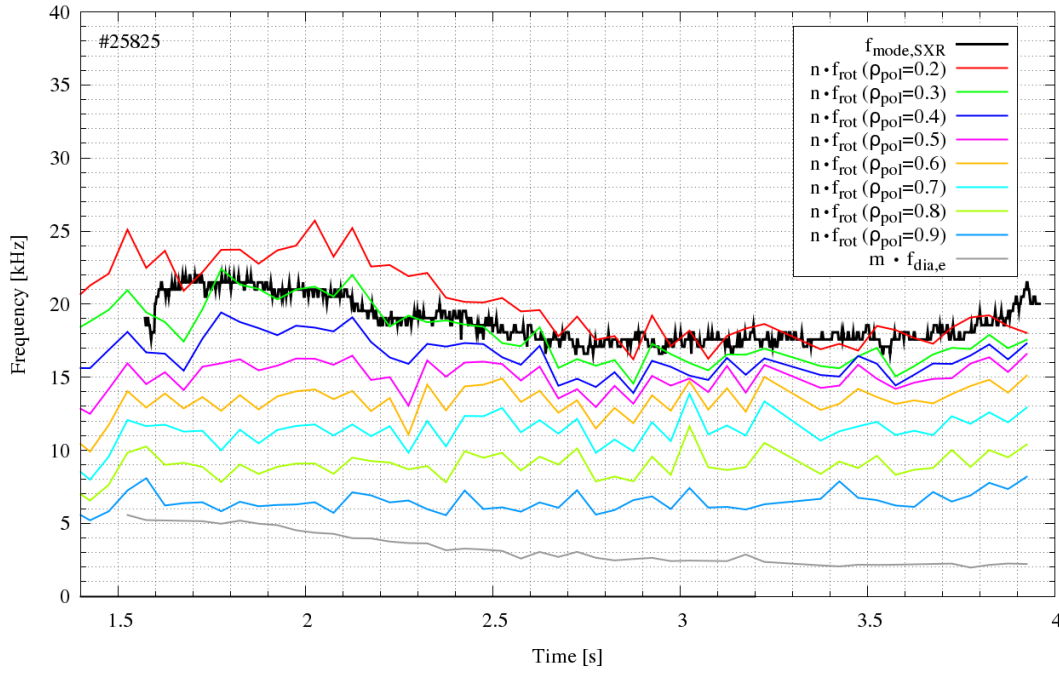


Figure 5.6: The rotation comparison during discharge #25825. This is an H-mode discharge with a flat top current of 1.0 MA, a central line averaged density of $8.2 \cdot 10^{19} \frac{1}{m^3}$ and an axis toroidal magnetic field of -2.48 T. The heating by NBI is 7.5 MW and no ECRH. Instead, the ICRH heating has a power input of 3.3 MW during the presence of the mode.

One possible explanation for this behavior was shown in the investigation by [18]. This work focuses on the influence by the so-called *Neoclassical Toroidal Viscosity theory* (NTV), which was introduced in section 2.7. This theory describes a neoclassical damping of the plasma flow and predicts an additional offset of the observed mode frequency. This offset is directed in the ion diamagnetic drift direction and depends mainly on the ion temperature gradient. If this offset is larger than the electron diamagnetic drift the island could rotate faster than the ambient plasma at its location, which would explain the observations. The investigation of these effects is carried out in the next chapter.

Another contribution, which has not been considered yet, could be the mode coupling. The motivation for this assumption can be seen during discharge #25698 in Figure 5.1. The decrease of the island rotation frequency from 1.0 s to 1.5 s is similar to that of the plasma rotation at $\rho_{pol} \approx 0.3$, while the relative deceleration of the plasma at the island location is smaller. This indicates that the (3/2) island is connected to inner ρ_{pol} -values, which could be possible if mode coupling occurs. The existence of sawtooth crashes indicates a $q = 1$ surface during discharge #25698. Thus, the (3/2) mode could couple with an internal (2/2) mode. The determination of the inversion radius in SXR identifies the $q = 1$ resonant surface location at $\rho_{pol} \approx 0.28$.

In order to investigate mode coupling, the SXR signal was analysed (see Figure 5.7). It can be seen that the central SXR amplitude of the mode frequency does not have a minimum, which is expected for an $m = 3$ mode (see section 3.5). Also the phase jumps do not show a characteristic $m = 3$ mode. Instead of that, the FFT transformation of the SXR diagnostic shows a clear amplitude for the central channels. This indicates an even m mode, which is closer to the plasma center than the (3/2) mode. Having $n = 2$ the coupled mode can only be a (2/2) mode. Additionally, all ECE channels, which are inside the $q = 1.5$ surface do not show an phase jump. Hence, the coupled MHD mode should be ideal. An ideal mode does not change the topology of the magnetic flux. Therefore, it should be able to move rather freely in the plasma. However, it is not fully understood if an ideal MHD mode couples without any drag effects, or if it can drag the (3/2) island, e.g. via the NTV.

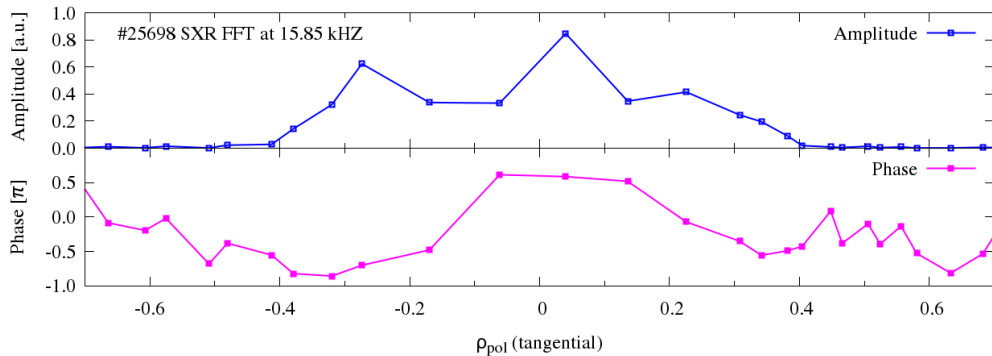


Figure 5.7: The FFT analysis with SXR for discharge #25698 and 15.85 kHz at 2.55 s indicate the existence of an $m = 2$ ideal MHD mode in the central plasma, which couples to the (3/2) island.

Estimation of the Uncertainties

An extensive calculation of the uncertainties is not carried out in this work, in particular due to the fact that not all uncertainties are available. However, a rough estimation of the uncertainty can be performed as the following:

The uncertainty of the FFT spectrogram from the SXR signal is 250 Hz per pixel, thus $\Delta 500$ Hz should be considered at least. Furthermore, the determination of the location is possible for the region between two adjacent ECE channels. This and the mapping routines for the equilibrium reconstruction should give an uncertainty of about $\Delta \rho_{pol} \approx 0.04$, which amounts to approximately $\Delta 0.5 - 1.0$ kHz (depending on the rotation profile).

The uncertainty for the plasma rotation from CXRS diagnostic has two contributing effects. Firstly, the CXRS measures the velocity of the carbon impurities and not of the main plasma ions, which are slightly faster (section 4.2). This gives a systematic error for the plasma rotation. In addition, the determination of the rotation velocity is performed by a fit of three Gaussian functions into not always clearly separated peaks in the measured spectrum, hence there might be a large fitting error. The specified uncertainty in the CXRS data is usually around 5 %, which would correspond to $\Delta f_{rot} \approx 1.0$ kHz. This uncertainty seems to be underestimated and the real uncertainty is probably higher.

The determination of the diamagnetic drift frequency requires temperature and density profiles, the toroidal magnetic field and the corresponding positions for the radial gradient. The magnetic field and the position values are taken from the equilibrium, which does not include uncertainty information. The electron temperature and density uncertainties can be obtained from IDA. Equation 4.3 can be used to show, that the uncertainty for the diamagnetic drift is linearly dependent on these quantities and their radial gradients. According to Gaussian uncertainty propagation, the velocity uncertainty is then given as:

$$\Delta v_{dia,e} = \sqrt{\left(\frac{\Delta T_e}{T_e}\right)^2 + \left(\frac{\Delta n_e}{n_e}\right)^2 + \left(\frac{\Delta \frac{\partial T_e}{\partial r}}{\frac{\partial T_e}{\partial r}}\right)^2 + \left(\frac{\Delta \frac{\partial n_e}{\partial r}}{\frac{\partial n_e}{\partial r}}\right)^2} \quad (5.1)$$

Due to the fact, that IDA data uses modeled profiles, the uncertainty of gradients can be assumed to be of the same order as the uncertainty of the profile. Equation 5.1 will result in an uncertainty of about 35% for diamagnetic drift if we assume for the temperature uncertainty 15% and for the density uncertainty 20%. This in turn will correspond to an uncertainty of $\Delta f_{dia,e} \approx 1.8$ kHz, if the diamagnetic drift frequency is 5 kHz.

The Influence of ECRH on Mode Rotation

An additional effect can be observed in Figure 5.1 at 1.0 s. Exactly at this time an additional ECRH heating of 0.7 MW is turned on and the rotation velocity of the island and that of the plasma decelerate approximately with the same rate. Furthermore, at 3.61 s the ECRH is turned off and the plasma rotation increases.

The decrease of the plasma rotation due to ECRH has been observed in several experiments [28], [9]. One possible explanation is the global confinement time of energy, which is strongly correlated to the momentum confinement [9]. Scaling laws show that the energy confinement time τ_E and the energy input P scales as $\tau_E \propto P^{-\alpha}$, with $\alpha = 0.5 - 0.73$ [32]. Since ECRH provide heating power but no momentum input, it can be stated that the plasma rotation decreases with ECRH. In addition, the local change of the momentum transport can contribute to the decrease of the plasma rotation [9]. However, the underlying physics are still not fully understood [28]. The island rotation in Figure 5.1 decelerates parallel in comparison with the plasma rotation. The difference between plasma and mode rotation does not change. Hence, the ECRH influences mainly the ambient plasma rotation but not the rotation of the (3/2) island in the plasma rest frame.

5.2. The Rotation of (2/1) Modes with Flat Temperature Profiles

The previously shown modes occur in plasmas without strong impurity contribution, which means in particular, that the central plasma temperature is around several keV with a clearly distinctive temperature profile. But it can happen in ASDEX Upgrade, that the plasma becomes contaminated by tungsten. Because of its large nucleus charge, tungsten is not fully ionized in the plasma. The remaining tungsten electrons can be excited and will emit line-emission during relaxation, resulting in an additional energy loss. Tungsten can accumulate in the plasma core and causes there a temperature reduction.

It has been observed in ASDEX Upgrade that (2/1) islands can occur in cases with tungsten accumulation and flat temperature profiles in the plasma core. These cases are of interest for the understanding of mode rotation, since the diamagnetic effects should be strongly reduced. Therefore, these islands are expected to rotate almost as the plasma at the corresponding location. The comparison of the rotation of such (2/1) islands is shown in Figure 5.8 and Figure 5.11.

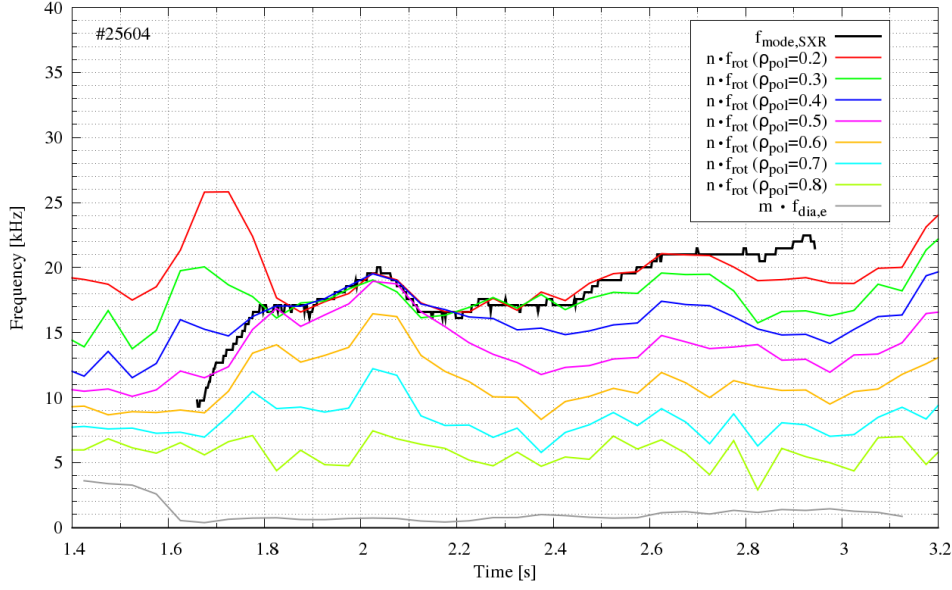


Figure 5.8: The comparison of rotation frequencies in discharge #25604. The (2/1) island arise at 1.661 s without a trigger indication. At the same time a flattening of the rotation profile is observed.

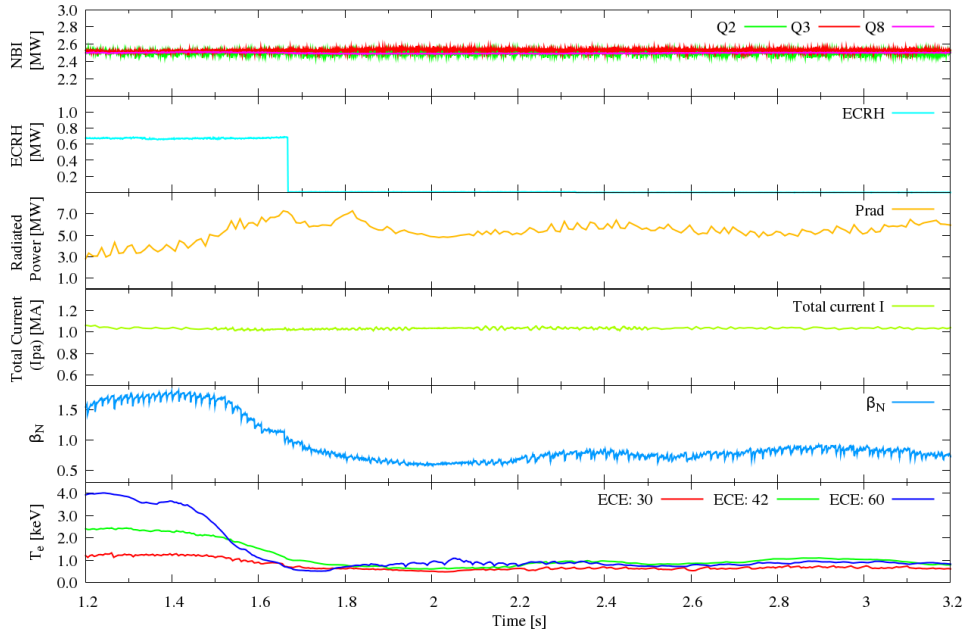


Figure 5.9: Discharge #25604 has a flat top current of 1.0 MA, a central line averaged density of $7.8 \cdot 10^{19} \frac{1}{m^3}$ and an axis toroidal magnetic field of -2.48 T. The NBI heating is 7.5 MW and an ECRH heating of 0.7 MW is turned on until 1.668 s. Various ECE channels shows the development of the electron temperature. The ECE channels #60, #42 and #30 are around $\rho_{pol} \approx 0.15$, 0.55 and 0.80, respectively. The plasma is an H-mode, when the temperature decrease starts due to tungsten accumulation at 1.45 s.

The MHD mode occurs at 1.661 s and 0.9 keV central temperature, shortly before the ECRH is switched off. The mode can be characterised with Mirnov coils as a (2/1) mode. In addition, an ECE phase jump can be observed for $\rho_{pol} \approx 0.58 - 0.64$, which indicate that the observed mode is an island. The location of the (2/1) island cannot be determined for all times, because the ECE is not available for ρ_{pol} between 0.64 and 0.78 for this discharge. But we assume that the island is close to $\rho_{pol} \approx 0.6$. The q_{95} -value is 4.25 when the mode starts, decreases to 4.1 at 2.0 s and stays constant until 4.0 s.

The (2/1) island in Figure 5.8 arise at a frequency, which correspond to the plasma rotation at $\rho_{pol} \approx 0.58$ and accelerates right from the start within 120 ms until it reaches the plasma rotation at $\rho_{pol} \approx 0.3$. At the same time the initially peaked plasma rotation profile flattens for central ρ_{pol} -values. After the initial acceleration the rotation of the (2/1) mode is faster than that of the plasma at the $q = 2$ surface. Furthermore, after 2.2 s the plasma rotation at $\rho_{pol} > 0.4$ decreases while the (2/1) mode and the plasma at $\rho_{pol} \approx 0.2 - 0.3$ stay at a similar frequencies. This indicates that the plasma at the inner ρ_{pol} could be responsible for the rotation of the (2/1) mode.

In order to investigate coupling effects, the $q = 1$ surface was determined via the sawtooth inversion radius for different times at ρ_{pol} between 0.2 and 0.3. This indicates that the (2/1) mode is synchronised with the plasma rotation at the $q = 1$ surface, which could be possible if a coupled (1/1) mode exists. Due to the tungsten accumulation for this discharge, the FFT analysis of SXR is very uncertain. However, the FFT analysis from ECE show a strong amplitude for inner ρ_{pol} -values, which is shown in Figure 5.10. Note, that the ECE has a maximum resolution of 31.25 kHz and the observed mode frequency is higher than the Nyquist frequency of the ECE (see section 4.1). However, even if the frequency cannot be determined with ECE, the FFT amplitude and the phase jumps of the mode can still be investigated.

The strong amplitude of inner ρ_{pol} -values show a dominating central mode. This strengthens our assumption that a strong inner mode can drag the outer MHD mode. However, this is only possible if the (1/1) mode has a connection to the plasma rotation and cannot move freely in the plasma rest frame. One possibility for this connection could be the NTV, which will be discussed in the next chapter. In addition, Figure 5.8 shows that the diamagnetic effects can be neglected in this case, due to the flat temperature profiles.

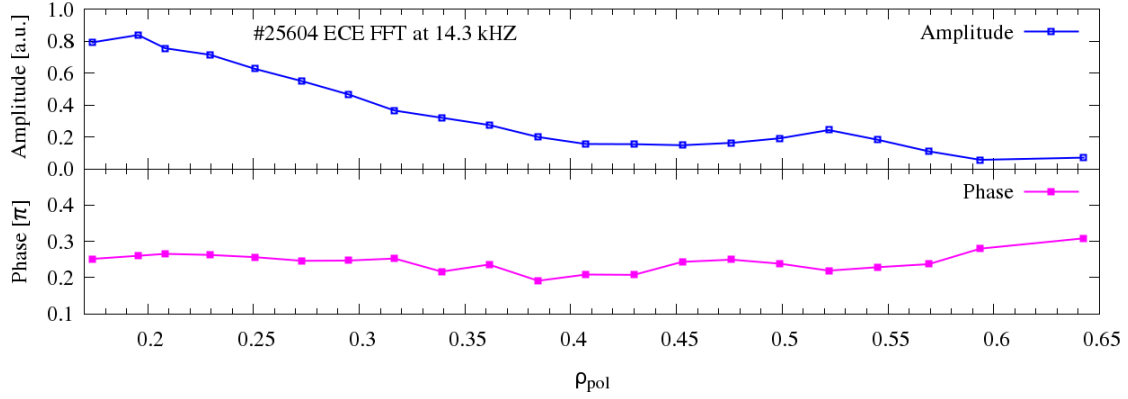


Figure 5.10: The FFT analysis with ECE for discharge #25604 and the frequency of 14.3 kHz at 1.84 s. The strong central amplitude indicate the existence of a (1/1) mode, which is coupled to the (2/1) MHD mode. There is no phase jump of ECE at this time to determine the location of the (2/1) mode.

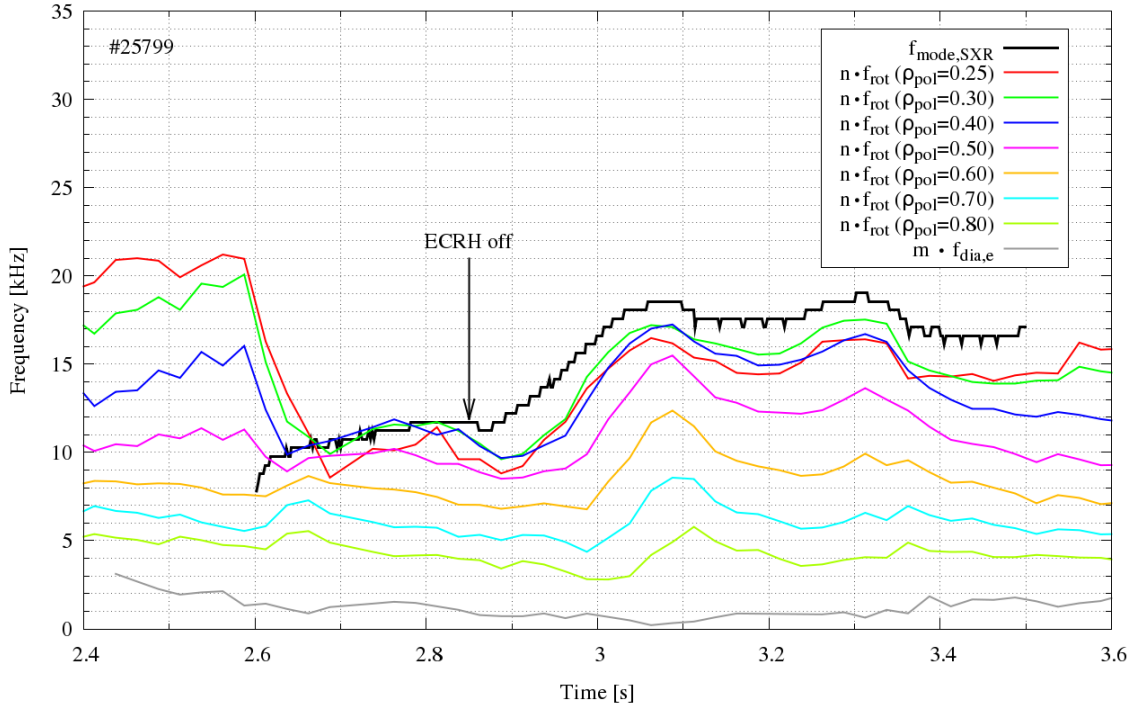


Figure 5.11: The rotation comparison during discharge #25799 confirms the observation of the rotation profile flattening after mode formation. Discharge #25799 is an H-mode with 1.0 MA flat top current, $8.3 \cdot 10^{19} \frac{1}{\text{m}^3}$ central line averaged density and -2.53 T axis toroidal magnetic field. The NBI heating is 7.5 MW and the ECRH works with 1.7 MW until 2.86 s, and is then switched off.

Another (2/1) island with flat temperature profile occurs during discharge #25799 at $\rho_{pol} \approx 0.6$ (see Figure 5.11). It starts at 2.592 s at a frequency, which corresponds to the plasma rotation at $\rho_{pol} \approx 0.6$. Right from the start the island accelerates and the plasma rotation profile flattens and becomes even slightly inverse. The $q = 1$ surface was determined around $\rho_{pol} \approx 0.3$ with sawteeth in SXR. Additionally, a large FFT amplitude at inner regions was observed in ECE, which indicates mode coupling. After the flattening of the plasma rotation the (2/1) island rotates faster than the plasma at $\rho_{pol} = 0.6$ and fits better to the plasma rotation of the $q = 1$ surface. The deviation between the $q = 1$ surface and the MHD mode rotation could be explained by the uncertainty. In addition, it can be seen, that after the ECRH is switched off, the rotation of the plasma and the mode increases noticeably.

Chapter 6.

Neoclassical Influence on MHD Mode Rotation

It was shown in the previous chapter, that the comparison of the MHD mode rotation with the plasma shows a discrepancy, if we assume that the island rotation is determined by the plasma rotation and the electron diamagnetic drift. One possible correction which could explain the observed rotation frequencies is given by the *Neoclassical Toroidal Viscosity* (NTV) theory, which describes two major effects. One effect is that the toroidal plasma flow is damped in the presence of an MHD mode. Secondly, NTV adds an additional offset for the MHD mode rotation directed in the direction of the ion flow [6].

6.1. Determination of the NTV Regime

NTV originates due to a non ambipolar radial particle drift in the plasma, when the toroidal flux symmetry is broken. This theory predicts a neoclassical toroidal offset velocity for MHD modes, which is proportional to the ion temperature gradient, as it was introduced in section 2.7. Additionally, the neoclassical offset velocity depends on the NTV regime of the plasma.

The two relevant NTV regimes for low collisionality plasmas are the $(1/\nu)$ -regime and the (ν) -regime. The limit between these regimes is determined by $q\omega_E$, where ω_E is defined as the $\mathbf{E} \times \mathbf{B}$ poloidal drift frequency $\omega_E = \frac{E_r}{rB_\phi}$. In order to determine the regime in ASDEX Upgrade, the radial electric field E_r is estimated. Equation 2.4 can be used for a stationary case to obtain the radial electric field as:

$$E_r = \frac{(\nabla p_\alpha)_r}{q_\alpha n_\alpha} - (\mathbf{v}_\alpha \times \mathbf{B})_r \quad (6.1)$$

Here, the index α represents a certain particle species in the plasma. This equation shows, that the radial electric field is generated by the pressure gradient and the velocity of the particles. For the calculation it is convenient to rewrite this equation as:

$$E_r = \frac{(\nabla p_\alpha)_r}{q_\alpha n_\alpha} - (v_{\theta,\alpha} B_\phi - v_{\phi,\alpha} B_\theta) \quad (6.2)$$

where, $v_{\theta,\alpha}$ is the poloidal and $v_{\phi,\alpha}$ the toroidal velocity. The determination of the electric field requires only the consideration of one species, since there can be only one electric field. For our estimation of the radial electric field we use the impurity ions from the CXRS diagnostic. According to [30], the radial electric field is dominated by the toroidal particle flow. Hence, we neglect the pressure and the poloidal velocity contribution in our estimation. Figure 6.1 shows the calculated electric field E_r for various discharges on the midplane of the LFS.

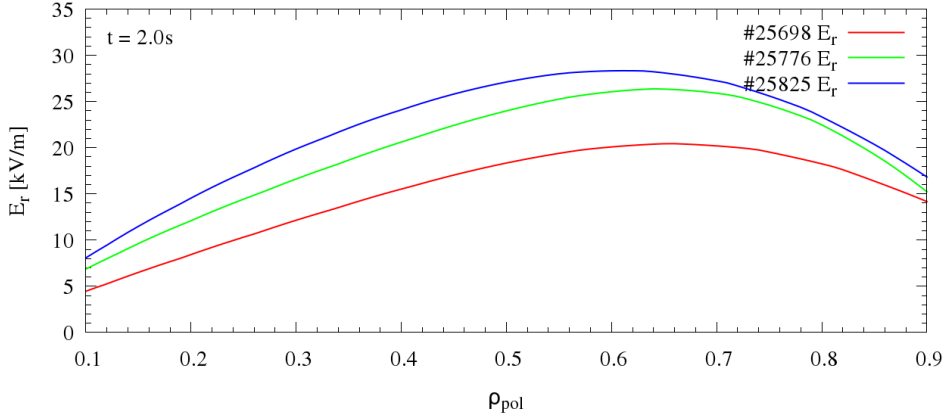


Figure 6.1: E_r measurements for various discharges in ASDEX Upgrade at $t = 2.0$ s. Because E_r is dominated by the toroidal particle flow [30], the contribution of the poloidal velocity and the pressure was neglected.

The radial electric field E_r is about $20 - 30 \frac{\text{kV}}{\text{m}}$, which is in a good agreement to previous E_r investigations in ASDEX Upgrade [30]. The calculation of the $q\omega_E$ limit is carried out using the EQH equilibrium, which provides the toroidal magnetic field B_ϕ , the q -profile and the minor radius r . Afterwards, ν_{ii}/ϵ is calculated using the following equations [47]:

$$\nu_{ii} = \frac{1}{\tau_{ii}} \quad (6.3)$$

$$\tau_{ii} = 6.60 \cdot 10^{17} \frac{(m_i/m_p)^{1/2} T_i^{3/2}}{n_i Z^4 \ln \lambda} \quad (6.4)$$

$$\ln \lambda = 17.3 - \frac{1}{2} \ln(n_e/10^{20}) + \frac{3}{2} \ln T_i \quad (6.5)$$

$$\epsilon = \frac{r}{R_0} \quad (6.6)$$

Here, τ_{ii} is the ion-ion collision time, m_i the ion mass, m_p the proton mass, T_i the ion temperature in [keV], n_i and n_e the density of ions and electrons in [m^{-3}], respectively, Z the ion charge and $\ln \lambda$ the Coulomb logarithm. In our case the calculation is performed for deuterium as main plasma ions, hence, $Z = 1$ and $m_i = 2m_p$ and we assume that $n_i \approx n_e$. The comparison of ν_{ii}/ϵ with $q\omega_E$ (see Figure 6.2) shows that ν_{ii}/ϵ is clearly below the $q\omega_E$ limit at the MHD mode location for all discharges. Therefore, the (ν) -regime is valid for ASDEX Upgrade with $k \simeq 0.92$. A further investigation of the k -factor is carried out below.

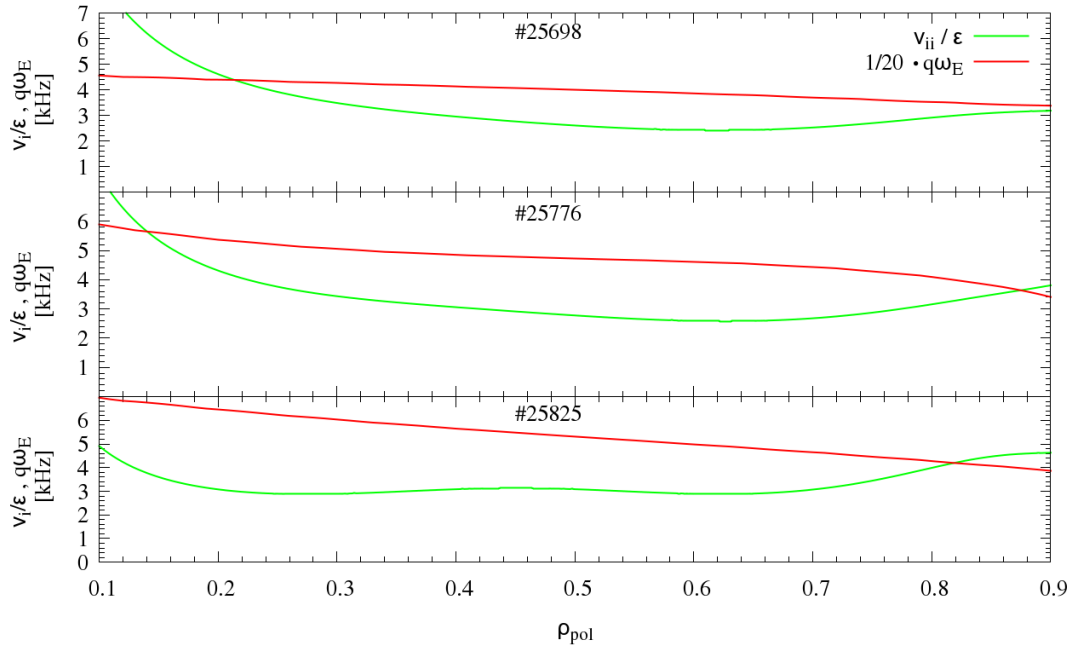


Figure 6.2: The comparison of the limit $q\omega_E$ and ν_{ii}/ϵ on the midplane of the LFS for different discharges at $t = 2.0\text{s}$. Note that $q\omega_E$ is divided by 20, for a better comparison. All discharges show, that ν_{ii}/ϵ is clearly below the $q\omega_E$ limit.

6.2. (3/2) Mode Rotation with the Neoclassical Offset

Two models are used for the expected MHD mode rotation. In the first model we use the same approach as it was discussed in chapter 5 and assume that the magnetic island rotates in the plasma rest frame with the electron diamagnetic drift offset. In addition we assume that the MHD mode field perturbation interacts with trapped particles and produces a neoclassical toroidal velocity offset, which is added to the island rotation. This offset is determined at the island location with the ion temperature gradient from CXRS and the EQH equilibrium. Furthermore, the toroidal mode number n is taken into account. The frequency of this model will be called $f_{mode,I}$:

$$f_{mode,I} = n \cdot f_{plasma} - m \cdot f_{dia,e} + n \cdot f_{nc} \quad (6.7)$$

The second model is used to investigate if the electron diamagnetic drift is required to describe the island rotation. The reason for this assumption is that the neoclassical offset contribution allows that the island has an additional differential rotation and is therefore not necessarily *frozen* in the electron flow. Hence, the electron diamagnetic drift will be neglected in this model. The frequency of this model will be called $f_{mode,II}$:

$$f_{mode,II} = n \cdot f_{plasma} + n \cdot f_{nc} \quad (6.8)$$

Furthermore, the calculation of the MHD mode frequency with the electron diamagnetic drift frequency but without the neoclassical offset, as it is described in section 2.6, will be shown for comparison as $f_{mode,0}$.

The comparison of the observed MHD mode frequency from SXR with the different models is shown in Figure 6.3 for discharge #25698. The development of the island locations was considered in the calculation. Individual components for the frequency calculations are shown as dashed lines in the graph. As can be seen, the determination of the mode frequency $f_{mode,0}$ does not describe the measured data at all. The consideration of the neoclassical offset velocity in the first model $f_{mode,I}$ increases the expected frequency to the previous plasma rotation level and fits better to the measured island frequency f_{SXR} . Especially, shortly after the mode formation, $f_{mode,I}$ can describe the measured frequency rather well. During the presence of the island $f_{mode,I}$ is slightly lower than the plasma rotation, but it can still describe f_{SXR} , if the uncertainties are considered¹.

¹The uncertainty estimation of $f_{mode,0}$ is described in section 5.1. In order to get the uncertainty of $f_{mode,I}$ and $f_{mode,II}$ the possible uncertainty of the CXRS measurement of the ion temperature gradient has to be taken into account.

The frequency of the second model $f_{mode,II}$ is slightly higher than the observed mode frequency for all times. But with the exception of the MHD mode formation, also $f_{mode,II}$ can describe the observed MHD mode rather well.

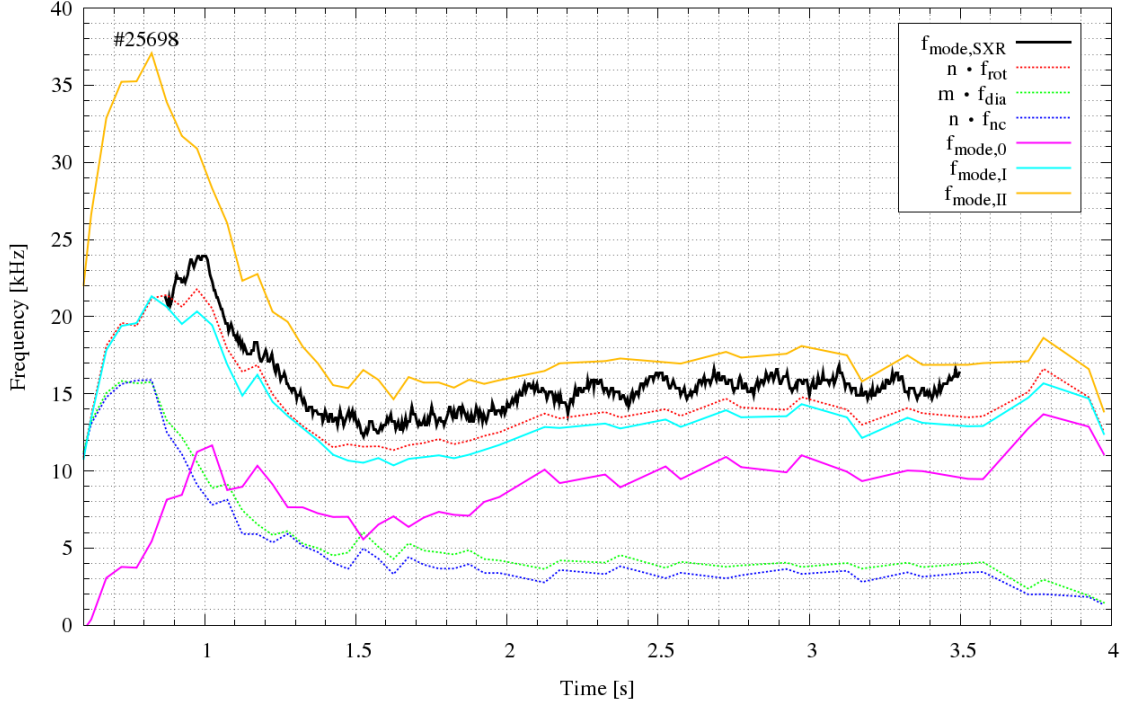


Figure 6.3: The comparison of the expected mode rotation frequency during discharge #25698, for different models. The frequency $f_{mode,0}$ considers the plasma rotation together with the electron diamagnetic drift. The additional contribution of the neoclassical offset is considered in $f_{mode,I}$. The frequency $f_{mode,II}$ considers the neoclassical offset, but neglects the diamagnetic drift velocity.

A similar observation for the MHD mode frequency is found for discharge #25776 (see Figure 6.4) and for discharge #25825 (see Figure 6.5). In both discharges $f_{mode,I}$ and $f_{mode,II}$ describe the observed frequency much better than the frequency $f_{mode,0}$. Additionally, both discharges show that at the most times the frequency of the first model $f_{mode,I}$ is slightly lower, than the observed frequency, while the frequency of the second model $f_{mode,II}$ is slightly higher. The deviation of the observed frequency is smaller for $f_{mode,II}$, which could indicate that $f_{mode,II}$ describes the MHD mode rotation better than $f_{mode,I}$.

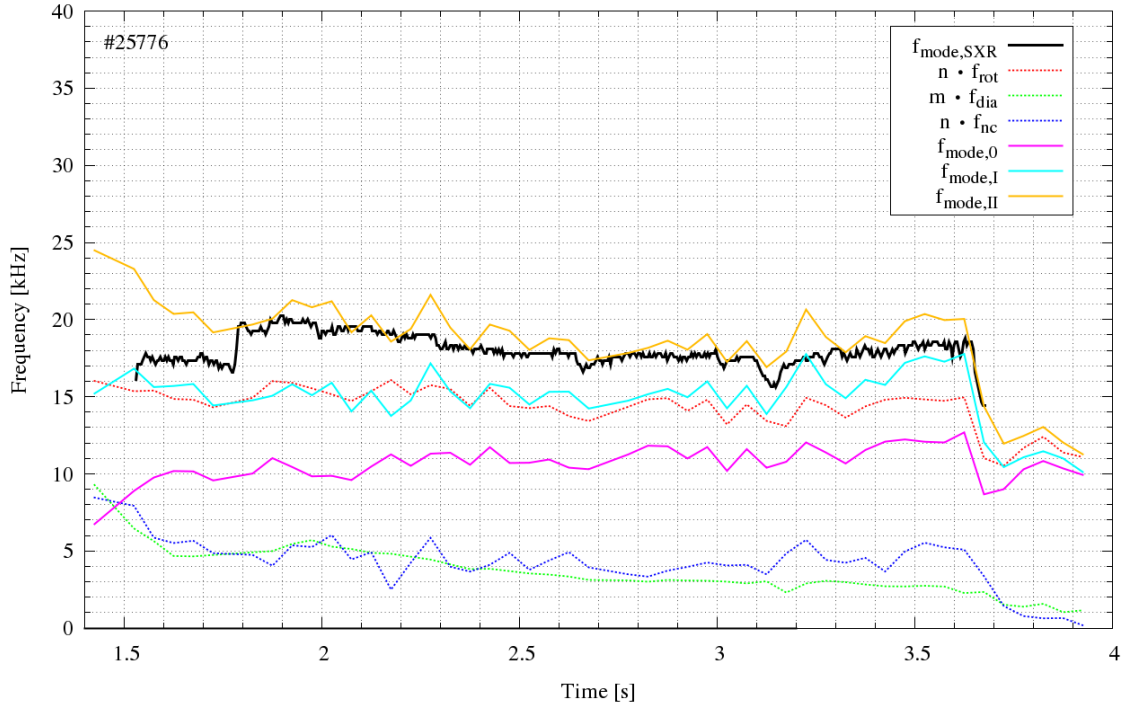


Figure 6.4: The comparison of the expected island rotation frequency for different models during discharge #25776.

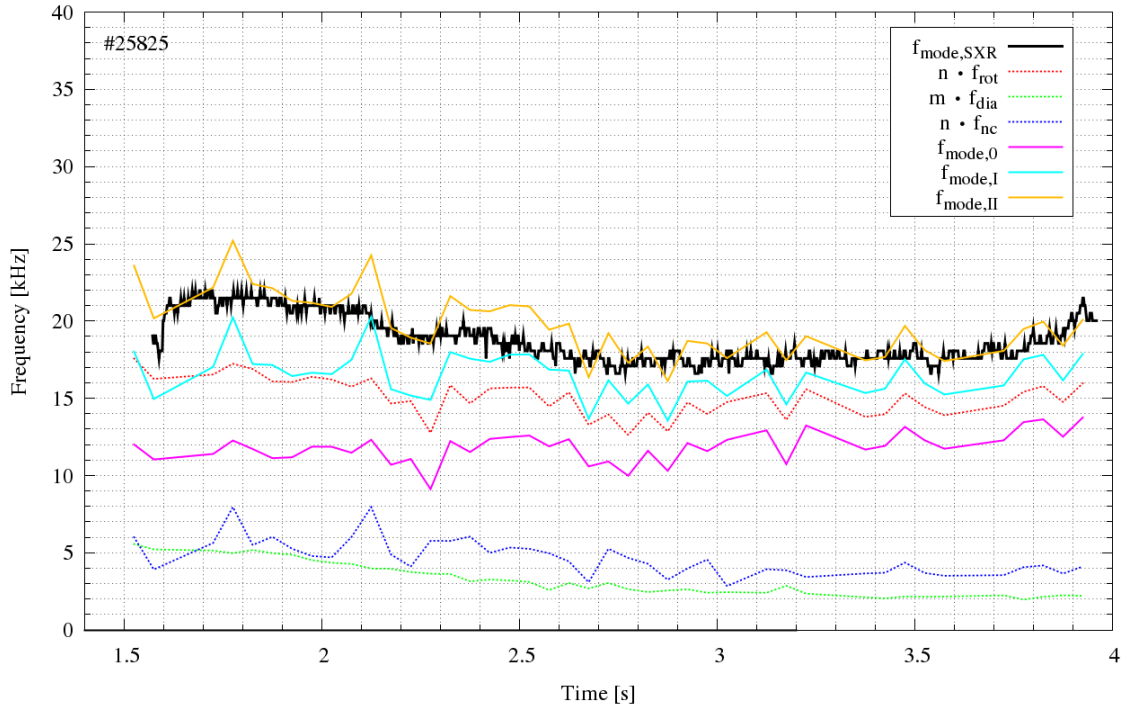


Figure 6.5: The comparison of the expected island rotation frequency for different models during discharge #25825.

However, there are several aspects, which have to be considered as well. One aspect is the CXRS measurement. CXRS determines the velocity of impurity ions. But the plasma rotation is determined by the main plasma ions, which rotate slightly faster, as it was explained in section 4.2. Hence, CXRS underestimates the plasma rotation frequency.

Furthermore, it was shown in section 5.2 that the mode coupling could influence the MHD mode rotation frequency as well. The inner MHD mode can rotate faster and drag the outer MHD mode. Thus, the observed island frequency f_{SXR} can be faster with mode coupling than expected for a single (3/2) island.

Moreover, the determination of the neoclassical toroidal velocity offset is proportional to a k -factor, which depends on the plasma regime. The determined plasma regime in ASDEX Upgrade is the (ν) -regime with $k \simeq 0.92$. However, if the plasma is not deeply in the (ν) -regime, the k -factor can be between 0.92 and 3.5. Since all these effects lead to an underestimation of the expected mode frequency, it seems more likely that $f_{mode,I}$ fits the observed mode frequency better than $f_{mode,II}$.

Evaluation of the Coefficient k

The neoclassical offset velocity is directly proportional to the k -factor (equation 2.29). The NTV theory predicts two relevant regimes for currently operated tokamaks, with $k \simeq 3.5$ for the $(1/\nu)$ -regime and $k \simeq 0.92$ for the (ν) -regime. But there is no theory for the development of the k -factor between these regimes.

We determined the k -factor for which the calculated frequency of $f_{mode,I}$ and $f_{mode,II}$ fits the observed MHD mode frequency f_{SXR} . The evaluation of the k -factor is shown in Figure 6.6. In the first model the k -factor is between 1 and 2. This could indicate that the plasma is still not very deep in the (ν) -regime and k could be between 0.92 and 3.5. On the other hand, the k -factor of the second model is mostly below 0.92, especially for discharge #25698. This is lower than predicted by the neoclassical theory and cannot be explained by the transition between the regimes. Furthermore, if we consider the influences of coupled inner modes and the possibility of a too low velocity measurement, k will decrease in both cases. This will lead to a better agreement of the k -factor with the first model. Hence, the electron diamagnetic drift frequency should be included in the island rotation.

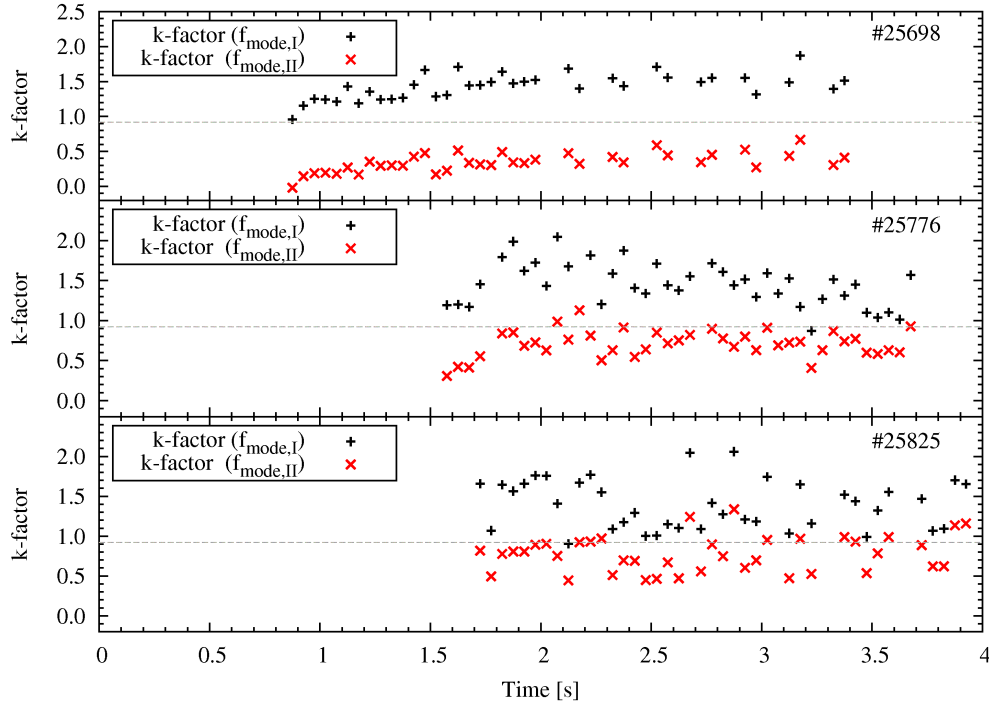


Figure 6.6: The evaluation of the k -factor for different discharges and models. The dashed line shows $k = 0.92$ for the (ν) -regime. The k -factor of the first model is between 1 and 2. In the second model the coefficient k is mostly below 0.92.

6.3. (2/1) Modes with Flat Temperature Profiles

The investigation of the (2/1) MHD modes in the previous chapter leads to the question, whether the neoclassical toroidal velocity offset can be used to explain the observed rotation frequency. These (2/1) MHD modes are remarkable because of the flat temperature profiles, which occur due to tungsten accumulation in the plasma core. Therefore, all offset velocities, like the electron diamagnetic drift velocity and the neoclassical offset should have a small contribution.

The tungsten accumulation causes a lower ion temperature. Therefore, the ν_{ii}/ϵ quantity is expected to be higher, which could change the NTV regime. Hence, a verification of the NTV regime is necessary. The comparison of ν_{ii}/ϵ and $q\omega_E$ is demonstrated in Figure 6.7. Note, that $q\omega_E$ is divided by a factor of 10 for comparison. Therefore, it is clear that ν_{ii}/ϵ is lower than the $q\omega_E$ limit and it can be stated that the (ν) -regime is valid in this case.

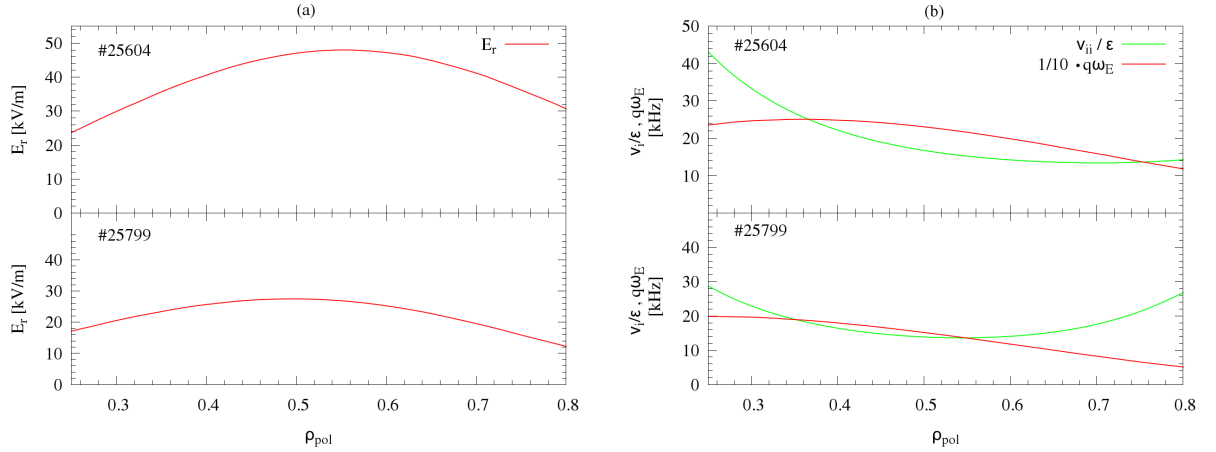


Figure 6.7: (a) The electric field during MHD mode occurrence. (b) The comparison of the $q\omega_E$ limit and ν_{ii}/ϵ . Note that the $q\omega_E$ limit is divided by 10 for better comparison. Both graphs show discharge #25604 at $t = 2.0$ s and discharge #25799 at $t = 3.0$ s.

The comparison of the observed (2/1) MHD mode rotation with different rotation models is shown in Figure 6.8 and Figure 6.9. Additionally, the coupled (1/1) MHD modes are compared in these figures, since it was observed that they could be responsible for the mode rotation. Note, that the electron diamagnetic drift can be neglected for the (1/1) MHD modes, because these modes are assumed to be ideal. Hence, $f_{mode,0}$ is equal to the plasma rotation and $f_{mode,I}$ is equal to $f_{mode,II}$ for the (1/1) modes.

It can be seen that the contribution of the electron diamagnetic drift velocity and the neoclassical toroidal offset velocity for both (2/1) MHD modes is very small. Hence, both models $f_{mode,I}$ and $f_{mode,II}$ are approximately equal to the plasma rotation. As can be seen the rotation of both (2/1) modes can be described only at the formation time. Afterwards, both modes accelerate and rotate much faster than predicted by any of these models.

The expected rotation frequency of the (1/1) MHD modes from our models fits better to the measured mode frequency. This is because of the higher ambient plasma rotation at $q = 1$. For these cases the neoclassical offset velocity varies strongly and can even be negative, since the ion temperature from CXRS shows hollow profiles. Thus, the neoclassical components cannot improve the description of the MHD mode rotation. However, these cases demonstrate that the rotation of the (2/1) MHD mode can be dominated by the rotation of the coupled (1/1) MHD mode. Therefore, mode coupling should be taken into account for the investigation of the MHD mode rotation.

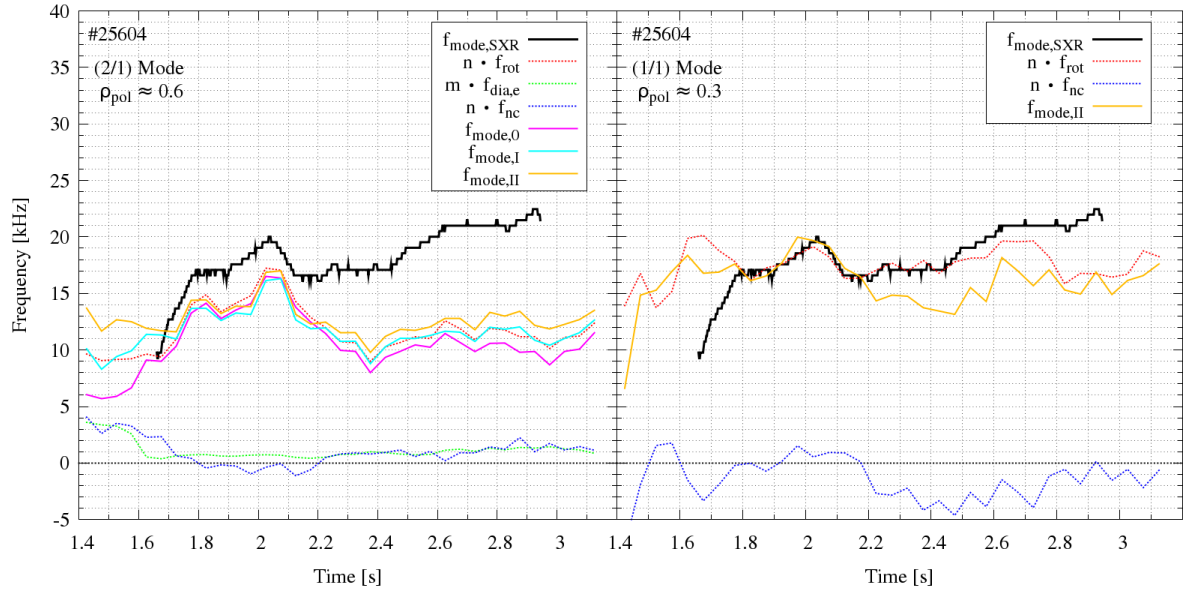


Figure 6.8: The comparison of MHD mode rotation for discharge #25604. The observed mode frequency is compared with the models for a (2/1) mode located at $\rho_{pol} \approx 0.6$ (left) and for a (1/1) mode located at $\rho_{pol} \approx 0.3$ (right).

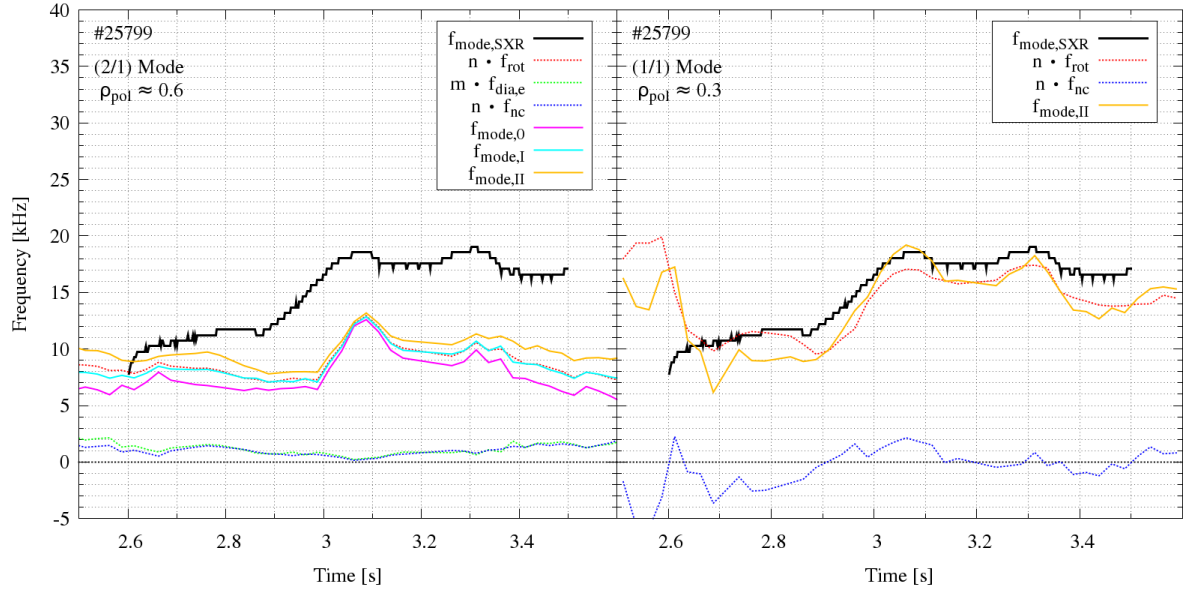


Figure 6.9: The comparison of MHD mode rotation for discharge #25799. The observed mode frequency is compared with the models for a (2/1) mode located at $\rho_{pol} \approx 0.6$ (left) and for a (1/1) mode located at $\rho_{pol} \approx 0.3$ (right).

6.4. Neoclassical Torque

The magnetic field perturbation of an MHD mode will break the axis symmetry of the tokamak equilibrium, which causes a radial nonambipolar drift of the trapped particles. This can generate a $\mathbf{j} \times \mathbf{B}$ torque and cause a deceleration of the plasma flow. Since MHD modes are moving in the plasma rest frame, we can argue that the torque can not only affect the plasma rotation, but also the rotation of MHD modes. If two coupled MHD modes are present in a plasma, the torque will be generated by both MHD modes. The torque can be calculated using the expression given by [18]:

$$t_{\Phi,NTV} = K \cdot \sum_{m,n} |nb_{m,n}|^2 W_{m,n} \cdot \left([\omega_{rot} + \sum \omega_{offset}] - \omega_{MHD} \right) \quad (6.9)$$

with

$$K = 1.74 n_e \frac{e T_i}{2 \nu_{ii}} R B_{\Phi} \epsilon^{3/2} \langle R \rangle \langle B_{\Phi}^{-1} \rangle \langle R^{-2} \rangle \quad (6.10)$$

Here, n_e is the electron density, T_i the ion temperature, ν_{ii} the ion-ion collision frequency, R the major radius, B_{Φ} the toroidal magnetic field. The $\langle \rangle$ represent the average of the quantity on a flux surface. The observed MHD mode frequency is described by ω_{MHD} and the plasma rotation by ω_{rot} . The rotation contributions, which generate an offset velocity are described by $\sum \omega_{offset}$. The coefficients $b_{m,n}$ represent the normalized perturbed magnetic field and can be calculated with equation 2.22 from the displacement function ξ . The calculation of $b_{m,n}$ for the toroidal geometry is shown in appendix A and the determination of $W_{m,n}$ in appendix B.

In this equation $K, b_{m,n}, W_{m,n}$ and ω_{rot} are profiles of ρ_{pol} . The frequencies $\sum \omega_{offset}$ are the offset velocity values at the MHD mode location. This equation describes that the torque will be 0 at that location, where the plasma rotation and all assumed offset frequencies will be equal to the observed MHD mode frequency. The other regions will have a non vanishing torque.

The coefficients $b_{m,n}$ and $W_{m,n}$ in equation 6.9 depend on the q -profile. Since the q -profile from the CLISTE reconstruction is not very accurate for the plasma core, we have used the positions of the observed MHD mode, the $q = 1$ surface and the q_{95} value to obtain an adapted q -profile. The determination of the q -profile was carried out as a spline of the three points over their position with the boundary condition $0 = \frac{dq}{d\rho_{pol}}$ at $\rho_{pol} = 0$.

Furthermore, we determined from the FFT analysis of the ECE the radial displacement function $\xi_r(r)$, which is required to measure the magnetic perturbation $b_{m,n}$:

$$\xi_r = \frac{\Delta T_e}{\frac{\partial T_e}{\partial r}} \quad (6.11)$$

Here, ΔT_e is the temperature fluctuation from the FFT amplitude and $\frac{\partial T_e}{\partial r}$ the temperature gradient, which is time averaged for the time interval of the FFT analysis. The displacement ξ_r could be determined only for discharges with non zero temperature gradient, in order to avoid diverging ξ_r . For this reason, ξ_r could not be determined for discharges with (2/1) MHD modes and flat temperature profiles.

The observed displacement ξ_r is shown exemplary for discharge #25698 and $t = 1.82$ s in Figure 6.10. The expected (3/2) island amplitude from the ECE has a minimum at its X-point and a maximum left and right from the X-point. The distance of these maxima correspond approximately to the island width [31]. This specific signal shape can be recognised in our observations around $\rho_{pol} \approx 0.46$, which confirms that the present MHD mode is a (3/2) island. Additionally, ECE has an amplitude further inside. This indicates the existence of the coupled (2/2) mode, as it was predicted by SXR (see section 5.1).

Since there are two coupled modes, the displacement is subdivided in two parts. One part represents the (3/2) mode and the other represents the (2/2) mode. The composition of the signal is not exactly known, since it depends on the mode eigenfunctions ξ and on their phase coupling. Therefore, we assumed that the (2/2) mode dominates for $\rho_{pol} < 0.25$ and the (3/2) mode dominates for $\rho_{pol} > 0.40$. The region of ρ_{pol} between 0.25 and 0.40 was subdivided linearly. The fractional contribution is shown in Figure 6.10 as weighting factor. Additionally, we add the following constraints for the displacement: $\xi_r \equiv 0$ at $\rho_{pol} = 0$ with a linear decay and $\xi_r \equiv \frac{1}{e} \cdot \xi_{r,last}$ at $\rho_{pol} = 0.7$ with an exponential decay. Here, $\xi_{r,last}$ is the last measured ECE amplitude.

We used the experimental determination of the displacement to calculate the $b_{m,n}$. Afterwards, the torque could be evaluated for both MHD modes individually. We have used equation 6.9 with different offset contributions $\sum \omega_{offset}$ for each MHD mode. It is assumed that the rotation frequency of the (3/2) island has an electron diamagnetic drift offset $\omega_{dia,e}$ and a neoclassical offset ω_{nc} . The (2/2) MHD mode is assumed to be ideal. Thus, it is expected that this mode has no offset contribution due to the electron

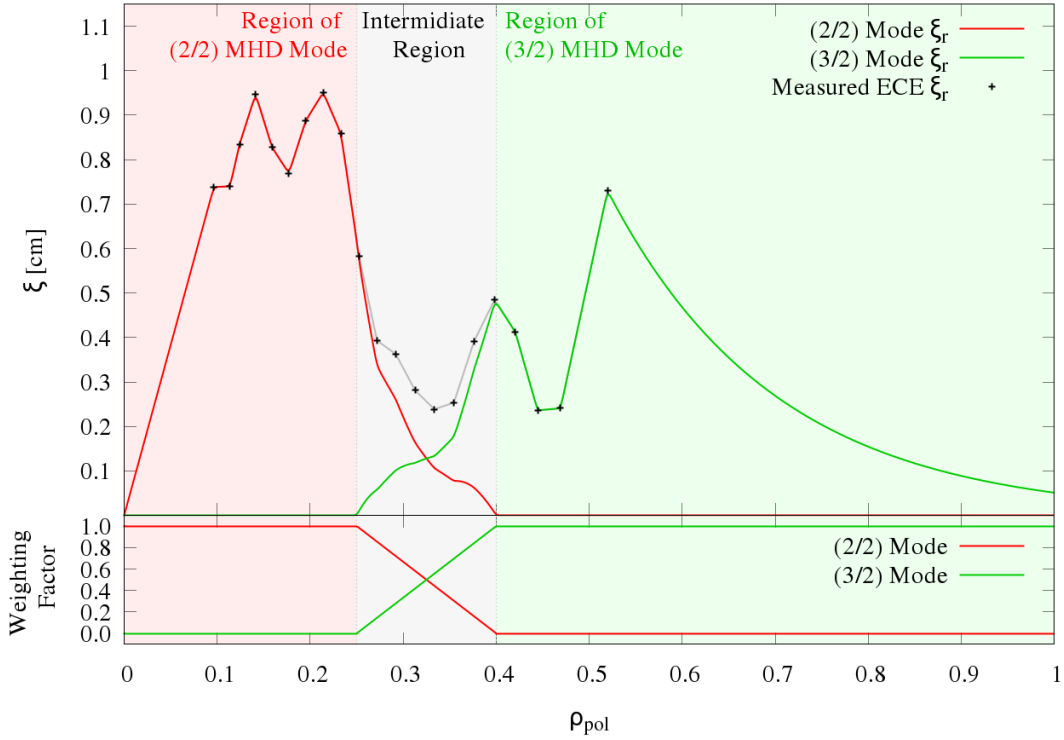


Figure 6.10: The black points in the right graph represent the observed displacement ξ_r for discharge #25698 at $t = 1.82$ s. The displacement is subdivided on two MHD modes. The green line represent ξ_r of the (3/2) island and red line the (2/2) MHD mode. The used weighting factor is shown in the bottom graph on the right.

diamagnetic drift. Therefore, only the neoclassical offset ω_{nc} was taken into account for the (2/2) MHD mode. All offsets were calculated at the position of the rational surface of the corresponding mode.

The result of the calculation is shown in Figure 6.11. It can be seen, that the torque acts decelerating on the central plasma rotation and accelerating on the outer plasma flow. This is consistent with the observations by [18]. On the other hand, the torque can also influence the rotation of the MHD modes. According to Newtons third law, we can determine the torque on the MHD modes by inverting the torque on the plasma. Hence, the fast central plasma rotation will try to accelerate the coupled MHD modes, while the slow outer plasma will try to decelerate them. If we integrate the torque function, the total torque on the MHD modes can be calculated. If the total torque is negative, it will decrease the MHD mode rotation. If it is positive, it can increase the MHD mode rotation. The *natural* velocity of the MHD modes in a stationary state could be determined, if the total torque is vanishing.

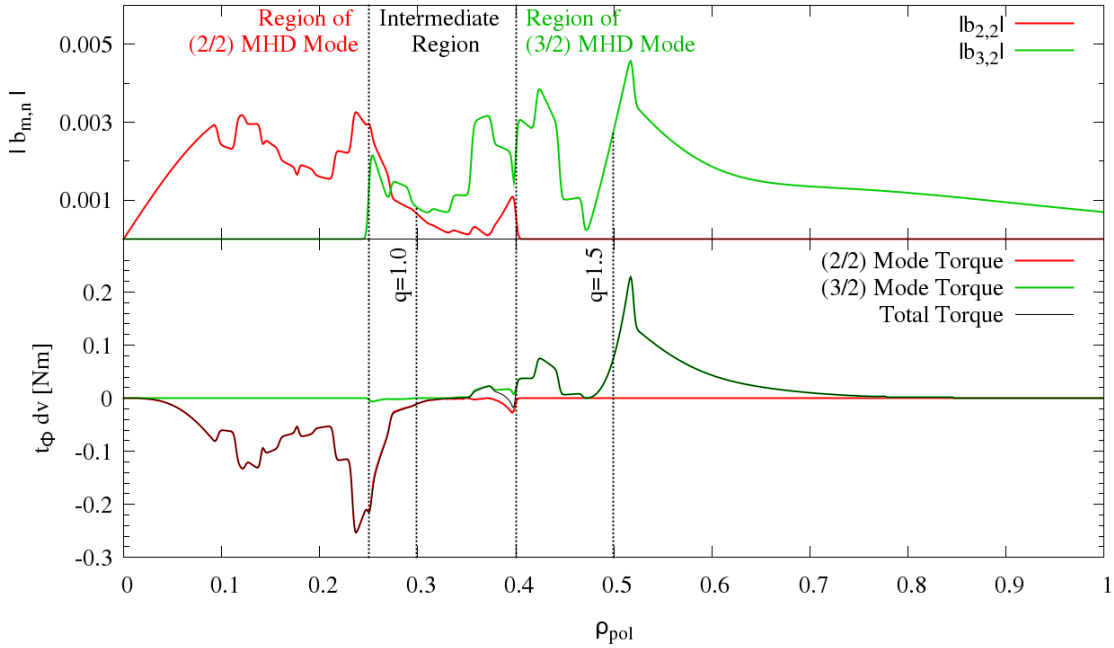


Figure 6.11: The top graph shows the determined $b_{m,n}$ for discharge #25698 and $t = 1.82$ s. The graph below illustrate the calculated torque of both MHD modes.

6.5. Determination of the Frequency with Vanishing Torque

The previous determination of the torque was carried out with the observed MHD mode frequency. The torque is usually used to explain the deceleration or the acceleration of the plasma rotation shortly after an MHD mode occurs. However, in a stationary case the plasma rotation does not change and we can use the torque to investigate the MHD mode rotation. We can vary an assumed MHD mode frequency and calculate the torque. With this variation the *natural* MHD mode frequency should be obtained, where the total torque is 0. If we carry out this calculation for the case which is shown in Figure 6.11 the frequency with vanishing torque is determined at $f = 14.5$ kHz. This corresponds well with the observed MHD mode frequency of $f = 13.9$ kHz.

The determination of the frequency with vanishing torque has been used for discharges #25698, #25776 and #25825. In addition we have used different assumptions for the offset velocities, in order to find the *natural* MHD mode frequencies (see Table 6.5). Model I considers the toroidal neoclassical offset velocity f_{nc} at the position of each MHD mode.

Additionally, the (3/2) island mode is assumed to have electron diamagnetic offset contribution. Model II neglects f_{nc} for both modes. Model III is similar to the first Model, but it is assumed that the inner (2/2) MHD mode has an additional contribution due to the ion diamagnetic drift velocity $f_{dia,i}$. Model IV considers only the neoclassical offset velocity, without all diamagnetic drifts. Finally, Model V assumes no offset velocities at all.

| | (2/2) ideal mode | (3/2) magnetic island |
|------------------|--------------------------------------|--------------------------------------|
| Model I | $n \cdot f_{nc}$ | $n \cdot f_{nc} - m \cdot f_{dia,e}$ |
| Model II | — | $-m \cdot f_{dia,e}$ |
| Model III | $n \cdot f_{nc} + m \cdot f_{dia,i}$ | $n \cdot f_{nc} - m \cdot f_{dia,e}$ |
| Model IV | $n \cdot f_{nc}$ | $n \cdot f_{nc}$ |
| Model V | — | — |

Table 6.1: Assumed offset contributions of the expected MHD mode rotation frequency for the (3/2) island and the (2/2) ideal mode.

The offsets velocities were calculated at the rational surface of each MHD mode. The results of the modulated MHD rotation frequencies, for which the torque becomes 0, is shown in Figure 6.12. Surprisingly, discharge #25698 shows the best agreement of the observed MHD mode rotation for model V. But also model I can describe the observed MHD mode rotation quite well, with the exception of the time shortly after mode formation. It has to be mentioned, that the uncertainty of model I is much larger than for model V, because the offset velocities are dependent on the temperature gradients. This could explain the larger scatter. Furthermore, model II underestimates the mode frequency, while model III and model IV show a tendency of overestimation. This can be understood if we clarify the effects of our assumptions. For example, if the $\omega_{rot} + \sum \omega_{offset}$ term becomes larger due to electron diamagnetic drift frequency, the expected MHD mode frequency f_{MHD} must increase to compensate the additional torque. On the other hand if we neglect the neoclassical offset contribution or subtract the electron diamagnetic drift velocity, the expected MHD mode rotation is decreased.

The further analysis of discharges #25776 and #25825 shows a similar picture. Both models, I and V can describe the MHD mode rotation quite well. One possible explanation for this could be that the neoclassical offset velocity has a similar size as the electron diamagnetic contribution (see Figure 6.3 - Figure 6.5), thus these offset velocities can cancel each other. The remaining difference of these models is the neoclassical offset

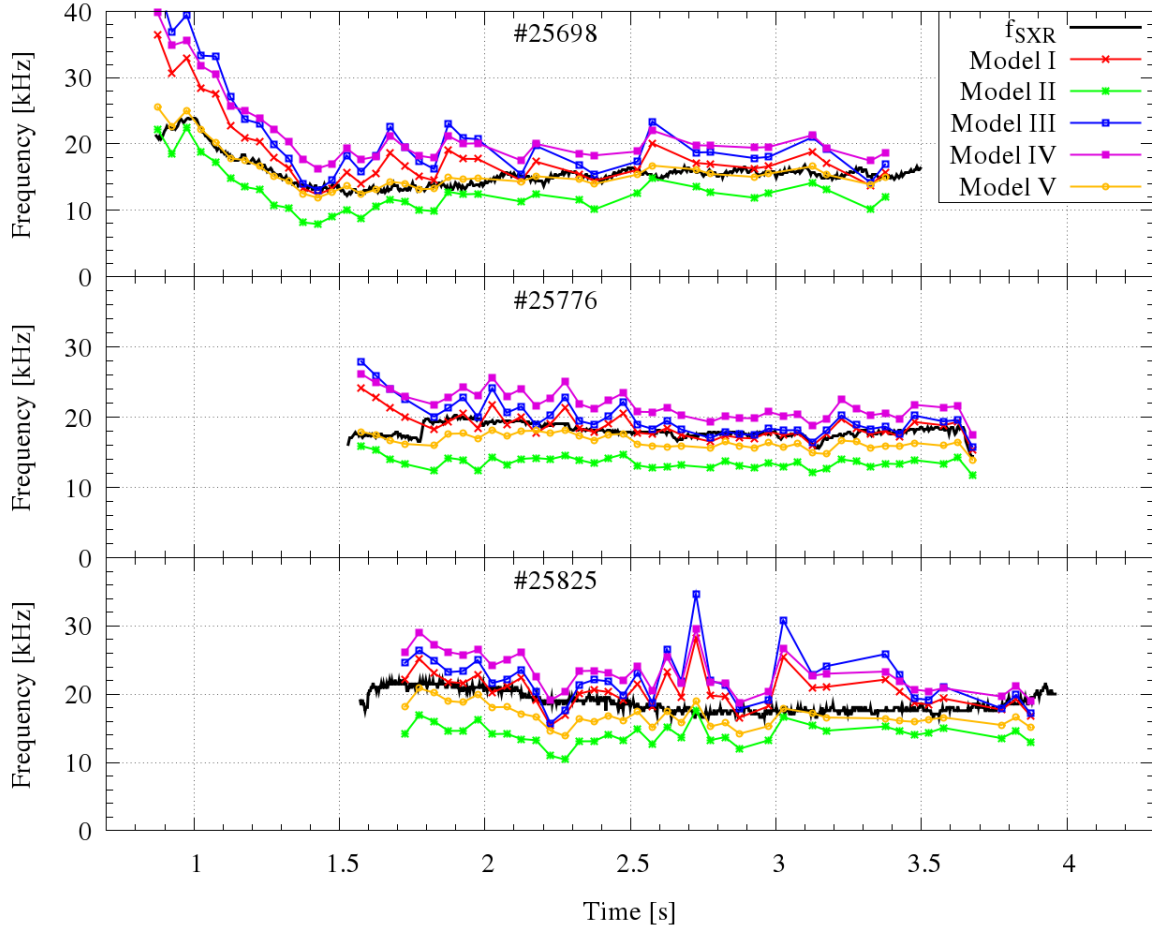


Figure 6.12: The determined frequency with vanishing torque for various discharges.

contribution of the inner coupled mode. This leads to a higher expected MHD mode rotation for the first model in comparison with model V. However, both of these models are suitable to describe the MHD mode rotation and we cannot favour one of these models.

Figure 6.12 shows two further characteristics. First, model I and model III describe the MHD mode rotation similarly for several times during discharge #25776. This coincidence occurs, because the $(3/2)$ MHD mode dominates at these times. The inner MHD mode perturbations are small and do hardly contribute to the torque determination. Furthermore, we can compare the frequency of model I with the previous determination of the mode frequency $f_{mode,I}$ in Figure 6.4. It can be seen that $f_{mode,I}$ underestimates the observed MHD mode frequency, whereas model I includes the inner $(2/2)$ mode and has therefore a higher frequency. Hence, model I seems to fit better. However, the uncertainties of model I are much larger than of $f_{mode,I}$.

Secondly, we can see in discharge #25698 and #25776 that the determination of the frequency with vanishing torque does not describe the observed MHD mode rotation for model I shortly after MHD mode formation. This can be explained by the choice of our mode contribution to the total displacement (see Figure 6.10). This choice was fixed for all times of the analysis. However, the MHD mode location is further inside at the formation time (see Figure 5.3 and Figure 5.4). Hence, the contribution to the displacement was overestimated for the inner (2/2) mode and underestimated for the (3/2) island during the time, where the island had not its final location around $\rho_{pol} \approx 0.5$. At these times the influence of the electron diamagnetic drift was too low, resulting in a higher expected mode frequency.

Chapter 7.

Summary, Conclusions and Outlook

The goal of this work was the investigation of the rotation of magnetic islands in a tokamak plasma. Standard plasma theory expects that the rotation of a magnetic island can be described with the plasma rotation together with the electron diamagnetic drift. This follows from the condition, that the magnetic field topology is *frozen* in the electrons of the plasma. The electron diamagnetic drift adds a poloidal rotation, which contributes to the rotation in counter-current direction. Since the plasma rotation in ASDEX Upgrade is usually in current direction, islands are expected to rotate slower than the plasma. However, the opposite is usually observed in ASDEX Upgrade.

This thesis concentrates on the possible explanation of this behavior, which is given by the neoclassical viscosity theory (NTV). NTV proposes two effects which can influence the MHD mode rotation, a neoclassical torque and a neoclassical toroidal offset velocity, which is proportional to the ion temperature gradient. The effect of both contributions was investigated for the rotation of islands.

It was found that the neoclassical toroidal offset velocity is of similar size as the electron diamagnetic drift in ASDEX Upgrade. Hence, the expected island rotation will be similar to the plasma rotation if both offsets are taken into account. In the case of $(3/2)$ islands, the three components (plasma rotation, electron diamagnetic drift and neoclassical velocity offset) can be used to describe the observed MHD mode rotation if we consider several effects. One is that the measured plasma rotation by CXRS slightly underestimates the rotation of the main plasma ions. Furthermore, the neoclassical offset velocity is proportional to a factor k , which can vary between 0.92 and 3.5 for various plasma regimes. We have used $k = 0.92$ for the (ν) -regime. However, if the plasma is not exactly in this regime, the neoclassical offset velocity will be larger. These arguments would increase our

expected MHD mode rotation and we could describe the observed MHD modes.

In addition, we have found (2/1) MHD modes with flat temperature profiles, which cannot be described with the plasma rotation, the electron diamagnetic drift and the neoclassical offset velocity at the $q = 2$ surface. These MHD modes rotate with the plasma flow at $q = 1$. In these cases we have observed a strong amplitude of coupled (1/1) MHD modes with ECE, which can drag the (2/1) mode to rotate faster than the surrounding plasma. Also the (3/2) islands were coupled to (2/2) MHD modes, which are located further inside the plasma. Hence, also in this case, an increase of the (3/2) island rotation frequency due to the inner coupled (2/2) mode is likely.

In order to consider coupling effects we have calculated the neoclassical torque for the (3/2) magnetic islands. In a stationary case, where the rotation of the plasma and the MHD modes is constant, we can assume that the MHD mode rotates at a frequency, where the total neoclassical torque is vanishing. We have varied the assumed rotation frequency of the MHD mode for different models to find the frequency with vanishing torque. Two models were able to describe the experimental observations of the MHD mode rotation frequency rather well. One model assumes no offset velocities for both MHD modes. The second model assumes that the offset velocities are described by the electron diamagnetic drift and the neoclassical offset for the magnetic island and only the neoclassical offset for the inner coupled ideal mode. Since the electron diamagnetic drift and the neoclassical offset velocity of the (3/2) island cancel each other out in many cases, both models show similar results. Therefore, we cannot favour one of the models. For the (2/1) modes the torque analysis could not be carried out because of the flat temperature profiles. However, these cases show directly that mode coupling to an ideal mode can strongly influence the island rotation.

The determination of the MHD mode rotation was carried out in this thesis on a rather slow time resolution, due to the available CXRS. Therefore, one possible improvement could be a higher time resolution. With this, we could possibly look at the dynamics of MHD modes. Furthermore, the calculation of the main ion plasma flow could give more accurate plasma rotation profiles, which could be used for a more detailed study on the MHD mode rotation. Additionally, a faster ECE (Nyquist frequency higher than the mode frequency) would help to determine the displacement of the MHD modes more accurately. Finally, the experimental determination of $b_{m,n}$ could be expanded by theoretical models or simulations for coupled modes. This could improve the understanding of the torque influence to the MHD mode rotation, in case of coupled MHD modes.

Appendix A.

Determination of $b_{m,n}$

The calculation of $b_{m,n}$ can be carried out using the linearized equation of the magnetic field perturbation:

$$\mathbf{B}_1 = \nabla \times (\boldsymbol{\xi} \times \mathbf{B}_0) \quad (\text{A.1})$$

Here, $\boldsymbol{\xi}$ represents the displacement function, the index 0 the equilibrium quantity and the index 1 the perturbation. The calculation can be carried out for cylindrical coordinates (r, θ, ϕ) , where $(R\phi)$ represents the z coordinate in the cylinder.

Furthermore, we can assume a large-aspect ratio tokamak with a circular cross section. Hence, we can write that $\frac{\partial}{\partial r} \sim \frac{1}{r} \frac{\partial}{\partial \theta} \gg \frac{1}{R} \frac{\partial}{\partial \phi}$. Additionally, we can demand for the perturbation [47]:

$$\nabla \cdot \boldsymbol{\xi} = 0 \quad (\text{A.2})$$

In the approximation of the large aspect ratio we obtain the relation $\xi_r \sim \xi_\theta \gg \xi_\phi$ and $B_{r1} \sim B_{\theta 1} \gg B_{\phi 1}$. Furthermore, we must use the differential operators for cylindrical coordinates:

$$\nabla \cdot \mathbf{A} = \frac{1}{r} \frac{\partial}{\partial r} (r A_r) + \frac{1}{r} \frac{\partial A_\theta}{\partial \theta} + \frac{\partial A_z}{\partial z} \quad (\text{A.3})$$

$$(\nabla \times \mathbf{A})_r = \left(\frac{1}{r} \frac{\partial A_z}{\partial \theta} - \frac{\partial A_\theta}{\partial z} \right) \quad (\text{A.4})$$

$$(\nabla \times \mathbf{A})_\theta = \left(\frac{\partial A_r}{\partial z} - \frac{\partial A_z}{\partial r} \right) \quad (\text{A.5})$$

$$(\nabla \times \mathbf{A})_z = \left(\frac{1}{r} \frac{\partial}{\partial r} (r A_\theta) - \frac{1}{r} \frac{\partial A_r}{\partial \theta} \right) \quad (\text{A.6})$$

Now we can use the Fourier ansatz $\boldsymbol{\xi} \propto e^{i(m\theta - n\phi)}$ for the displacement together with equation A.3 to derive the relation:

$$\xi_\phi = -\frac{i}{m} \frac{\partial}{\partial r} (r \xi_r) \quad (\text{A.7})$$

This equation can be used in equation A.1 together with equations A.4 - A.6 to derive the radial perturbed magnetic field:

$$B_{r1} = (\nabla \times (\boldsymbol{\xi} \times \mathbf{B}_0))_r \quad (\text{A.8})$$

$$= \frac{1}{r} \frac{\partial}{\partial \theta} (\xi_r B_{0\theta} - \xi_\theta B_{0r}) + \frac{\partial}{\partial z} (\xi_r B_{0\phi}) \quad (\text{A.9})$$

Furthermore, in a large aspect ratio tokamak we can assume that $B_{0\theta} = \frac{r B_{0\phi}}{Rq}$ and $B_{0r} \approx 0$. Additionally, we can write $\xi_r = \tilde{\xi}(r) \cdot e^{i(m\theta - \frac{nz}{R})}$. With this the equation can be reduced to:

$$B_{r1} = im \cdot \frac{B_{0\phi}}{Rq} \cdot \tilde{\xi} \cdot e^{i(m\theta - \frac{nz}{R})} - in \cdot \frac{B_{0\phi}}{R} \cdot \tilde{\xi} \cdot e^{i(m\theta - \frac{nz}{R})} \quad (\text{A.10})$$

$$= -\frac{im B_{0\phi}}{R} \left(\frac{n}{m} - \frac{1}{q} \right) \xi_r \quad (\text{A.11})$$

The analogue calculation for the other components of the magnetic perturbations yields:

$$B_{\theta 1} = \frac{B_{0\phi}}{R} \frac{\partial}{\partial r} \left[\left(\frac{n}{m} - \frac{1}{q} \right) r \xi_r \right] \quad (\text{A.12})$$

$$B_{\phi 1} = 0 \quad (\text{A.13})$$

Using equations A.11 - A.13 we can calculate the normalized perturbed magnetic field as:

$$b_{m,n} = \sqrt{\frac{B_{r1}^2 + B_{\theta 1}^2}{B_0^2}} \quad (\text{A.14})$$

Appendix B.

Determination of $W_{m,n}$

The $W_{m,n}$ coefficients describe the influence of the magnetic perturbation. The $W_{m,n}$ coefficients are given by:

$$W_{m,n} = \int_0^1 \frac{(F_{mnc}(\kappa))^2 + F_{mns}(\kappa)^2}{E(\kappa) - (1 - \kappa^2)K(\kappa)} d\kappa^2 \quad (\text{B.1})$$

where κ is a normalized pitch-angle variable defined in [41]. $E(\kappa)$ and $K(\kappa)$ are the complete elliptic integrals of first and second kind and can be calculated as:

$$K(\kappa) = \int_0^{\pi/2} \frac{d\theta}{\sqrt{1 - \kappa^2 \sin^2 \theta}} \quad (\text{B.2})$$

$$E(\kappa) = \int_0^{\pi/2} d\theta \sqrt{1 - \kappa^2 \sin^2 \theta} \quad (\text{B.3})$$

$F_{mnc}(\kappa)$ and $F_{mns}(\kappa)$ are defined as:

$$F_{mnc}(\kappa) = 2 \int_0^{2 \arcsin(\kappa)} \sqrt{\kappa^2 - \sin^2(\theta/2)} \cos((m - nq)\theta) d\theta \quad (\text{B.4})$$

$$F_{mns}(\kappa) = 2 \int_0^{2 \arcsin(\kappa)} \sqrt{\kappa^2 - \sin^2(\theta/2)} \sin((m - nq)\theta) d\theta \quad (\text{B.5})$$

$W_{m,n}$ was calculated numerically for different n and m values. Equations B.4 and B.5 show the dependence of $W_{m,n}$ on the q -profile. The results of the calculation for $W_{m,n}$ are shown in Figure B.1. It can be seen, that $W_{m,n}$ has a maximum at $q = \frac{m}{n}$ and that the half-width of $W_{m,n}$ depends on n .

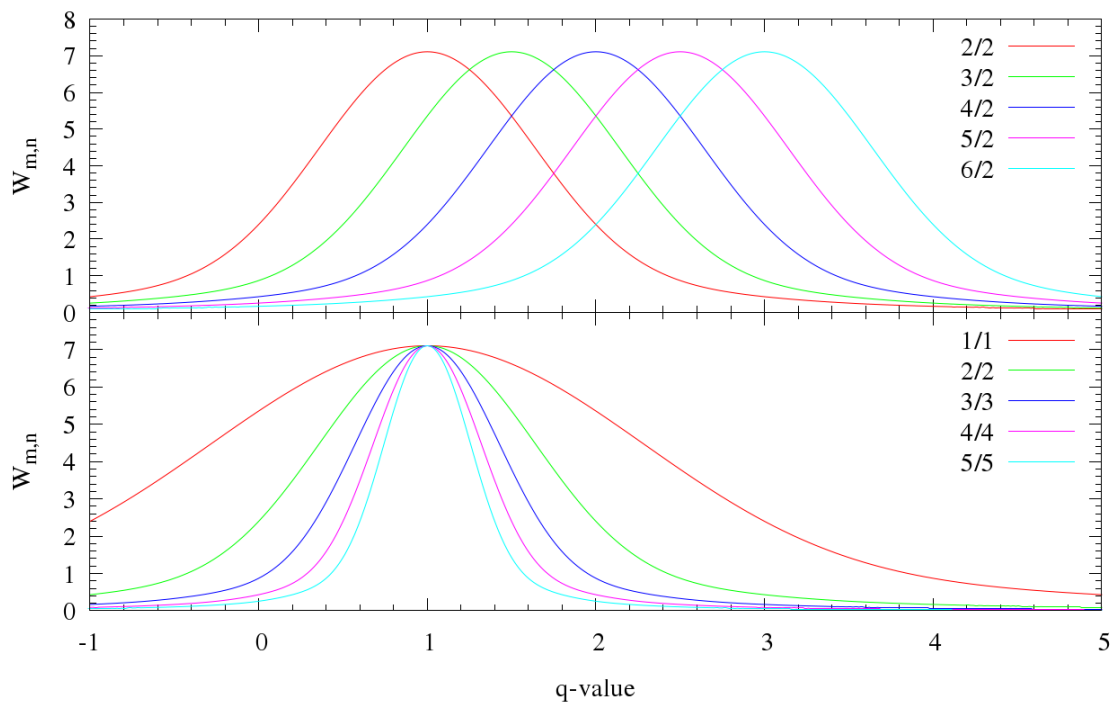


Figure B.1: The influence of $W_{m,n}$ for different q -values. The top graph shows the $W_{m,n}$ for $n = 2$ and varies the m values. The bottom graph illustrates an equal m/n ratio for various n values.

Bibliography

- [1] ASDEX Upgrade documentation, <https://www.aug.ipp.mpg.de/wwwaug/>, 2010.
- [2] H. Biglari et al., “Influence of sheared poloidal rotation on edge turbulence”, *Physics of Fluids B*, vol. 2, pp. 1–4, 1990.
- [3] D. Biskamp, *Nonlinear Magnetohydrodynamics*, Cambridge University Press, 1992.
- [4] B. D. Bondarenko, “Role of O. A. Lavrent’ev in the formulation of the problem and the initiation of research into controlled nuclear fusion in the USSR”, *Physics Uspekhi*, vol. 44, pp. 886–894, 2001.
- [5] I. Classen, “Imaging and Control of Magnetic Islands in a Tokamak”, Ph.D. dissertation, Technische Universiteit Eindhoven, 2007.
- [6] A. J. Cole et al., “Effect of neoclassical toroidal viscosity on error-field penetration thresholds in tokamak plasmas”, *Physical Review Letters*, vol. 99, no. 6, p. 065001, Aug 2007.
- [7] A. J. Cole et al., “Neoclassical toroidal viscosity and error-field penetration in tokamaks”, *Physics of Plasmas*, vol. 15, no. 5, p. 056102, 2008.
- [8] G. D. Conway et al., “Suppression of Plasma Turbulence During Optimized Shear Configurations in JET”, *Physical Review Letters*, vol. 84, no. 5, pp. 1463–1466, 2000.
- [9] M. De Bock, “Understanding and controlling plasma rotation in tokamaks”, Ph.D. dissertation, Technische Universiteit Eindhoven, 2007.
- [10] R. Dux, “Plasmaphysik und Fusionsforschung: Teil II”, Lecture notes, Universität Augsburg, 2002

-
- [11] A. Dinklage et al., “Integrated Data Analysis for Fusion: A Bayesian Tutorial for Fusion Diagnosticians”, *AIP*, vol. 988, no. 1, pp. 471–480., 2008
 - [12] R. Fischer et al., “Multiple diagnostic data analysis of density and temperature profiles in ASDEX Upgrade”, *36th EPS Conference on Plasma Physics*, 2009.
 - [13] B. Geiger, “Optimization of ion temperature and rotation measurements by CXRS”, Diploma thesis, LMU München, 2009.
 - [14] P. Goldston, R. J. Rutherford, *Introduction to plasma physics*, IOP Publishing Ltd, 1995.
 - [15] S. Günter, “Plasmaphysik und Fusionsforschung”, Lecture notes, TU München, 2009.
 - [16] R. J. La Haye et al., “Propagation of magnetic islands in the $E_r = 0$ frame of co-injected neutral beam driven discharges in the DIII-D tokamak”, *Physics of Plasmas*, vol. 10, no. 9, pp. 3644–3648, 2003.
 - [17] M. von Hellermann et al. “Analytical approximation of cross-section effects on charge exchange spectra observed in hot fusion plasmas.” *Plasma Physics and Controlled Fusion*, vol. 37, pp. 71–94, 1995.
 - [18] M. D. Hua et al., “Comparison of MHD-induced rotation damping with NTV predictions on MAST”, *Plasma Physics and Controlled Fusion*, vol. 52, no. 3, p. 035009, 2010.
 - [19] J. D. Huba, “NRL Plasma Formulary”, Naval Research Laboratory, Washington, DC 20375, 2007.
 - [20] I. A. Hutchinson, *Principles of Plasma Diagnostics*, Cambridge University Press, 2002.
 - [21] V. Igochine, “Investigation of MHD Instabilities in Conventional and Advanced Tokamak Scenarios on ASDEX Upgrade”, Ph.D. dissertation, Technische Universität München, 2002.
 - [22] V. Igochine et al., “Hotlink based Soft X-ray Diagnostic on ASDEX Upgrade”, Max-Planck-Institut für Plasmaphysik, IPP Report 1/338, 2010.

- [23] M. Kaufmann, *Plasmaphysik und Fusionsforschung*, Teubner Verlag, 2003.
- [24] Y. B. Kim et al., “Neoclassical poloidal and toroidal rotation in tokamaks”, *Physics of Fluids B: Plasma Physics*, vol. 3, no. 8, pp. 2050–2060, 1991.
- [25] K. Lackner et al., “Long-term fusion strategy in europe”, *Journal of Nuclear Materials*, vol. 307-311, Part 1, pp. 10–20, 2002.
- [26] J. D. Lawson, “Some Criteria for a Power Producing Thermonuclear Reactor”, *Proceedings of the Physical Society. Section B*, vol. 70, no. 1, p. 6, 1957.
- [27] P. J. Mc Carthy et al., “The CLISTE interpretive equilibrium code”, Max-Planck-Institut für Plasmaphysik, IPP Report 5/85, 1999.
- [28] R. M. McDermott et al., “Core Toroidal Rotation Changes Observed with ECRH Power in NBI Heated Plasmas on ASDEX Upgrade”, *36th EPS Conference on Plasma Physics*, 2010.
- [29] R. M. McDermott, Private communication, 2010.
- [30] H. W. Meister, “Transportuntersuchungen im Übergangsbereich von Einschlussregimen an ASDEX Upgrade”, Ph.D. dissertation, Max-Planck-Institut für Plasmaphysik, Garching, 2000.
- [31] J. Meskat, “Untersuchung der Struktur und Dynamik magnetischer Inseln im Tokamak ASDEX Upgrade”, Ph.D. dissertation, Universität Stuttgart, 2001.
- [32] J. Ongena, “Heating, Confinement, and Extrapolation to Reactors”, *Fusion Science and Technology*, vol. 45, pp. 453–466, 2004.
- [33] J. Ongena et al., “Energy for Future Centuries. Will Fusion be an Inexhaustible, Safe and Clean Energy Source?”, *EFDA JET RE (00)01*, 2001.
- [34] M. Reich, “A new diagnostic for ASDEX Upgrade edge ion temperatures by lithium-beam charge exchange recombination spectroscopy”, Ph.D. dissertation, LMU München, 2005.
- [35] J. Schirmer et al., “Rotation frequencies of MHD modes in ASDEX Upgrade”, *34th EPS Conference on Plasma Physics*, 2007.

-
- [36] J. Schirmer, “Plasma Turbulence Studies Using Correlation Doppler Reflectometry on the ASDEX Upgrade Tokamak”, Ph.D. dissertation, LMU München, 2005.
- [37] M. Schittenhelm, “Untersuchung von Tearing Moden in asymmetrisch elongierten Plasmen am Tokamakexperiment ASDEX Upgrade”, Ph.D. dissertation, TU München, 1995.
- [38] W. Schneider et al., “ASDEX Upgrade MHD equilibria reconstruction on distributed workstations”, *Fusion Engineering and Design*, vol. 48, no. 1-2, pp. 127 – 134, 2000.
- [39] M. van Schoor et al., “An experimental and theoretical study on the formation of electric study on the formation of electric field induced flow shear in the tokamak edge”, *Journal of Nuclear Materials*, vol. 313-316, pp. 351–359, 2003.
- [40] B. Scott, “ $\mathbf{E} \times \mathbf{B}$ Shear Flows and Electromagnetic Gyrofluid Turbulence”, *Physics of Plasmas*, vol. 7, no. 5, pp. 1845–1856, 2000.
- [41] K. C. Shaing et al., “Magnetohydrodynamic-activity-induced toroidal momentum dissipation in collisionless regimes in tokamaks”, *Physics of Plasmas*, vol. 10, no. 5, pp. 1443–1448, 2003.
- [42] K. C. Shaing et al., “Plasma flow and confinement in the vicinity of a rotating island in tokamaks”, *Physics of Plasmas*, vol. 10, no. 12, pp. 4728–4736, 2003.
- [43] M. Sokoll, “MHD-Instabilitäten in magnetisch eingeschlossenen Plasmen und ihre tomographische Rekonstruktion im Röntgenlicht”, Ph.D. dissertation, TU München, 1997.
- [44] W. Suttrop, “Astrophysikalische Plasmen”, Lecture notes.
- [45] W. Suttrop, “Electron Cyclotron Emission (ECE) diagnostics,” Internal IPP documentation, 1997.
- [46] P. de Vries, “Magnetic islands in tokamak plasmas”, Ph.D. dissertation, Universiteit Utrecht, 1997.
- [47] J. Wesson, *Tokamaks*, Oxford university press, 2004.

-
- [48] W. Zhu et al., “Observation of Plasma Toroidal-Momentum Dissipation by Neoclassical Toroidal Viscosity”, *Physical Review Letters*, vol. 96, no. 22, p. 225002, 2006.
- [49] H. Zohm, “Trying to establish common understanding about rotation and $\mathbf{E} \times \mathbf{B}$ shear stabilisation”, Internal discussion protocol, 2001.
- [50] H. Zohm, “MHD-Gleichgewichte und Stabilität heißer Fusionsplasmen”, LMU München, Lecture notes, 2004.
- [51] H. Zohm et al., “Overview of ASDEX Upgrade results”, *Nuclear Fusion*, vol. 49, no. 10, p. 104009, 2009.

Acknowledgment

At the end I would like to thank all people helping me to write this thesis. Without the great help of all these people, this work would never be accomplished. Special thanks to:

Prof. Dr. Sibylle Günter, who provided me with the possibility to do this work, for the great support and for her helpful advices. She was a great supervisor and it was a pleasure to work with her.

Dr. Anja Gude for being a great mentor! I would like to thank for her great help, her patience, the fruitful discussions, her ideas and advices, her friendliness and for the help with my thesis. I cannot imagine a better mentor. Thank you Anja, for everything!

Prof. Dr. Hartmut Zohm for his great support and the advice during the whole time of my thesis and for the possibility to be a part of the E1 group.

Dr. Jörg Hobirk, Dr. Marc Maraschek and Dr. Valentin Igochine for their advice, the enjoyable discussions, their support and for their great help during this thesis.

Bernhard Sieglin for various fruitful discussions, for the great time, the great atmosphere and for many enjoyable conversations during the last months.

Dr. Racheal M. McDermott for her help with the CXRS and for her advices.

Matthias Willensdorfer for the enjoyable time and the nice conversations during the last months.

The whole **ASDEX Upgrade Team** for all the help, the great atmosphere and the friendliness I got during this period.

My **parents** and my **brother**, who helped me the whole time during my studies and for their great support during my life.

My lovely wife **Natalia Bytschkow** for her endless patience and her lovely help, when it got late again. Thank you, for the great time with you.

Thank you all!

Erklärung

des Studierenden im Masterstudiengang Engineering Physics

Name: **Bytschkow**

Vorname: **Denis**

Mit der Abgabe der Master Thesis versichere ich, dass ich die Arbeit selbständig verfasst und keine anderen als die angegebenen Quellen und Hilfsmittel benutzt habe.

.....

(Ort, Datum)

.....

(Unterschrift)